UNIVERSITÀ DI PARMA

UNIVERSITA' DEGLI STUDI DI PARMA

DOTTORATO DI RICERCA IN

Scienza e tecnologia dei materiali

CICLO XXXVI

Study of room-temperature multiferroic mixed stuffed tridymite-like barium ferrites in thin film and bulk forms

Coordinatore:

Chiar.mo Prof. Enrico Dalcanale

Tutore:

Chiar.mo Prof. Francesco Mezzadri

Dottorando: Michele Casappa

Anni Accademici 2020/2021 – 2022/2023

Index

1 Introduction

In recent decades, the modern need to model electronic devices capable of expanding computing powers, at the cost of lower energy consumption and reduced environmental impact, is pushing the scientific community to research new multifunctional materials and to optimize methods of integrating them into existing technologies. For this reason, material science holds great interest for multiferroics. The possibility of exhibiting a long-range ordering able to host net polarization and magnetization within the same crystal lattice and of changing its properties through chemical modification plays a crucial role in various fields of modern engineering and physics, from spintronics to sensors, from data storage to photovoltaics. However, despite their immense potential, multiferroics face inherent challenges and limitations that hinder their widespread distribution. A key challenge lies in achieving strong and robust coupling between the ferroic orders, as in many multiferroics the coupling is weak, making it difficult to control and manipulate the two orders simultaneously, and limiting its practical applications. Another challenge is represented by the low transition temperatures in most of the multiferroic structures. These materials often exhibit their ferroic orders at cryogenic temperatures, making them unsuitable for ambient-temperature applications. So, to fully realize the potential of multiferroics, it is essential to develop materials with strong coupling between the ferroic orders and room-temperature ferroic ordering. Moreover, the fabrication of high-quality multiferroic thin films with uniform and well-controlled properties remains a significant challenge. The need for precise control over the crystal structure, composition, and microstructure of these materials is essential for achieving their optimal properties. So, overcoming the inherent challenges and limitations of multiferroics is essential for exploiting their full potential and translating them into practical applications that can revolutionize various fields of technology.

This PhD thesis focuses on the study of some materials belonging to the class of "stuffed" tridymite structures, with parental formula AB_2O_4. The project started with the analysis carried out on barium monoferrite, $BaFe_2O_4$, which is a previously unrecognized multiferroic material at room temperature. Then, the central part of the thesis is devoted to the first successful transfer of pure $BaFe_2O_4$ to thin film form, by exploiting the pulsed electron deposition (PED) technique. This investigation allowed to explore the synthesis

conditions finally allowing to grow single phase $BaFe_2O_4$ over different key materials both in textured and epitaxial thin film form. In addition, the possibility of obtaining structural variants through chemical substitutions, aimed at modulating the physical properties, was evaluated in the bulk form.

2 State of the Art

2.1 Multiferroicity and magnetoelectric coupling

2.1.1 Theoretical and historical background

The first formal definition of multiferroics was drawn up by H.Schmid in 1994 [1], as materials "...in which two or all three of the properties‘ ferroelectricity ’,‘ ferromagnetism ’and‘ ferroelasticity ’occur simultaneously in the same phase...". It was then expanded, including ferrotoroidicity as well as non-primary ferroic orders, such as antiferromagnetic and ferrimagnetic, and entire classes of composite systems (particulates, laminates, rods/fibers). The coexistence of multiple ferroic ordering states can be accompanied by a certain degree of magnetoelectric coupling, so that the ferroelectric and ferromagnetic properties can be controlled by applying external magnetic and electric fields. In particular, this possibility of controlling the orientation of the ferroelectric/ferromagnetic domains has represented a turning point in established fields such as spintronics in the information technology industry: contrary to the traditional approach, whereby the control of the electronic spins takes place by means of a magnetic field, thus entailing high energy consumption and limited data storage, the use of a magnetoelectric device ensures to encode information through an electric field, meeting the demand for low-power bits writing and reading. This has been revealed to be attractive especially for the manufacture of last generation multi-state data memory devices, capable of exploiting the reversible and non-volatile magnetoelectric effect of multiferroic structures [2,3]. Finally, besides microelectronics, the use of multiferroic-based architectures found success in the most disparate fields of research. Multiferroic and magnetoelectric composites have the potential to be used for biomedical applications, such as magnetically assisted in vivo targeted drug delivery: by applying a magnetic field it is possible to guide the nanoparticles to the desired location in the body. Once at the targeted site, an oscillating magnetic field can be applied to induce a change in their electric polarization and shape, breaking the drug-nanoparticle bond and releasing the drug molecules at the specific location. Multiferroics have also emerged as promising materials for harvesting energy from sunlight through the exploitation of ferroelectric and ferromagnetic domains. The internal electric fields associated with ferroelectricity facilitate the separation of electrons

and holes, while, if present, the transition-metal *d* states reduce the band gap, enabling the absorption of low-energy solar phonons. In addition, the magnetic properties of multiferroics offer the possibility of controlling the photocurrent direction using magnetic fields. All these features could simplify the design of photovoltaic devices [4]. However, despite the promising technological impact of these materials, the occurrence of ferroic orders is hard to obtain as it must respect restrictive symmetry requirements; so that, as an example, to have a structural transition from a paraelectric-disordered state to a ferroelectric-ordered one, a spontaneous spatial symmetry breaking must take place. As stated by Schmid, the crystallographic classification identifies a series of polar point groups, whose peculiar absence of an inversion center among the possible symmetry operations is able to generate an anisotropy in the orientation of the electric dipole moments inside the crystal, thus allowing the presence of a polarization (non-zero and switchable). These features can be found in 10 of the 32 crystallographic point groups: *1, 2, m, mm2, 4, 4mm, 3, 3m, 6, 6mm*. The same applies to magnetic ordering, which requires a structure with breaking of the time-inversion symmetry, that is, able to allow a parallel alignment, ruled by the exchange interaction term [5]. It follows that the simultaneous occurrence of both ferroelectric and ferromagnetic ordering requires that both spatial and time inversion symmetries are broken simultaneously at certain critical temperature values, below which the symmetry transition is energetically favorable. However, the achievement of such conditions has been traditionally hampered by the mutually exclusive electronic demand of the two ferroic orders; in fact, as observed by N.Hill [6], in classical ferroelectric ABO_3 perovskites (barium titanate, as an example, $BaTiO_3$), symmetry breaking is usually induced by a d^0-transition metal in the octahedral B-site, through the formation of an asymmetric coordination, hindering any magnetic ordering due to the lack of unpaired electrons (as in the case of Ti^{4+}). On the other hand, a condition diverging from d^0-ness would promote the establishment of Jahn-Teller-type distortions, energetically competing with the off-centering process necessary for ferroelectric ordering. This dichotomy still represents the main limiting factor of classical ferroelectric systems, so that, in the first decades the research achievements were extremely limited in the first decades. Nonetheless, the so-called first era of multiferroics was featured by some interesting discoveries: in 1966 Ascher et al. investigated the properties of nickel-iodine boracite, $Ni_3B_7O_{13}I$, a multiferroic material that exhibits both ferroelectricity ($T < 64$ K) and weak ferromagnetism ($T < 29$ K) simultaneously. Interestingly, a coupling between

these ferroic orders leads to a colossal linear magnetoelectric effect, thus enabling the hysteretic switching of a multiferroic state by either electric or magnetic fields [7]. Moreover, it should be noted that bismuth ferrite perovskite, $BiFeO_3$, which is one of the most studied modern multiferroics, was first recognized as a multiferroic material in 1960s [8]. Anyway, the discovery of new symmetry- and structure-related phenomena, as new types of long-range magnetic orders [9], combined with the optimization of theoretical tools, which allowed the construction of precise mathematical models (Landau theory above all [10]), encouraged the scientific community to devise new synthesis strategies to solve the impasse described by Hill, and paved the way for a revitalized second era. To date, 4 main mechanisms capable of driving multiferroism are known (Figure 1):

(I) Electronic lone pair mechanism, according to which the ferroelectric order is generated by the stereochemical activity of localized s electrons, that via partial hybridization with the p orbitals of the surrounding anions give rise to asymmetrical coordination. Typical examples are ABO_3 perovskite containing Bi^{3+} or Pb^{2+} in the A-site, that, with the simultaneous presence of magnetically active atoms in the B-site, can produce multiferroicity and then, magnetoelectric coupling.

(II) Geometric mechanism turns out to be the result of structural distortions leading to the so-called "improper" ferroelectricity. This phenomenon, which can also be described by the second order Jahn-Teller effect [11], usually takes place in manganese-based hexagonal perovskites, in which the layers of Mn^{3+} ions have two different types of coordination, giving rise to the instabilities at the origin of noncentrosymmetric distortions.

(III) Charge ordering occurs in materials featured by alternating layers of ions displaying different oxidation states (for example Fe^{2+}/Fe^{3+} in $LuFe_2O_4$ [12]), thus inducing an electric polarization because of the lack of geometrical compensation in this arrangement. Such systems are "dimerized-charge" ordered and the presence of magnetic ions can result in a net magnetization.

(IV) Eventually, improper ferroelectricity can originate by a spin-induced mechanism, which in turn is related to the non-centrosymmetric nature of the magnetic ordering. This effect is ascribed to the strong correlation between the magnetic long-range order of the material and its crystal structure and is governed by the inverse Dzyaloshinskii-Moryia (DM) interaction, depending on the spin-orbit coupling. Otherwise, also the magnetostriction occurring in periodic collinear spin arrangements can induces a net polarization, without the exploitation of the spin-orbit interaction.

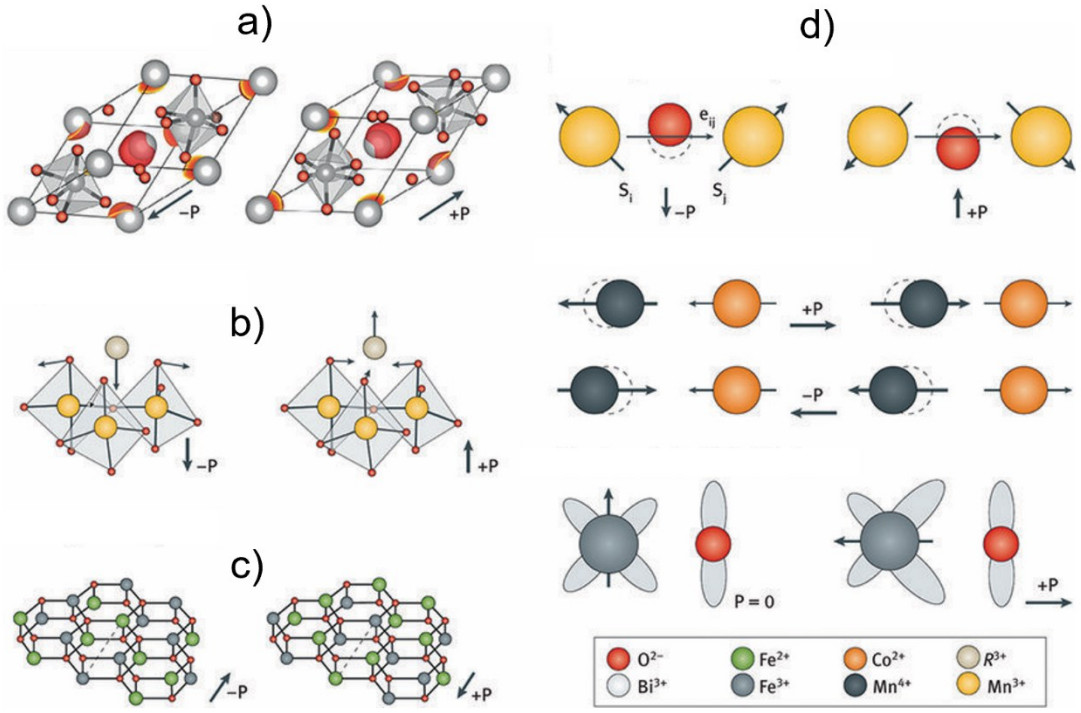

Figure 1 – Multiferroism-driving mechanisms. a) Lone-pair mechanism: the figure shows the example of $BiFeO_3$, in which polarization is induced by the shift of Bi^{3+} ions towards the FeO_6 octahedra. The polar vector is parallel to [111] lattice direction. b) Geometric ferroelectricity: given a general hexagonal-$RMnO_3$ structure, the movements of the MnO_5 bipyramids cause a shift of the R-ions, resulting in a net polarization. c) Charge ordering mechanism: the alternation of Fe^{2+} and Fe^{3+} layers in $LuFe_2O_3$ was proposed to give rise to a spontaneous electric polarization that can be switched by the jump of an electron from the Fe^{2+} to the Fe^{3+} site. d) Magnetically induced ferroelectricity: it is due to the inverse DM interaction, which can induce a canting of neighboring magnetic spins, and, therefore, a polar displacement (top image). Also, ferroelectricity can arise from magnetostriction (middle) and, in some materials, by a spin-driven modulations in chemical bonding (bottom) [13].

2.1.2 Type-I multiferroics

The aforementioned classification defines the mechanisms that occur in two macro-

categories of materials: type-I and type-II multiferroics.

Type-I ones, which represent the most "classic" case of multiferroic state, have two distinct and independent electrical and magnetic sorting mechanisms, at different (and usually rather high) critical temperatures. Among these, the transition metal perovskite oxide family is one of the most studied and developed systems, due to its capacity to undergo several distortions and host a wide array of ions with different size and oxidation state. This inevitably reflects on the variability of the properties: starting from the structure of a simple perovskite, ABO_3, where the BX_6 octahedra generate a framework with the larger 12-coordinated A-cations, it is possible to model different compositions by chemical substitution with transition metals or elements from the lanthanide group, so as to obtain multiple behaviors, from insulator to conductor, from ferromagnetism to magnetic frustration, from simple piezoelectricity to long-range ferroelectricity. This is particularly true for the so-called double perovskites, which, being characterized by an $ABB'X_6$ type formula, with the B- and B'-cations being ordered and not randomly distributed in the lattice, benefit from the tuning of the properties carried by the chosen ions. In particular, the interest reserved for these mixed systems was encouraged by the prospect of setting the appropriate conditions to establish a certain degree of coupling between the magnetic moments of nearby atoms and, consequently, as predicted by the Goodenough-Kanamori semi-empirical rule [14], induce the long-range ferromagnetic order. For sure, one of the most studied cases is that related to Sr_2FeMoO_6, whose multiple properties, including low dielectric losses at high temperature, half-metallicity and low-field RT magnetoresistance, make it ideal for some interesting applications in magnetic sensors and spintronics [15,16]. Also, the combination of Fe^{3+} and Cr^{3+} layers showed potential multiferroic properties. In particular, epitaxial Bi_2FeCrO_6 thin films display both ferroelectricity, driven by the action of the $6s^2$ lone pair of the Bi^{3+} ions, with a maximum dielectric polarization of 2.8 $\mu C/cm^2$ and a magnetic saturation around 20 emu/cm^3 at room temperature, ascribable to a strong superexchange interaction in the Fe-O-Cr bonds, which, in turn, is induced by epitaxially-induced strains; this magnetization experiences a net reduction at a specific critical film thickness ($t > 80$ nm), leading to the unavoidable formation of defects [17, 18]. However, the manufacture of these promising architectures has to deal with some crucial drawbacks, such as the presence of impurities due to the different chemical characteristics of the involved species, and, in the latter case

mentioned, a certain degree of disorder detected at the B-site, as a consequence of the similar size of the Fe^{3+} and Cr^{3+} ions.

I. Bismuth ferrite ($BiFeO_3$)

Among the most well-known simple perovskite oxides, bismuth ferrite, $BiFeO_3$ (BFO), has had the greatest success, especially from an application point of view. This material, belonging to the *R3c* space group, has a spontaneous polarization along the pseudocubic direction <111> of ~100 μC/cm^2, induced by the combination of the partial dislocation of Bi^{3+} ions with the shift of the iron ions within the octahedra formed with oxygen. BFO is also an antiferromagnet with a G-type order, meaning that layers of ferromagnetically coupled iron spins are antiferromagnetically oriented with respect to the adjacent ones. Such structure is able to generate a small canting of the magnetic moments as a result of DM interaction. Both ferroic orders are stable at high temperatures (T_{Curie} = 1100 K; $T_{Néel}$ = 670 K), making of this material a promising candidate to room temperature application.

Noteworthy, the most interesting features were observed on BFO thin films. Zhao et al. [19] found out that the switching of polarization, through an electric field, of (001)-oriented BFO films grown on $SrTiO_3$ (100) substrates also modify the orientation of antiferromagnetic domains, thus giving rise to magnetoelectric coupling. This is due to symmetry relations occurring between the film and substrate, allowing a multiple orientation of the polarization vector, i.e. at 71°, 109° and 180° with respect to the direction of spontaneous polarization (Figure 2).

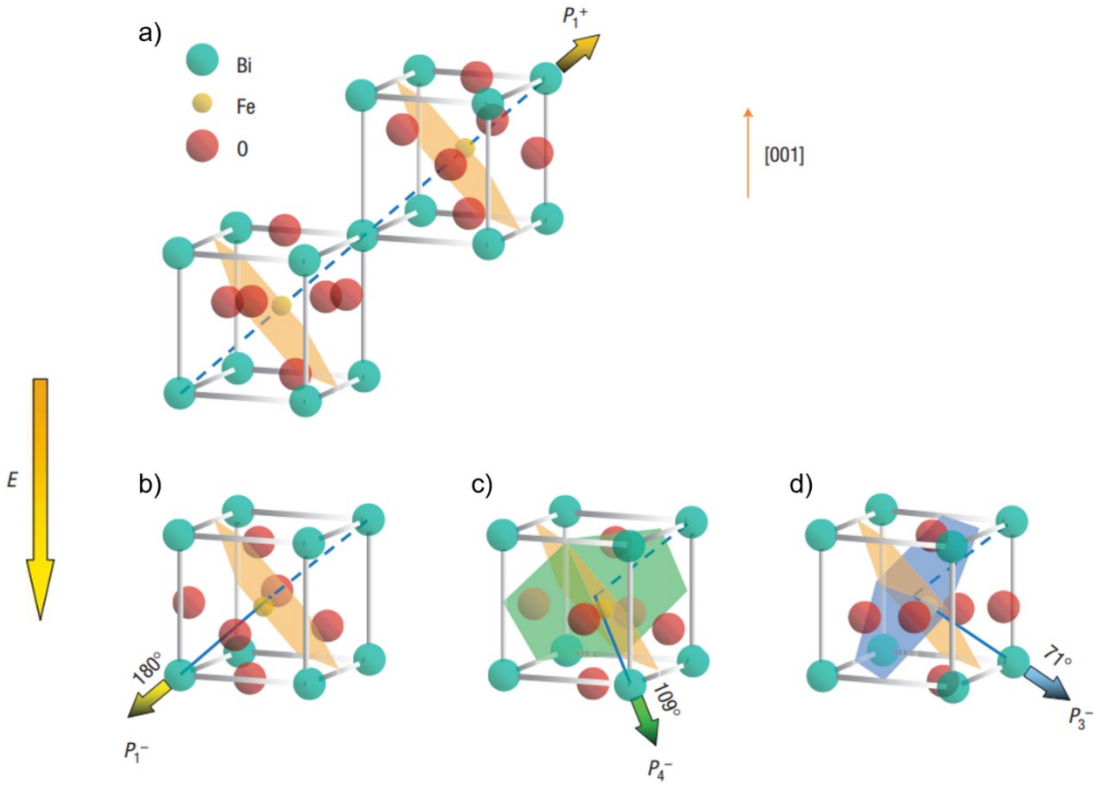

Figure 2 – $BiFeO_3$ crystal structure and its ferroelectricity and antiferromagnetism (pseudocubic index). a) (001)-$BiFeO_3$ with the spontaneous polarization lying along the <111> direction (P_1^+) and the antiferromagnetic plane (orange) orthogonal to the polar vector. b)-c)-d) Change of orientation of the antiferromagnetic plane (green and blue) as a result of the 180°, 109° and 71° polarization switching, respectively, after applying an electric field along the [001] direction [19].

Epitaxy also opens up the possibility of controlling domain structures, which is difficult to achieve in bulk samples. Factors such as the choice of an appropriate monocrystalline substrate, which is responsible for the applied strain on the film and any anisotropy in the charge distribution at the BFO/substrate interface, and the application of an external electric field can strongly influence the selection of different polarization states and induce the formation of individual domain walls [20, 21]. All the domain engineering methods developed for BFO have been progressively encouraged, as having specific domain walls often means acquiring unique properties. As an example, since the optical bandgap of BFO (2.3-2.8 eV) can be narrowed by strain engineering (by applying uniaxial/hydrostatic pressures externally or by latex mismatching), a well above bandgap ferrophotovoltaic effect was observed in BFO thin films, due to the separation of photogenerated charge carriers occurring at the domain walls. In particular, as shown in

Figure 3, the electric transport measurement carried out with top electrodes orthogonally oriented with respect to the 71°-domain walls revealed a large photoinduced open-circuit voltage (16V) while the film is under illumination [22].

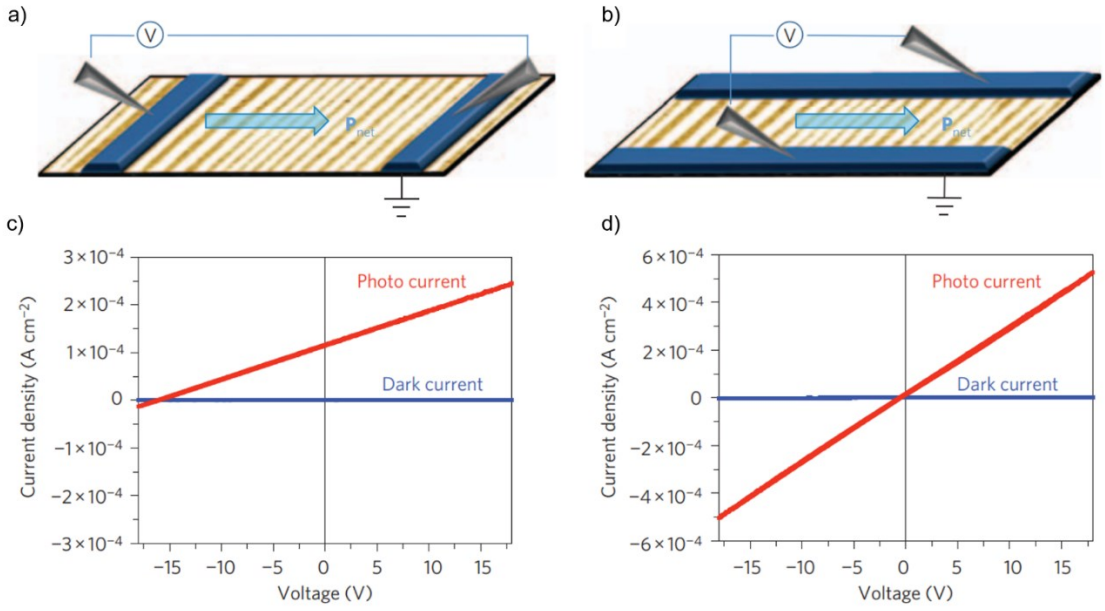

Figure 3 – Light and dark I-V measurements. a)-b) Schematics of device geometries, with electrodes for electric transport measurements perpendicular and parallel to the $BiFeO_3$ domain walls, respectively. c)-d) corresponding measurements carried out on a) and b) architectures [22].

Furthermore, BFO has proven to be easily and effectively integrated in those multilayer heterostructures exploiting interfacial magnetoelectric coupling for low-power electric field-controlled magnetic random-access memories (MRAM) in data storage. Within this framework, Chu et al. [23] suggested to use the strong magnetoelectric coupling possessed by BFO in order to correlate its antiferromagnetism to the ferromagnetic domains of $Co_{0.9}Fe_{0.1}$, thus promoting an increase in the coercive field and a shifting of the ferromagnetic hysteresis cycle. More interestingly, the polarization of BFO layer, being responsible for the switching of antiferromagnetic domains, leads to a reversible rotation of the magnetization of $Co_{0.9}Fe_{0.1}$ one, precisely thanks to the collinear coupling between the magnetic state of the ferromagnet and the orientation of the antiferromagnetic plane (Figure 4). This is evident from the analysis carried out on local magnetization in CoFe using the X-ray magnetic circular dichroism-photoemission electron microscopy, through which it was possible to detect changes in the magnetic direction of $Co_{0.9}Fe_{0.1}$

layer while the electric field is applied (Fig. 4c). This interfacial effect, combined with the electric field-mediated magnetization control, has a great impact on all those technologies that require the stabilization of specific magnetic domain states in soft ferromagnets used in magnetic recording at lower energy consumption. Specifically, this solution represented the turning point for already known devices: as an example, the deposition of spin valves on top of BFO/Mn doped BFO(001) heterostructure turned out to produce a giant magnetoresistance effect and allowed to optimize the exchange bias [24].

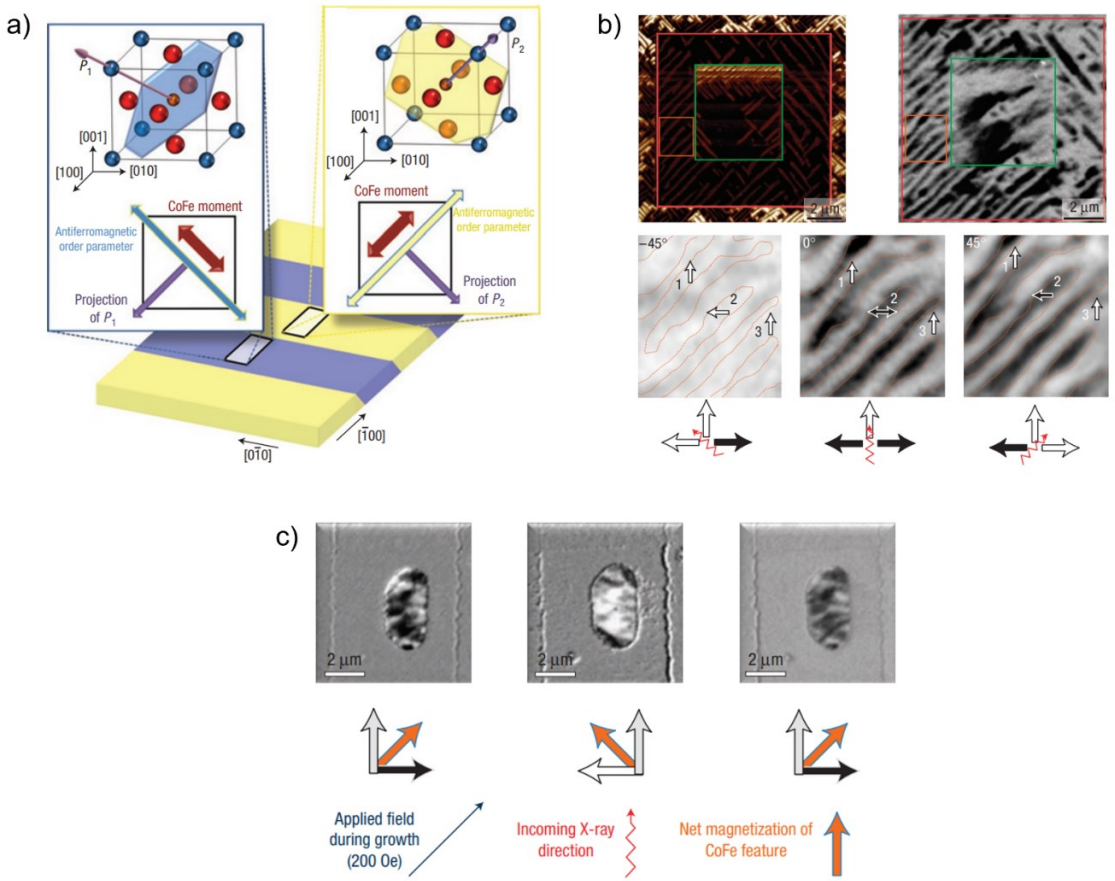

Figure 4 – a) Polarization switching-induced antiferromagnetic plane rotation in $BiFeO_3$ and resulting effect on CoFe magnetic moments. b) Top images: on the left side, in-plane piezoresponse force microscopy images collected in a 10 µm region (red square) and in smaller 5 µm region by applying different electric fields (±12 V). On the right side, corresponding images taken from X-ray magnetic circular dichroism–photoemission electron microscopy (XMCD-PEEM) at the Co L-edge for the CoFe layer grown the previously written pattern, showing a comparable arrangement of the magnetic states with that of the electrically poled regions below. Bottom images: XMCD-PEEM measurements show the different rotation states of the Co Fe domains by varying the incoming X-ray. c) XMCD-PEEM images collected to reveal the magnetic domains of CoFe layer in the as-grown state (left) and after first and second electrical switch (central and right). The magnetic contrast (grey, black and white) proves the ability of electric field to rotate the magnetization by 90° [24].

By taking into account other properties discovered in this material, such as the presence of a certain degree of conductivity within the domain walls found at low temperatures (~50K), which promises the creation of functionalized nanoscopic channels [25], or the decrease of polarization and its coercive field through chemical substitution with La^{3+} ions [26], useful in low consumption spintronics, it can be easily concluded that BFO to date stands as a leading material in the field of magnetoelectric multiferroics.

2.1.3 Type-II multiferroics

The class of type-II multiferroics refers to those materials exhibiting an improper ferroelectricity, induced by a different ordering phenomenon. This means that a crystal structure being centrosymmetric, so that it could not host a ferroelectric order, will undergo an inversion symmetry breaking driven not by its first order parameter (i.e. polarization) but as a second order event. In most of the cases ferroelectricity is induced by magnetic ordering, through mainly two different mechanisms: symmetric exchange and antisymmetric spin exchange interaction. The former, which is typical of collinear structures, can induce a magnetostriction, resulting in an ion shifting in the magnetic phase and, therefore, in the formation of polarization. This mechanism characterizes in particular the series of compounds of the RMn_2O_5 family, including the very first type-II magnetoelectric to be discovered: $TbMn_2O_5$. In this material the polarization switching via an applied magnetic field was demonstrated; however, as often observed in type-II magnetoelectrics, the ferroelectric transition temperature is rather low (40 K), making the material hard to find a field of application [27].

The second one, also called inverse DM interaction (see paragraph 2.1.1), describes all those materials that have spiral or helical magnetic structures. The DM effect, whose origin is ascribed to the spin-orbit coupling, can be defined for two neighboring i- and j-atoms, with a spin $\mathbf{S} \neq 0$, as $\mathbf{D_{ij}} \cdot (\mathbf{S_i} \times \mathbf{S_j})$, where $\mathbf{D_{ij}}$ is a symmetry-dependent vector, affected by the oxygen ion displacement from the 180° i-j bond; as a consequence, this interaction leads to the canting of the spins S_i and S_j. On the contrary, therefore, the presence of a magnetic structure made of neighboring canted spins, as the case with a cycloidal arrangement, favors the displacement of oxygen atoms, thus generating a polarization proportional to the vector product $\mathbf{r_{ij}} \times (\mathbf{S_i} \times \mathbf{S_j})$ with r_{ij} as the distance between the two sites i and j. This effect is reported for $TbMnO_3$, a manganite with a distorted perovskite structure, hosting an antiferromagnetic sinusoidal ordering below $T_{Néel} = 40$ K; by further lowering the temperature ($T < 28$ K) the spin lattice assumes a cycloid-type spiral ordering. It has been shown that the ferroelectric polarization emerges precisely at this transition, until it reaches values around 600-800 $\mu C/m^2$, optimizable up to about 2000 $\mu C/m^2$ by a partial substitution on the site with smaller cations, such as Dy^{3+} [28, 29]. To date, among the most promising induced-multiferroics there is certainly copper(II) oxide, CuO, already known as a starting material for high critical temperature

superconductors, showing strong exchange interaction and, therefore, higher ordering temperatures (in this case, between 213 and 230 K) [30]. Also, Hexaferrite-based architectures, such as Y-type $Ba_2Mg_2Fe_{12}O_{22}$, have shown important advantages in terms of application, including a very sensitive magnetoelectric response for low intensity magnetic fields (~ 0.03 T) and a relatively high Curie temperature (at $T_c < 195$ K a screw-type spin structure is established) [31]. In any case, also from these more recent studies it is evident the need for further investigation on this class of multiferroics, able to obtain materials with consistent electromagnetic properties and operating temperature values comparable to key materials as in the case of the most classic type-I multiferroics.

2.2 Stuffed tridymite-like compounds

The previous paragraphs clearly outline a series of decisive challenges to make magnetoelectric mutiferroics real options for state-of-the-art devices development. Despite the presence of extremely high-performance leading materials such as $BiFeO_3$ (see paragraph 2.1.2), the discovery of new structural archetypes with robust magnetoelectric coupling properties at room temperature and at reduced switching energies is strongly motivated by the technological needs of next generation logic devices, looking for higher computing powers and reduced energy consumption.

This section introduces a specific category of compounds, structurally based on a known polymorphic phase of silica, namely tridymite, which allowed explore multiferroism outside the commonly studied class of perovskite derived materials.

2.2.1 SiO_2-Tridymite: structure and phase transitions

Silica (SiO_2) can crystallize into 8 different polymorphs: α-quartz (low quartz), β-quartz (high quartz), tridymite, cristobalite, coesite, stishovite, moganite and keatite (Figure 5) [32]. Excluding stishovite, the polymorph stable at the higher pressures (P>8 GPa at RT), characterized by the unusual octahedral coordination for the Si^{4+} ion, the description of all the other phases involves a common structural unit, consisting of vertex-sharing SiO_4 tetrahedra.

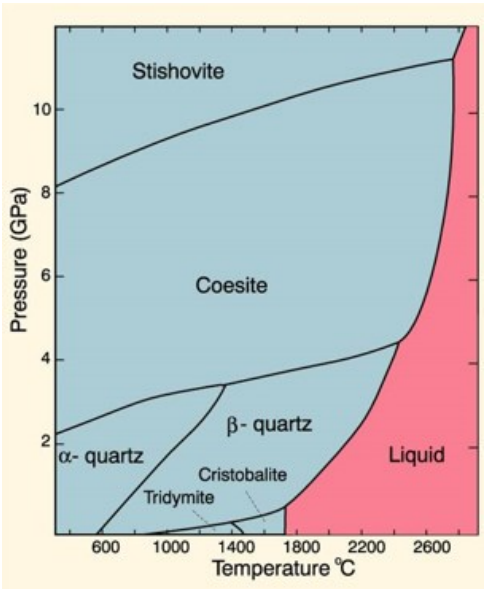

Figure 5 – Phase diagram of silica, SiO_2 [33]. Not all silica polymorphs are shown.

The different arrangements of the tetrahedra are at the origin of the different physical and symmetry properties. In particular, at high temperatures and low pressures, the crystalline structures called tridymite and cristobalite are the most favored and, overall, are the result of "reconstructive" transformations, leading to the formation of planes consisting of six-term rings, made of six adjacent SiO_4 blocks. This arrangement means that tridymite and cristobalite have lower densities than quartz (2.33 g/cm^3, 2.37 g/cm^3 and 2.65 g/cm^3, respectively). As the pressure increases, in fact, the denser phases are stabilized. Tridymite is noteworthy for its ability to generate up to seven different phases (Figure 6), which are the result of a series of displacive transitions that occur at different heating temperatures and kinetic cooling rates down to room temperature [34].

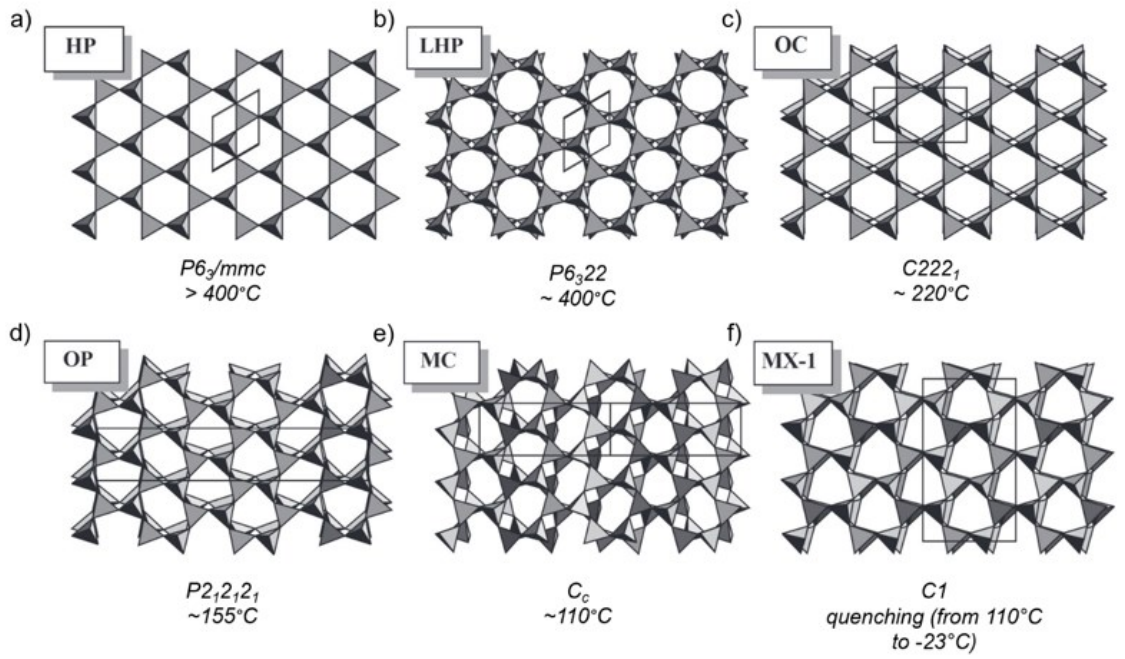

Figure 6 – Tridymite polymorphism. a) Hexagonal primitive tridymite; b) low hexagonal primitive tridymite; c) orthorhombic C-centred tridymite; d) orthorhombic primitive tridymite; e) monoclinic C-centred tridymite (projection along the [101] direction); f) monoclinic tridymite. a)-b)-c)-d)-f) structures are projected along the [001] direction [34].

These polymorphs are variants of the idealized hexagonal structure of the tridymite, the so-called *Hexagonal Primitive* (HP) tridymite; therefore, they can be described by stacking planes consisting of hexagonal rings formed by tetrahedra of SiO_4, connected by vertices, and pointing alternately upwards and downwards (Figure 7a). The stacking sequence of the layers is of the hexagonal-closed packed type, "ABAB", different from that observed in cristobalite, where the sequence is of the "ABCABC" type. This means that, in HP-tridymite, the oxygens at the base of the tetrahedron lie one above the other assuming a cis orientation; while, in β-cristobalite, the tetrahedra assume a trans orientation (Figure 7b). From a symmetry point of view, this structure belongs to $P6_3/mmc$ space group, with *6* axes passing through the center of each hexagonal ring. The above-described arrangement not only suggests that the cavities that are formed between the planes are the basis of the structure's good ability to bear high degrees of distortion, as precisely evidenced by the wide range of obtainable polymorphs, but also that tridymite is a good ground on which some chemical modifications capable of generating new derived structures could be attempted.

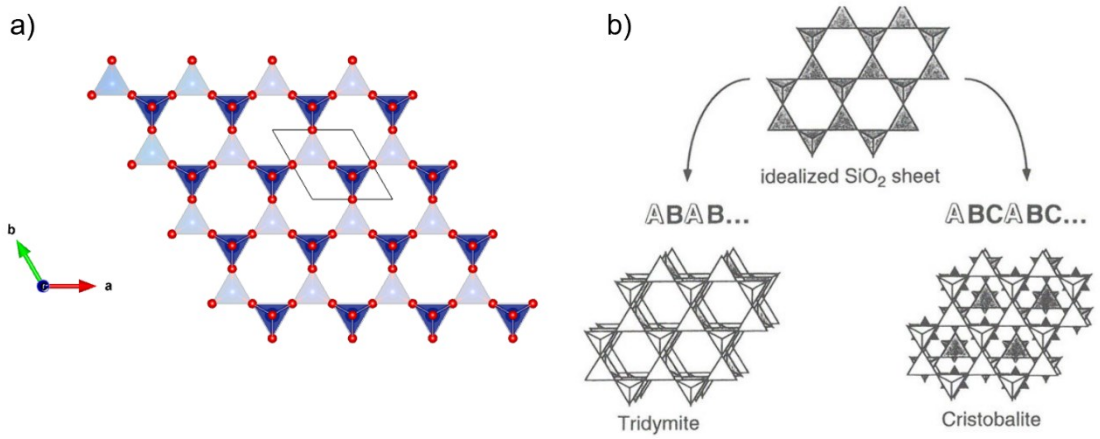

Figure 7 – a) SiO_4 tetrahedra distribution in the reference structure of HP-tridymite [35]. b) Two ways of stacking the identical layers formed by the SiO_4 tetrahedra: the sequence "ABAB" leads to the idealised structure of the tridymite, that "ABCABC" to the idealised structure of the cubic cristobalite. For clarity, the successive layers are slightly staggered [36].

2.2.2 Stuffed-tridymite compounds

Among the various polymorphic structures of silica, the tridymite one is particularly suitable for the insertion of even rather large cations. The presence of structural "channels" parallel to the direction [001] makes HP-Tridymite polymorph suitable for accommodating chemical modifications, thus generating the so-called "stuffed" derivatives of tridymite, with general formula AB_2O_4. The small B-site cation is located in the tetrahedral coordination polyhedra made of oxygen anions; the resulting BO_4 units form the typical tridymite six-term rings, whose voids are filled by A-site ions, also called stuffing cations. The partial or total substitution of tridymite silicon with lower valent ions and the subsequent introduction of cations into the large cavities allow to achieve charge neutrality. In these compounds, the stuffing cations are generally alkali and alkaline earth metals, and their inclusion in the structure depends on the compatibility with shape and size of the reticular cavities. In some cases, the framework may be distorted, so as to increase or decrease the size of the cavities in accordance with the ion radius of the hosted cation, leading to a wide variety of different derivative structures. Figure 8 shows the two possible distortion mechanisms that reduce the size of the channels parallel to the [001] direction. The three types of rings can all be observed in the so-called "stuffed" derivatives of tridymite [36]. Table I shows a series of basic tridymite derivatives.

Figure 8 – Two possible distortions of the hexagonal ring as a result of the rotation of the SiO_4 tetrahedra [36].

Table I – Some compounds showing the stuffed tridymite structure.

Derived structure	Cell parameters						Space group
	a (Å)	b (Å)	c (Å)	α	β	γ	
$BaAl_2O_4$[45]	10.470		8.819	90°	90°	120°	$P6_3$
$SrAl_2O_4$[46]	8.926		8.4985	90°	90°	120°	$P6_3$
$PbAl_2O_4$[47]	8.458	9.234	5.07	90°	90°	90°	*Ama2*
$SrFe_2O_4$[48]	8.1098	9.118	10.8495	90°	90°	91.53°	$P2_1/n$
$PbGa_2O_4$[47]	8.575	9.424	5.22	90°	90°	90°	*Ama2*
$BaGa_2O_4$[49]	18.6403		8.6801	90°	90°	120°	$P6_3$
γ-$SrGa_2O_4$	8.110	10.761	9.057	90°	91.569°	90°	$P2_1/n$
$KLiSO_4$	5.1421		8.634	90°	90°	120°	$P6_3$
$KAlSiO_4$ (kalsilite)	5.1982		8.5865	90°	90°	120°	$P6_3$
$KAlSiO_4$ (ortorombico)	15.669	9.057	8.621	90°	90.16°	90°	$P2_1$
$KNa_3Al_4Si_4O_{16}$ (nefelina)	10.01		8.405	90°	90°	120°	$P6_3$

Among these, the compounds of the $NaAlSiO_4$-$KAlSiO_4$ series are of some geological relevance; the most important are nepheline, $Na_3KAl_4Si_4O_{16}$, and kalsilite, $KAlSiO_4$ [36]. The distribution of atoms in the structure of nepheline which derives, like kalsilite, from the distortion of the tridymite cavities, is such that the alkali ions are clearly separated into two categories and the resulting formula is $A'A_3''Al_4Si_4O_{16}$. The collapse of the tridymite structure generates a larger cavity (site A') in which the larger radius ion is located, while the one inside the smaller site A'' has smaller dimensions. The structure of kalsilite derives from the ditrigonal distortion of the rings formed by six tetrahedra in the structure of the idealized tridymite. As can be seen from Table I, among the main compounds derived from the tridymite structure are those of the above-described AB_2O_4 type, mostly known in the field of photoluminescence. $BaAl_2O_4$, has been proposed as a new generation luminescent material, both in undoped form and doped with europium (II), in which the ferro-to-paraelectric transition through exposure to an electron beam at low temperature plays a role on the modification of the emission bands of the compound [37]. This compound has also been under investigation for its potential ferroelectric

nature, due to its non-centrosymmetric lattice structure (space group *P6₃*). However, despite its interesting capacitor behaviour within a broad temperature range, the performed room-temperature electric characterization has resulted in a weak ferroelectric component with a low saturated polarization value (~0.052 μC/cm^2) [38]. Even $SrGa_2O_4$ stuffed tridymite [39] has been suggested for luminescence applications: Liu et al. investigated the crystal-field splitting of europium ions in doped *γ*- and *β*-$SrGa_2O_4$, demonstrating that the former polymorph has a stronger interaction between the Eu^{3+} ions and the surrounding oxygen ions thanks to its hexagonal structure. The larger crystal-field splitting in *γ*-SrGa2O4 results in a narrower excitation band and a broader emission band, thus suggesting that *γ*-SrGa2O4 may be more suitable for luminescent applications, such as durable phosphor, optical memories and electroluminescent displays, than orthorhombic *β*-$SrGa_2O_4$ [40, 41]. Stuffed tridymite frameworks have also proven to bear different types of chemical modifications. Tanaka et al. [42] provide a detailed study of the structural and microstructural changes that occur in stuffed tridymite-type compounds $Ba_{1-x}Sr_xAl_2O_4$, revealing that its crystal structure changes from a hexagonal *P6₃22* space group to a monoclinic *P2₁/n* space group as x increases. Sr^{2+} content also affects the concentration of defects, such oxygen and strontium vacancies and Sr^{2+} interstitials. Double ions sites substitutions are also possible, as shown by germane ferrite $K_{0.75}Ba_{0.25}Fe_{1.25}Ge_{0.75}O_4$, a hexagonal mixed stuffed tridymite featured by off-centering of the bridging oxygen atoms along c-axis, which is likely due to the absence of ordered A- and B-sites [43]. The induction of these structural distortions might be a viable route to get a wide range of electric and magnetic properties. More recently, partial chemical substitution at the B-site via solid-state synthesis has proven to be a proper strategy to obtain a variety of chemical-physical properties. The so-called mixed stuffed-tridymites, with formula $Ba(Zn/Co)_{1-x}Si_{1-x}M_{2x}O_4$ (M=Al^{3+}, Fe^{3+}), exhibit multiferroic behavior, characterized mostly by weak ferroelectricity and antiferromagnetism at room temperature; on the other hand, the co-substitution of Co^{2+} and Fe^{3+} in $BaCo_{0.75}Si_{0.75}Fe_{0.5}O_4$ guaranteed a ferromagnetic component to the structure, though far below room-temperatures (~ 2 K), as well as interesting optical properties attributable to the metal-to-metal charge transfer between the substituent ions. If we also consider the low dielectric losses, together with the variability of the band-gap values observed, these solid solutions potentially promise to be an interesting choice in various fields, such as photocatalysis and photovoltaics [44].

2.2.3 Barium monoferrite $BaFe_2O_4$

The present PhD project is mainly focused on the $BaFe_2O_4$ (BaFeO) compound, a stuffed tridymite material, in which silicon ions are replaced by Fe^{3+} ones in the tetrahedral B-site, and Ba^{2+} stuffing cations ensure the charge neutrality of the structure.

The first series of studies conducted between the 1960s and 1970s on barium ferrite focused on the definition of its polymorphism, summarized in the table and figure below (Table II and Figure 9) [50, 51].

*Table II - Lattice parameters of the α-, β-, β'- and γ-BaFeO phases. *Possible pseudo-hexagonal. The parameters in the hexagonal reference axes are given in the first line, the orthorhombic ones in the second.*

Phase	Stable at	Symmetry	Spatial Group
α-$BaFe_2O_4$	> 1000 °C	Hexagonal	$P6_322$
β-$BaFe_2O_4$	800 °C < T < 1000°C	Hexagonal *	
		Orthorhombic	
β'-$BaFe_2O_4$	RT	Orthorhombic	$Pmc2_1$
γ-$BaFe_2O_4$	RT	Orthorhombic	$Cmc2_1$

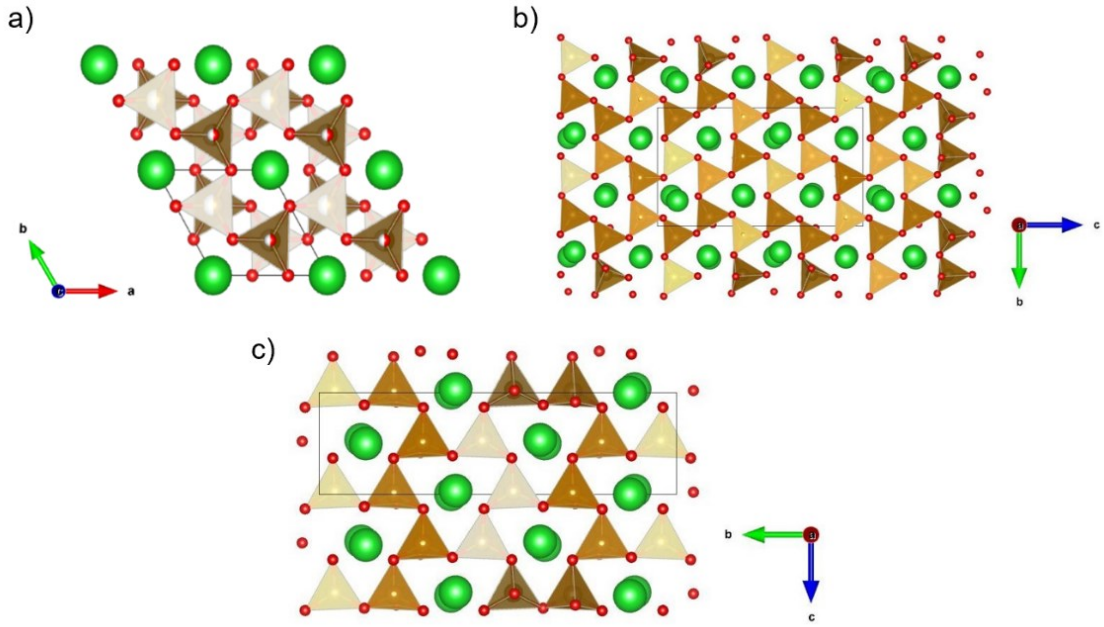

Figure 9 – a) α-$BaFe_2O_4$ structure projected along the [001] direction [51]; b) β'-$BaFe_2O_4$ structure projected along the [100] direction; c) γ-$BaFe_2O_4$ structure projected along the [100] direction (obtained from our X-ray single-crystal diffraction refinement). Green, brown and red atoms are barium, iron and oxygen ions, respectively.

The BaO-Fe_2O_3 system undergoes polymorphic transitions at about 800°C (β-BaFeO) and 1000°C (α-BaFeO). By quenching the samples from high temperature, it was found that there two phases can be observed at room temperature, called γ and β'. The γ phase

is obtained by quenching at temperatures below 800° C or above 1000° C, thus proving to be structurally related to the α polymorph; while the β'phase, which is metastable, is obtained by quenching at temperatures between 800 and 1000° C, i.e. in the region of existence of the β phase. The β'polymorph, by virtue of its metastable nature, converts to γ after a short treatment at about 400° C, highlighting that the γ phase is the stable one at room temperature. Among these four polymorphs, the most interesting one is undoubtedly the γ-phase, as it is the only non-centrosymmetric ($Cmc2_1$ space group) and, therefore, potentially ferroelectric. Conversely, the β'-phase, which is centro-symmetric ($Pmc2_1$ space group), cannot have a nonzero resultant polarization.

γ-$BaFe_2O_4$ crystals show 120° twining, as a result of the symmetry lowering occurring during the high temperature growth process taking place above 1000°C, from the α-hexagonal to the γ-orthorombic phase. The $Cmc2_1$ phase has raised interest mainly because of its optical properties. In fact, a bandgap of ~1.9 eV (652 nm) has been reported, which places γ-$BaFe_2O_4$ in a category of materials of possible photovoltaic interest [52]. The coexistence of ferroelectricity and photovoltaic properties would open the intriguing possibility of exploiting it as an absorber without the need for junctions (thus allowing a reduced complexity of the device) as the photogenerated electron-hole pair could be separated thanks to the internal electric field generated by the ferroelectric ordering. Although this phenomenon has been known for more than half a century, it has been poorly studied due to the scarcity of materials that exhibit the coexistence of such properties. However, the increasingly urgent search for eco-sustainable methods for obtaining energy has relaunched the research activity on this class of innovative materials [53, 54, 55]. In addition to this, the absorption in the visible region of the electromagnetic spectrum has opened the way to the possible application of BaFeO in the field of photocatalysis. In fact, some papers report the use of γ-$BaFe_2O_4$ as a catalyst in photodecomposition reactions. In particular, it was found that composites based on Pt and BaFeO irradiated with visible light ($\geq$ 420 nm) are able to decompose H_2O to H_2 and isopropanol (C_3H_7OH) to CO_2 in a relatively short time [55]. In another study [57] γ-$BaFe_2O_4$ was exploited for the selective oxidation of styrene to benzaldehyde. By conducting this reaction in a polar and aprotic solvent (e.g. acetone), the conversion of styrene increases up to 45%, with a selectivity of 88.5% and a final 40% yield. Finally, further studies have suggested the application of this material both as a microwave

absorber in the form of a pigment, and as a protector against electromagnetic interference, apparently by virtue of its high magnetization capacity, high coercivity, stability and permittivity [58]. The examples listed here testify to the high multifunctionality of this barium ferrite; therefore, the setting up of a study aimed at thoroughly determining its multiferroic properties would be extremely useful to better understand the specific activity of the material in already known applications, as well as to evaluate its integration into other technological systems.

2.3 References

[1] H.Schmid *"Multi-ferroic magnetoelectrics"* Ferroelectrics (1994), 162, 317-338

[2] W. Chongsheng, L. Qian, W. Yu, C. Jianfeng, C. Yanjun, Y. Qisheng, Z. Huaiwu and L. Yingli *"Nonvolatile eight-state memory prototype based on single-phase multiferroic hexaferrite at room temperature"* Ceramics International (2019), 45, 17152-17156

[3] W. Yanping , G. Cunxu, C. Zhendong, C. Shibo, S. Weixia, Z. Peng, C. Guilin and L. Jiangong *"Four-state memory based on a giant and non-volatile converse magnetoelectric effect in FeAl/PIN-PMN-PT structure"* Sci. Rep. (2016) 6, 30002

[4] N. Spaldin *"Multiferroics beyond electric-field control of magnetism"* Proc. R. Soc. (2020), A 476, 1-17

[5] H. H. Chen and R. K. Joseph *"Exchange interaction model of ferromagnetism"* J. Mat. Phys. (1972), 13, 725-739

[6] N. Hill *"Why are there so few magnetic ferroelectrics?"* J. Phys. Chem. B (2000), 104, 6694-6709

[7] E. Ascher, H. Rieder, H. Schmid and H. *Stössel "Some properties of ferromagnetoelectric nickel iodine boracite, $Ni_3B_7O_{13}I$"* J Appl Phys. (1966), 37, 1404–1405

[8] S.V. Kiselev, R.P. Ozerov and G.S. Zhdanov *"Detection of magnetic order in ferroelectric $BiFeO_3$ by neutron diffraction"* Sov. Phys. Dokl. (1963), 7, 742

[9] R.E. Newnham, J.J. Kramer, W.A. Schulze and L.E. Cross *"Magnetoferroelectricity in Cr_2BeO_4"* J Appl Phys. (1978), 49, 6088–6091

[10] D. Bossini, D.M. Juraschek, R.M. Geilhufe, N. Nagaosa4,5, A.V. Balatsky, M. Milanović, V.V. Srdić, P. Šenjug, E. Topić, D. Barišić, M. Rubčić, D. Pajić, T. Arima, M. Savoini and S.L. Johnson, C.S. Davies and A. Kirilyuk "Magnetoelectrics and multiferroics: theory, synthesis, characterisation, preliminary results and perspectives for all-optical manipulations" J. Phys. D: Appl. Phys. (2023), 56, 273001

[11] I. Bersuker *"The Jahn Teller effect"* Cambridge University Press (2006)

[12] N. Ikeda, H. Ohsumi, K. Ohwada, K. Ishii, T. Inami, K. Kakurai, Y. Murakami, K.

Yoshii, S. Mori, Y. Horibe and H. Kitô *"Ferroelectricity from iron valence ordering in the charge-frustrated system $LuFe_2O_4$"* Nature (2005), 436, 1136

[13] M. Fiebig, T. Lottermoser, D. Meier and M. Trassin *"The evolution of multiferroics"* Nat. Rev. Mater. (2016), 1, 16046

[14] J.B. Goodenough *"Theory of the Role of Covalence in the Perovskite-Type Manganites [La, M(II)]MnO_3"* Phys. Rev. (1955), 100, 564

[15] J. L. MacManus-Driscoll, A. Sharma, Y. Bugoslavsky, W. Branford, L. F. Cohen and M. Wei *"Reversible Low-Field Magnetoresistance in $Sr_2Fe_{2-x}Mo_xO_{6-\delta}$ by Oxygen Cycling and the Role of Excess Mo ($x > 1$) in Grain-Boundary Regions"* Adv. Mat. (2006), 18, 900-904

[16] K.I. Kobayashi, T. Kimura, H. Sawada, K. Terakura and Y. Tokura *"Room-temperature magnetoresistance in an oxide material with an ordered double-perovskite structure"* Nature (1998), 395, 677–680

[17] R. Nechache, C. Harnagea, A. Pignolet, F. Normandin, T. Veres, L.P. Carignan and D. Ménard *"Growth, structure, and properties of epitaxial thin films of first-principles predicted multiferroic Bi_2FeCrO_6"* Appl. Phys. Lett. (2006), 89, 102902

[18] R. Nechache, C. Harnagea and A. Pignolet *"Multiferroic properties—structure relationships in epitaxial Bi_2FeCrO_6 thin films: recent developments"* J. Phys.: Condens. Matter (2012), 24, 096001

[19] T. Zhao, A. Scholl, F. Zavaliche, K. Lee, M. Barry, A. Doran, M. P. Cruz, Y. H. Chu, C. Ederer, N. A. Spaldin, R. R. Das, D. M. Kim, S. H. Baek, C. B. Eom and R. Ramesh *"Electrical control of antiferromagnetic domains in multiferroic $BiFeO_3$ films at room temperature"* Nat. Mat. (2006), 5, 823–829

[20] J. C. Yang, Y. L. Huang, Q. He and Y. H. Chu *"Multifunctionalities driven by ferroic domains"* J. Appl. Phys. (2014), 116, 066801

[21] M. P. Cruz, Y. H. Chu, J. X. Zhang, P. L. Yang, F. Zavaliche, Q. He, P. Shafer, L. Q. Chen, and R. Ramesh *"Strain Control of Domain-Wall Stability in Epitaxial **BiFeO3** (110) Films"* Phys. Rev. Lett. (2007) 99, 217601

[22] S. Y. Yang, J. Seidel, S. J. Byrnes, P. Shafer, C.-H. Yang, M. D. Rossell, P. Yu, Y.-H.

Chu, J. F. Scott, J. W. Ager III, L. W. Martin and R. Ramesh *"Above-bandgap voltages from ferroelectric photovoltaic devices"* Nature Nanotechnology (2010), 5, 143–147

[23] Y.H. Chu, Lane W. Martin, Mikel B. Holcomb, M. Gajek, S.J. Han, Q. He, N. Balke, C.H. Yang, D. Lee, W. Hu, Q. Zhan, P.L. Yang, A. Fraile-Rodríguez, A. Scholl, S.X. Wang and R. Ramesh *"Electric-field control of local ferromagnetism using a magnetoelectric multiferroic"* Nat. Mat. (2008), 7, 478-482

[24] J. Allibe, S. Fusil, K. Bouzehouane, C. Daumont, D. Sando, E. Jacquet, C. Deranlot, M. Bibes and A. Barthélémy *"Room temperature electrical manipulation of giant magnetoresistance in spin valves exchange-biased with $BiFeO_3$"* Nano Lett. (2012), 12, 1141–1145

[25] P. Maksymovych, J. Seidel, Y. H. Chu, P. Wu, A. P. Baddorf, L.Q. Chen, S. V. Kalinin and R. Ramesh *"Dynamic Conductivity of Ferroelectric Domain Walls in $BiFeO_3$"* Nano Lett. (2011), 11, 5, 1906–1912

[26] Y.H. Chu, Q. Zhan, C.H. Yang, M.P. Cruz, L.W. Martin T. Zhao, P. Yu, R. Ramesh, P.T. Joseph, I.N. Lin, W. Tian and D. G. Schlom *"Low voltage performance of epitaxial BiFeO3 flms on Si substrates through lanthanum substitution"* Appl. Phys. Lett. (2008), 92, 102909

[27] N. Hur, S. Park, P.A. Sharma, J.S. Ahn, S. Guha and S-W. Cheong *"Electric polarization reversal and memory in a multiferroic material induced by magnetic fields"* Nature (2004), 429, 392–395,

[28] T. Kimura, T. Goto, H. Shintani, K. Ishizaka, T. Arima and Y. Tokura *"Magnetic control of ferroelectric polarization"* Nature (2003), 426, 55–58

[29] T. Kimura, G. Lawes, T. Goto, Y. Tokura, and A.P. Ramirez *"Magnetoelectric phase diagrams of orthorhombic $RMnO_3$ (R=Gd, Tb, and Dy)"* Phys. Rev. (2005), B71, 224425

[30] T. Kimura, Y. Sekio, H. Nakamura, T. Siegrist and A.P. Ramirez *"Cupric oxide as an induced-multiferroic with high T_C"* Nat. Mat. (2008), 7, 291-294

[31] S. Ishiwata, Y. Taguchi, H. Murakawa, Y. Onose and Y. Tokura *"Low-magnetic-field control of electric polarization vector in a helimagnet"* Science (2008), 319, 1643-1646

[32] G. Guthrie and P.J. Heaney "Mineralogical characteristics of the silica polymorphs

in relation to their biological activities" Scandinavian Journal of Work Environment & Health (1993), 21, 5-8

[33] https://serc.carleton.edu/download/images/8743/sio2.jpg

[34] A.K.A. Pryde and M.T. Dove *"On the Sequence of Phase Transitions in Tridymite"* Phys. Chem. Minerals (1998), 26, 171–179

[35] K. Kihara, T. Matsumoto and M. Imamura *"Structural change of orthorhombic-I tridymite with temperature: A study based on second-order thermal-vibrational parameters"* Zeitschrift fur Kristallographie (1986), 177, 27-38

[36] D.C. Palmer *"Stuffed derivatives of the silica polymorphs"*, Rewiews in Mineralogy (1994), 29, 83-122

[37] D.D. Engelsen, G.R.Fern, T.G. Ireland, F. Yang and J. Silver *"Photoluminescence and cathodoluminescence of $BaAl_2O_4:Eu^{2+}$ and undoped $BaAl_2O_4$: evidence for F-centres"* Opt. Mat. Express (2020), 10, 1962-1980

[38] J. Li, X. K. Lan, K. Du, X. Q. Song,W. Z. Lu, X. H. Wang and W. Lei *"Ultrabroad temperature stability of stuffed tridymite-type $BaAl_2O_4$ co-doped by $[Zn_{0.5}Ti_{0.5}]^{3+}$ with weak ferroelectricity"* Ceramics International (2019), 45, 22493- 22497

[39] V. Kahlenberg, R.X. Fischer and C.S.J. Shaw *"Polymorphism of Strontium Monogallate: The Framework Structures of β-$SrGa_2O_4$ and ABW-Type γ-$SrGa_2O_4$"* Journal of Solid-State Chemistry (2000), 153, 294-300

[40] S. Liu, S. Ma, S. Wang and Z. Ye *"Exploring crystal-field splittings of Eu3+ ions in γ- and β-SrGa2O4"* Journal of Luminescence (2019) 210, 155-163

[41] T. Wang, X. Xu, D. Zhou, Y. Yang, J. Qiu and X. Yu *"Effect of Defect Distribution on the Optical Storage Properties of Strontium Gallates with a Low-Dimensional Chain Structure"* Inorganic Chemistry (2016), 55, 894-901

[42] E. Tanaka, Y. Ishii, H. Tsukasaki, H. Taniguchi and S. Mori *"Structural changes and microstructures in stuffed tridymite-type compounds $Ba_{1-x}Sr_xAl_2O_4$"* Jpn. J. Appl. Phys. (2014), 53, 09PB01

[43] J. Choisnet, V. Caignaert and B. Raveau "*A germanoferrite with the real stuffed tridymite type structure: $K_{0.75}Ba_{0.25}Fe_{1.25}Ge_{0.75}O_4$*" J. Mater. Chem**.** (2004),14, 2438-2442

[44] A. Bhim, J.P. Sutter, J. Gopalakrishnan, S. Natarajan *"Stuffed Tridymite Structures: Synthesis, Structure, Second Harmonic Generation, Optical, and Multiferroic Properties"* Chem. A European J. (2020), 27, 1995-2008

[45] Y. Xiaomeng, L. Hui, Z. Dawei, H. Ruijin, T. Chunxian, H. Zhaoxia, Z. Shengming, Z. Zhi-Jun and Z. Guanhaoije *"$BaAl_2O_4:Eu^{2+}$-Al_2O_3 ceramics for wide range optical temperature sensing"* Dalton transactions (2022), 51, 1784-1790

[46] K. Fukuda and K. Fukushima *"Crystal structure of hexagonal $SrAl_2O_4$ at 1073 K"* Journal of Solid-State Chemistry (2005), 178, 2709-2714

[47] R.E. Marsh and I. Bernal *"More space-group changes"* Acta crystallographica (1995), 51, 300-307

[48] V. Kahlenberg and R.X. Fischer *"Structural Characterization of Strontium Monoferrite $SrFe_2O_4$, a new Stuffed Framework Compound"* Solid State Sciences (2001), 3, 433-439

[49] V. Kahlenberg, R.X. Fischer and J.B. Parise *"The Stuffed Framework Structure of $BaGa_2O_4$"* J. Solid State Chem. (2000), 154, 612-618

[50] H. Mitsuda, S. Mori and C. Okazaki *"The Crystal Structure of Barium Monoferrite, $BaFe_2O_4$"*, Acta Crystallographica (1971) 27, 1263-1269

[51] S. Meriani *"Polymorphism of Barium Monoferrite, $BaFe_2O_4$"* Acta Crystallographica (1972), 28, 1241-1243

[52] H. Huang *"Solar energy: Ferroelectric photovoltaics"* Nat. Photonics (2010), 4, 134-135

[53] M. Ichiki, R. Maeda, Y. Morikawa, Y. Mabune, T. Nakada and K. Nonaka *"Photovoltaic effect of lead lanthanum zirconate titanate in a layered film structure design"* Appl. Phys. Lett. (2004), 84, 395–397

[54] L. Pintilie, I. Vrejoiu, G. Le Rhun and M. Alexe *"Short-circuit photocurrent in epitaxial lead zirconate-titanate thin films"* J. Appl. Phys. (2007), 101, 064109

[55] B. Xu, D.J. Singh, V.R. Cooper and Y.P. Feng *"Design of a low band gap oxide ferroelectric: $Bi_6Ti_4O_{17}$"* Europhysics Letters (2011), 94, 37006

[56] P. H. Borse, C. R. Cho and K. T. Lim *"Synthesis of Barium Ferrite for Visible Light Photocatalysis Applications"* J. Korean Phys. Soc. (2011), 58, 1672-1676

[57] R.Y. Pawar and S.K. Pardeshi *"Selective oxidation of styrene to benzaldehyde using soft BaFe2O4 synthesized by citrate gel combustion method"* Arab. J. Chem. (2018), 11, 282-290

[58] M.C. Dimri, H. Khanduri, P. Agarwal, J. Pahapill and R. Stern "*Structural, magnetic, microwave permittivity and permeability studies of barium monoferrite ($BaFe_2O_4$)"* J. Magn. Magn. Mater. (2019), 486, 165278

3 γ-Phase Barium monoferrite stuffed-tridymite: bulk and single-crystal characterization

3.1 Methods

3.1.1 Synthesis

Polycrystalline BaFeO samples were prepared via solid-state reaction, starting from equimolar amounts of $BaCO_3$ and Fe_2O_3, which are then finely ground in an agate mortar. This step is crucial to minimize the formation of byproducts such as $BaFe_{12}O_{19}$, featured by a large ferromagnetic component compared to BaFeO. The reaction involves the thermal decomposition of $BaCO_3$ into CO_2 and BaO, which is highly unstable and, therefore, able to increase the reaction rate. The solid solution is fired at 1573 K for 12 h, in air; the cooling step occurs in the switched off furnace, following its thermal inertia. The *β*'-polymorph was obtained by preparing the same solid matrix, which was treated at 1173 K (12 h, in air) and then quenched at the same temperature.

BaFeO single crystals were prepared via melt synthesis, by using an iron-rich mixture ($BaCO_3/Fe_2O_3$ molar ratio 0.45/0.55), which then undergoes a specific treatment: the solid matrix is heated at 1613 K with a rate of 0.5°/min for 8 h; then, the mixture is cooled down to RT at 2°/min. The obtained crystals are washed with a HNO_3 acid solution (0.1N) in order to remove the mixture residuals.

Ceramic pellets were prepared by pressing BaFeO powders, which were previously washed with a HNO_3 aqueous solution (0.1 N) in order to remove impurities that can affect the final mechanical properties of the pellet, at 200 bar. Different sizes were obtained (0.3 – 2.5 cm diameter and 0.2 – 5 mm thickness). The final sintering step is conducted in a furnace at 1273 K for 24 h in air. An in-depth study of the BaFeO pellet is illustrated in chapter 4.

3.1.2 Diffraction techniques, Raman spectroscopy and transmission electron microscopy

All polycrystalline BaFeO samples were checked by means of powder X-ray diffraction

(PXRD), performed on a Rigaku Smartlab XE diffractometer. The instrument uses a Cu-source (K_α wavelength, λ = 1.5406 Å) and is equipped with a Ni filter to eliminate the K_β contribution. 5.0° Soller slits were used both on the incident and the diffracted beam, coupled with a 5 mm length-limiting slit. All measurements were collected in Bragg-Brentano geometry with an HyPix3000 detector in X-rays fluorescence reduction mode, given the presence of iron-based compounds. The obtained BaFeO powder patterns (collected in 10-120° 2θ range for structure refinement, in 10-80° 2θ range for phases check measurements) were refined by means of Rietveld method, performed using the GSASII software [1].

Single-crystal diffraction (SCXRD) data were collected using a Bruker Smart diffractometer, equipped with a Smart Breeze CCD detector, and a graphite monochromatized Mo K_α radiation (λ = 0.71073 Å) as the incident beam. Intensities were integrated using SAINT [2] considering the presence of six twin domains and data reduction was performed with the TWINABS program, which allowed to scale the intensities related to twin variants. The structure was solved using SHELXT. Finally, the refinement was carried out using SHELXL, with anisotropic displacement parameters for all atoms [3, 4].

Time-of-flight data were collected on the WISH (Wide angle In a Single Histogram) diffractometer at the ISIS facility (UK) [5]. The sample is placed in a thin-walled vanadium can and irradiated by white neutron pulses (with a wavelength in the 1.5 – 15 Å range) generated by a spallation source. The WISH instrument has a flight path of 40 m and is equipped with an 8 mm diameter-^{3}He gas tubes detector covering 160° of 2θ. The diffraction data were collected in the temperature range 300–1038 K in a standard RAL5 furnace. High statistic data were collected at 300 and 1038 K, whereas shorter measurements were captured every 10 K, with detector banks at average 2θ of 152.7,121.66, 90 and 58.33°. Neutron diffraction data and group theory calculations were processed using the ISODISTORT and JANA2006 softwares, respectively [6, 7].

Raman spectroscopy was exploited for the analysis of samples prepared via solid-state reaction. The micro-Raman spectrometer Horiba LabRam HR Evolution Raman was used with a confocal Olympus microscope and 10×, 50×, ULWD50×, 100× objectives (with spatial resolutions of ~1 μm). The Micro-Raman setting is also equipped with an He-Ne laser emitting at 632.8 nm, BraggRate Notch Filters, Silicon CCD + InGaAs Diode Array

detectors, gratings 300–600–1800 lines/mm, and density filters. The spectrometer was calibrated using the standard silicon Raman peak at 520.6 cm^{-1}. The measurements were collected using the 100× objective, for 30 s and four repetitions, using a 5% density filter.

Transmission electron microscopy (TEM) measurements were carried out on a Philips TECNAI F20 instrument, operating at 200 kV, in collaboration with CNR-IMM Institute in Bologna (IT). The powder sample was ground in isopropanol to get a suspension, which is then deposited on a copper grid covered with a holey carbon film. High resolution images (HREM) and selected area electron diffraction (SAED) experiments were carried out at room temperature.

3.1.3 Electric measurements

The dielectric and ferroelectric measurements were carried out in collaboration with the CNR-IMEM institute in Parma.

The AC electric resistivity was measured in a four-contact configuration in the temperature range 110 – 370 K. The dielectric constant ε_R was measured with a LCR meter HP4824A at 1 KHz frequency, by applying a sinusoidal signal of 100 mV. The dielectric losses were quantified by a capacitance measurement performed in staircase mode with 100 Hz sinusoidal modulation (maximum voltage amplitude of 1700 V).

Ferroelectric measurements were carried out by a TF-Analyzer 2000E (produced by AIXACCT GmbH). The disc-shaped pellet samples were lapped on both surfaces and then metalized by RT-sputtering with ~ 300 nm of gold, in order to get gold layers to be contacted with 100 μm diameter gold wires, by using conductive silver-based paste. The application of Positive-Negative protocol involves three different steps (Figure 1): the measurement starts with a trapezoidal write pulse, featured by rise-time and maximum amplitude retention time both of 5 ms; the following two read pulses of 100 Hz, with a delay time of 1 second, induce the “opening” of the hysteresis loop. The measurements were performed exploring the 100–1000 Hz frequency range at maximum applied voltage amplitude was 1500 V. Unlike standard Positive Up Negative Down (PUND), this protocol avoids the occurrence of dielectric breakdown.

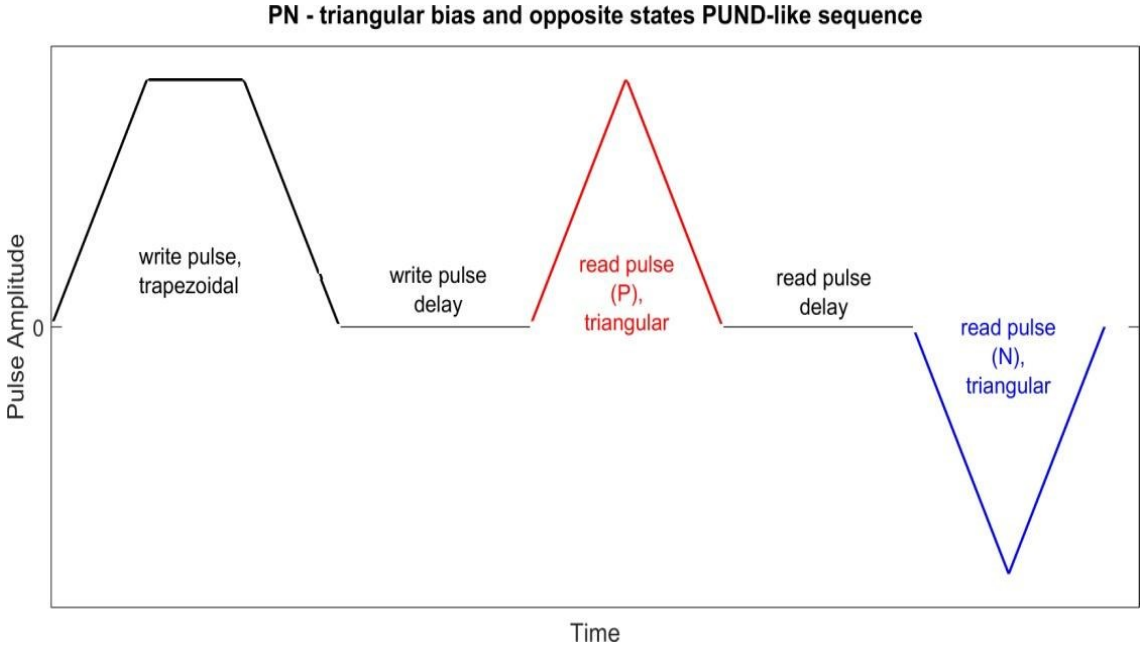

Figure 1 - PN time sequence of triangular pulses exploited to get a complete P(E) hysteresis loop.

Piezoresponse force microscopy (PFM) measurements were carried out in collaboration with the Institute for Materials Science and Center for Nanointegration Duisburg-Essen (CENIDE) and were collected using an MFP-3D atomic force microscope (Asylum Research). A cantilever-tip assembly Multi75E-G with spring constant 3 N/m and Pt/Cr conductive coating was used. The PFM images were collected at AC voltage by applying 10 V amplitude and 300 kHz frequency to the tip. The piezoresponse hysteresis loops were measured in dual amplitude resonance tracking PFM mode, which involves a sequence of DC voltage pulses applied to the PFM tip. Between the pulses, the PFM response was measured by applying a 3V amplitude AC voltage. The pulse duration was 50 ms. The PFM data were processed using the Gwyddion software [8]. The main contribution to the PFM-based study is to be ascribed to Dr. Vladimir Shvartsman (CENIDE, University of Duisburg-Essen).

3.1.4 Magnetic measurements

Magnetic measurements were carried out using a Quantum Design MPMS 3 Squid magnetometer located at the ISIS material characterization laboratory (UK) equipped with an oven for measurements in the temperature range 400–1000 K. A small ceramic fragment (8.97 mg) of the sample was used for the measurements and ZINCAR cement was employed to allow for good thermal contact and conduction with the oven probe. DC

zero-field cooling (ZFC) and field-cooled cooling (FCC) measurements were performed with selected applied field values in the range 0.01-2 T. Magnetization versus field measurements were performed with the same sample set up at temperatures of 300, 800 and 1000 K in the field range ±50000 Oe. In this specific work, Dr. Fabio Orlandi (ISIS, UK) made significant contributions to the processing and analysis of the experimental data.

3.2 Results and Discussion

3.2.1 Structural characterization

I. Symmetry

The preparation of an iron-rich mixture is essential to induce partial melting and, thus, create an environment favorable for the formation of nucleation centers and for the subsequent separation from the melt and the crystals growth. The $BaO\text{-}Fe_2O_3$ system is indeed characterized by a maximum congruent melting temperature, as evident from the corresponding phase diagrams; consequently, the deviation, albeit slight, from the reference stoichiometry guarantees an inevitable partial fusion of the solid mixture (Figure 2).

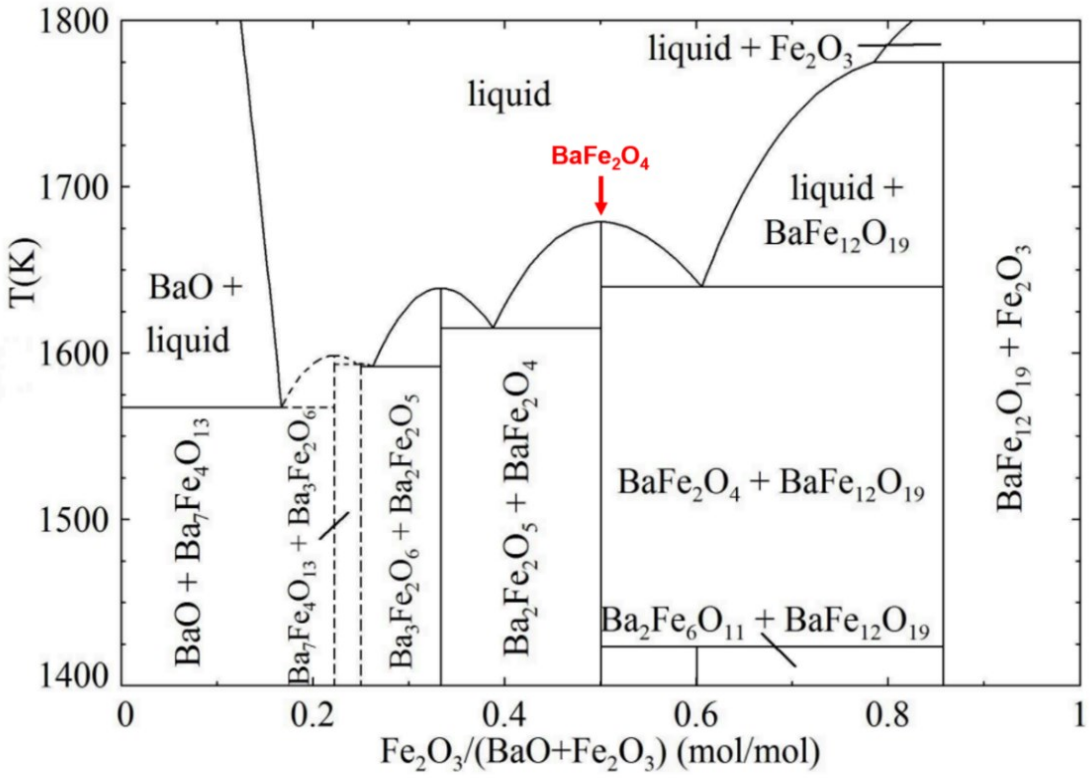

Figure 2 – $BaO\text{-}Fe_2O_3$ system phase diagram [9]. The red arrow indicates the congruent melting point of the $BaFe_2O_4$ composition.

The obtained crystals, having a slightly elongated shape and a reddish colour, are suitable for structural analysis using single-crystal X-ray diffraction (SCXRD) techniques.

The reciprocal lattice can be indexed using a hexagonal crystal system, with cell

parameters a=b=18.998 Å, c=8.437 Å, $\alpha=\beta=90°$ and $\gamma=120°$. However, structure solution and refinement does not allow to obtain reliable results. The literature (see paragraph 2.2.3) suggests that BaFeO crystals in the γ-orthorhombic phase are actually twinned. This is indeed the direct consequence of the lowering of symmetry undergone by the system upon cooling: during the phase transition, the α-hexagonal polymorph, stable at high temperature (T > 1000°C), undergoes a distortion that results in the disappearance of its characteristic 6-fold rotation symmetry axis, thus suggesting that a rearrangement of the crystal lattice, has occurred; at this point, the γ-polymorph can form simultaneously in its three equivalent twin variants (six, if non-centrosymmetric variants are considered), with their [h00]-direction running along the three equivalent (110)-planes belonging to hexagonal symmetry, so that the orthorhombic (h00)-planes appear to be rotated by 120° and parallel to the hexagonal (00l)-planes. Therefore, the complex twinning generates a pattern in which some reflections of the three different domains are perfectly superimposed in reciprocal space (grey spots in Figure 3).

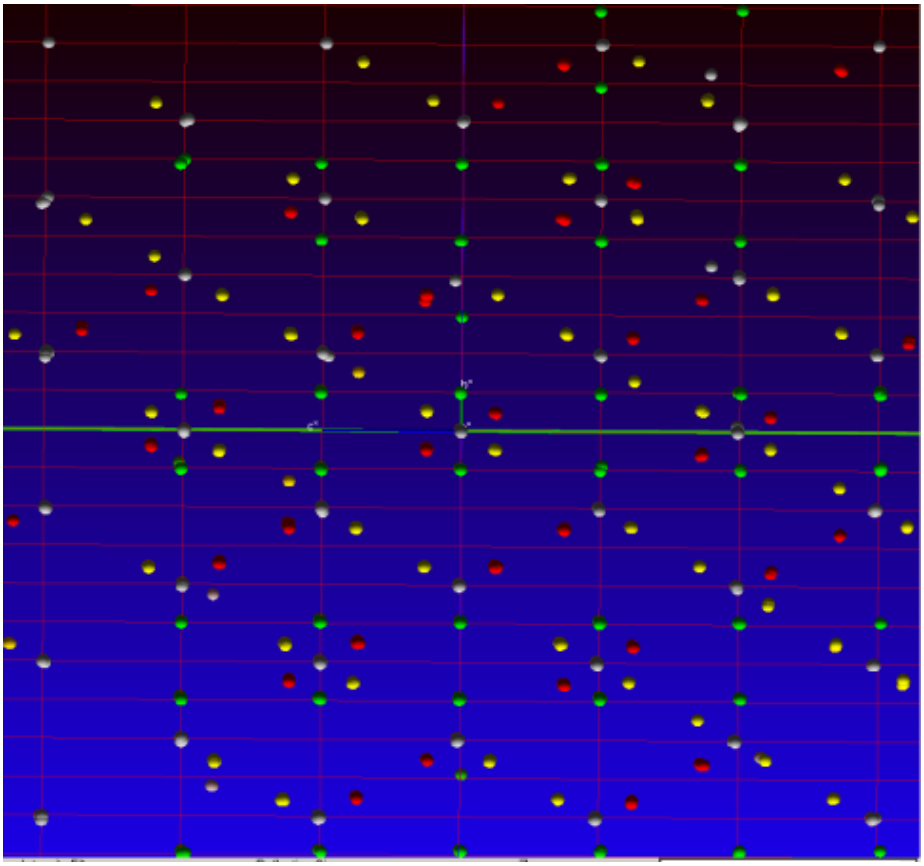

Figure 3 – Reciprocal space of a BaFeO crystal from SCXRD. Red, yellow and green spots represent the reflections belonging to the three twin variants, while grey ones are the result of their superposition.

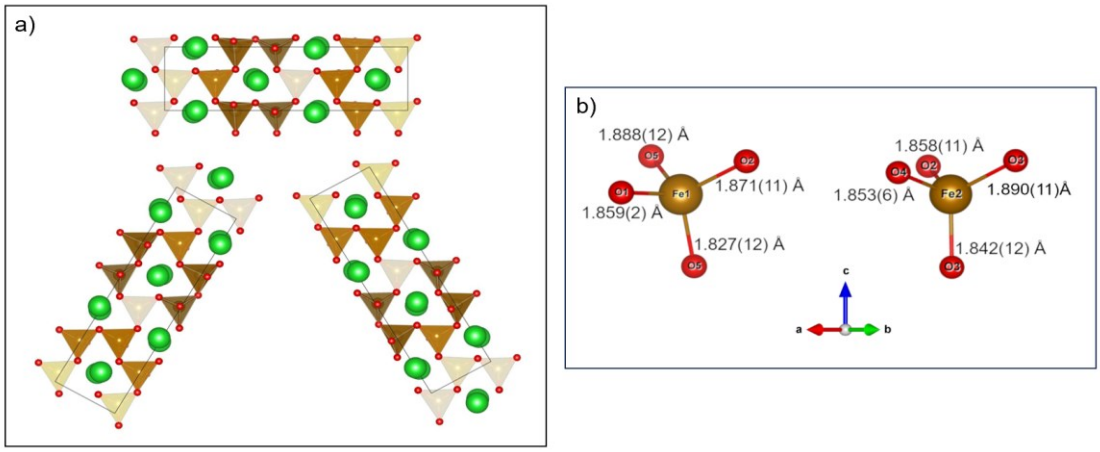

Figure 4 – a) BaFeO unit cells resulting from the three twin domains. Green, brown and red spheres represent barium, iron and oxygen ions, respectively. b) FeO_4 tetrahedra formed by different iron ions. The shortest Fe-$O_{3/5}$ bond is directed towards the c-axis.

The indexing of the different reflection groups allowed the definition of three orthorhombic cells, with cell parameters a = 8.437(5) Å, b = 18.998(12) Å, c = 5.384(3) Å and V = 863.0(9) $Å^3$, rotated by 120° (Figure 4a). Diffraction spots were integrated taking into account the weight of the three twin domains for overlapping reflections, scaling the intensities by using the TWINABS software. The applied matrix related to the present twin law is [0.5 0.5 0; 1.5 -0.5 0; 0 0 -1]. According to the systematic absences (*hkl* with $h + k = 2n + 1$ and *h0l* with $l = 2n + 1$) observed for the experimental data, the choice of the proper space fell on centrosymmetric *Cmcm* (n. 63) and non-centrosymmetric $Cmc2_1$ (n. 36). However, the refinement using the former did not allow obtaining a reliable model, with an implausible 7-fold coordination of the iron ions and a high R_1 reliability factor of ≈ 14 %. Conversely, the space group $Cmc2_1$ (n. 36), belonging to the polar *mm2* point group, proved to be a reliable model, as already demonstrated by previous studies (see paragraph 2.2.3). The final agreement indices are $R_1 = 0.0618$, $wR_2 = 0.0918$ and GooF = 1.072 for 1025 independent reflections and 72 parameters.

Given these results, the so-synthetized γ-BaFeO crystals appears to be a stuffed-tridymite compound characterized by an "up-up-up-up-up-down" (UUUUUD) pattern of the FeO_4 tetrahedra giving rise to the triangular channels along the [100] direction occupied by the Ba^{2+} ions. Noteworthy, the FeO_4 tetrahedra are characterized by a slight shift of the central Fe^{3+} ion from the barycenter of the coordination geometry. This off-centering also influences the different Fe-O bond lengths and is responsible for the formation of

electrical dipoles oriented along the polar axis of the crystal, parallel to the c vector, and, potentially, for the establishment of a long-range ferroelectric order. However, the observed twinning does not allow to determine whether the detected shift is oriented along the positive or negative direction of the polar axis. The average bond length determined for the two iron positions (Fe1 and Fe2) is 1.861(9) and 1.861(10), respectively, in agreement with the high-spin configuration predicted for iron (III) atoms in tetrahedral coordination. Figure 4b shows a detailed representation of the Fe-O coordination system, while the results of the structural refinement are summarized in the table below (Table I).

Table I – Summary of BaFeO crystal data and its refinement parameters. Atomic parameters were anisotropically refined. s.o.f values are 1 for each atom.

$BaFe_2O_4$, 293K s.g. *Cmc2₁* (36) a = 8.437(5), b = 18.998(12), c = 5.384(3) Å V = 863.0(9) Å³ ρ= 4.819 g/cm³ Z=8 Formula weight, 313.04 g/mol										
Wavelength		MoKα (0.71073 Å)			Reflections		1025			
μ		15.537			Reflections (I > 2\s(I))		828			
F(000)		1120.0			Parameters/restraints		72/31			
h		12			R1		0.0618			
k		27			R (I>2\s(I))		0.0409			
l		7			wR2		0.0918			
θmin- θmax		2.144- 31.442			wR (I > 2\s(I))		0.0847			
Tmin-Tmax		0.339-0.7462			GooF (S)		1.072			
Atom	x	y	z	U_{11}	U_{22}	U_{33}	U_{23}	U_{13}	U_{12}	U_{eq}
Ba1	0	0.13088(8)	-	0.0091(4)	0.0144(6)	0.0245(12)	0.0007(7)	0	0	0.0160(4)
Ba2	0.5	0.11813(7)	0.9643(3)	0.0101(4)	0.0148(6)	0.0207(10)	0.0002(8)	0	0	0.0152(3)
Fe1	0.27980(18)	0.04368(13)	0.4703(5)	0.0097(8)	0.0116(10)	0.0160(13)	0.0004(12)	0.0013(14)	-	0.0124(4)
Fe2	0.29090(19)	0.20941(11)	0.4889(5)	0.0090(8)	0.0116(10)	0.0152(13)	-0.0008(11)	0.0027(15)	0.0010(9)	0.0119(5)
O1	0.5	0.0467(7)	0.479(3)	0.016(4)	0.019(5)	0.020(5)	0.001(5)	0	0	0.019(3)
O2	0.2091(17)	0.1267(5)	0.621(3)	0.024(4)	0.010(4)	0.024(5)	0.001(3)	0.003(4)	-0.002(4)	0.019(4)
O3	0.215(12)	0.2916(5)	0.647(2)	0.012(4)	0.016(4)	0.013(4)	-0.003(3)	-0.004(4)	0.006(4)	0.014(2)
O4	0.5	0.2165(8)	0.591(3)	0.023(5)	0.024(5)	0.028(6)	-0.005(4)	0	0	0.025(4)
O5	0.2216(12)	0.0387(6)	0.144(2)	0.022(4)	0.018(4)	0.014(4)	-0.003(4)	-0.002(4)	0.007(4)	0.018(2)

A further structural analysis performed by Transmission Electron Microscopy (TEM) on a sintered pellet sample of γ-BaFeO (1000°C, 24h) confirmed the single crystal XRD results. The use of the previously described orthorhombic cell allows to index the entire group of reflections observed in [001] and [210] projections by selected area electron diffraction (SAED, Figure 5). No extra reflections apart from those associated with the previously described cell are identified. Moreover, the pattern shows the presence of the 120° twinning, in agreement with what is observed by X-ray diffraction. Figure 6 shows a series of high-resolution TEM images (HREM) taken along the [100] direction, together with the related Fast Fourier Transform, in which 60° and 120° twin boundaries are apparent.

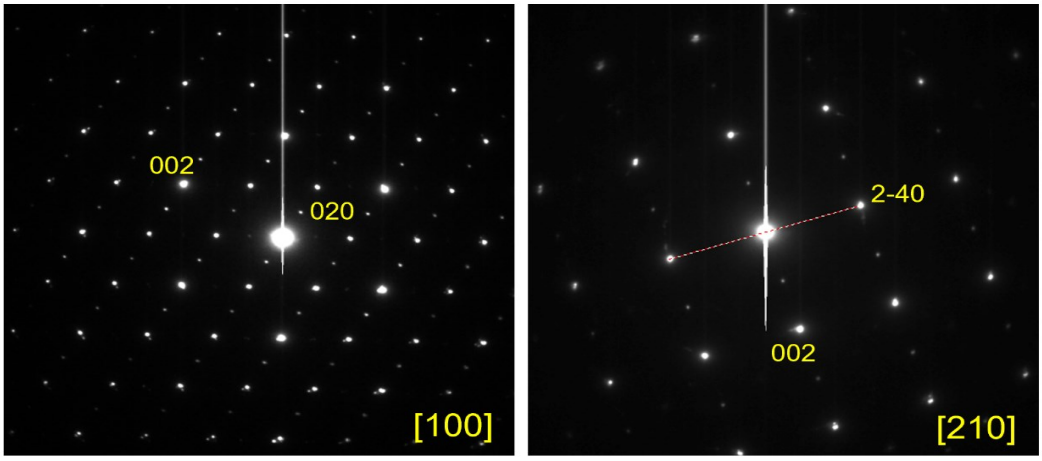

Figure 5 – Results from selected area electron diffraction collected along the [100] (on the left) and [210] (on the right) zone axes.

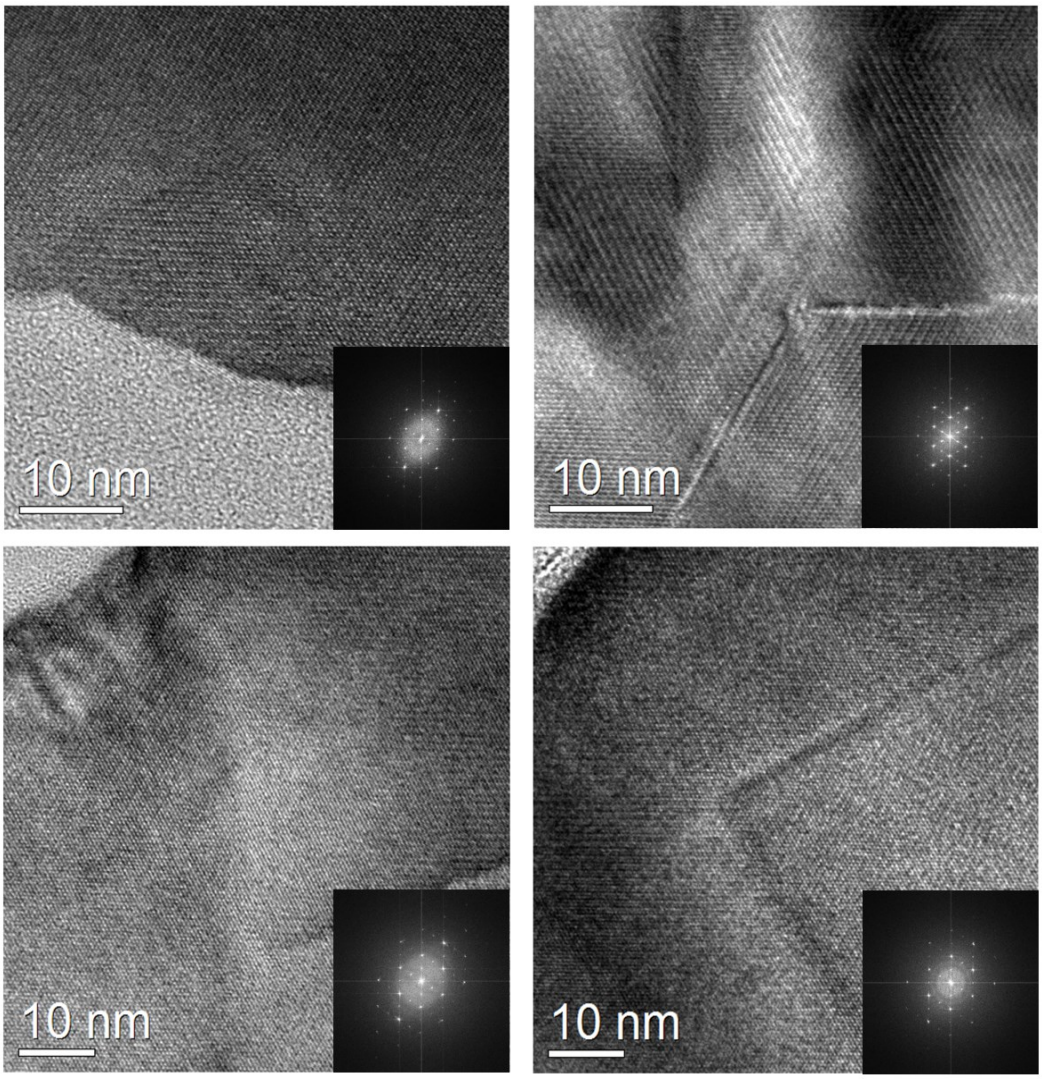

Figure 6 – High-resolution images recorded along the [100] zone axis. The insets show the corresponding fast Fourier transforms.

II. Bulk

Polycrystalline BaFeO samples were analyzed via Rietveld refinement, using the structure obtained by single crystal XRD as the starting model. Good agreement between the observed and calculated data was obtained, with R ~ 7%, and cell parameters a=8.4484(7), b=19.0618(17) and c=5.3860(5) Å (Figure 7).

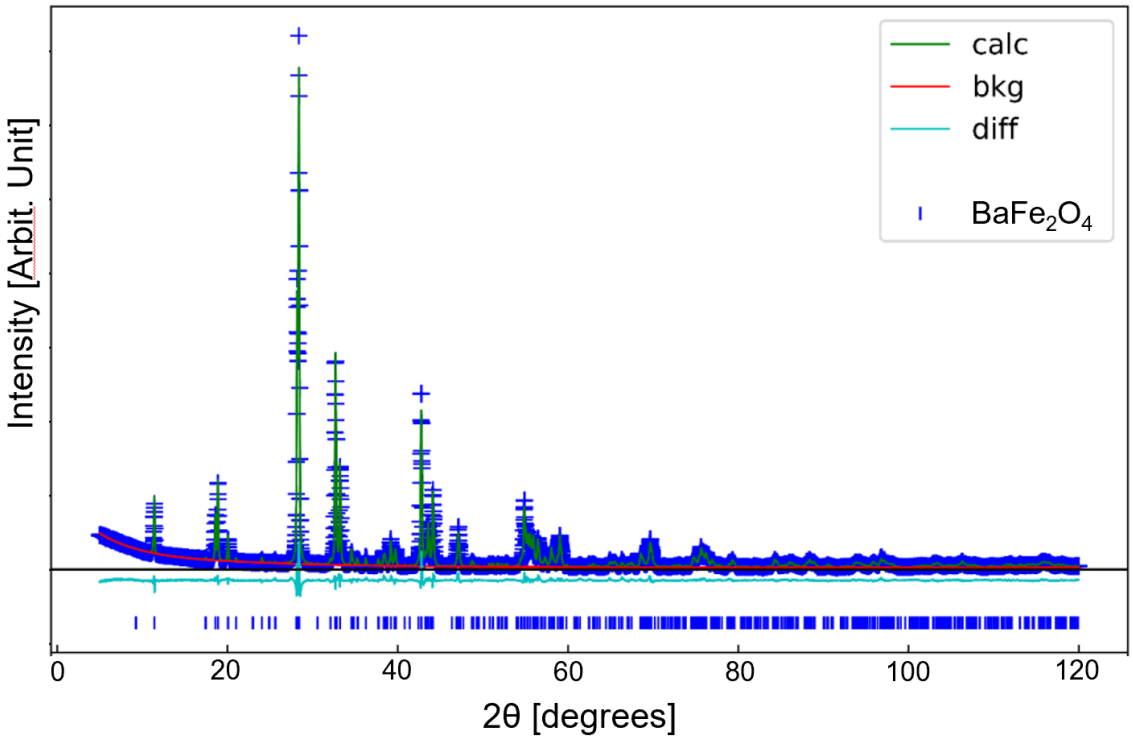

Figure 7 – Rietveld plot of BaFeO PXRD data.

Considering the reported polymorphism of BaFeO, a sample of *β'*-phase was synthesized in order to determine its X-ray diffraction and Raman patterns and exclude its presence as a byproduct of the synthesis described above. This phase, although metastable, has is kinetically favored by a rapid cooling from high temperature. Figure 8a shows the PXRD pattern obtained for the two phases, pointing out a fairly similar distribution of reflections, precisely due to the structural similarities: in fact, the main differences between the *β'*- and *γ*-orthorhombic lattices consist in the different tilting of the FeO_4 tetrahedra (Figure 8c, d). Within this framework, the measurements obtained from Raman spectroscopy have been extremely useful in discriminating between the two phases (Figure 8b). In fact, by superimposing the two spectra, it is possible to identify some Raman bands, including

those at 573 cm^{-1} and 625 cm^{-1}, which are uniquely attributable to the *β'*-phase and, most importantly, are completely absent in the pattern of the *γ*-phase; moreover, considering the absence of preferential orientations, the distribution of the relative intensities of the vibrational modes is also clearly different. Therefore, it is possible to state that, within the detection limits of the used techniques, the presence of *β*'-phase can be ruled out.

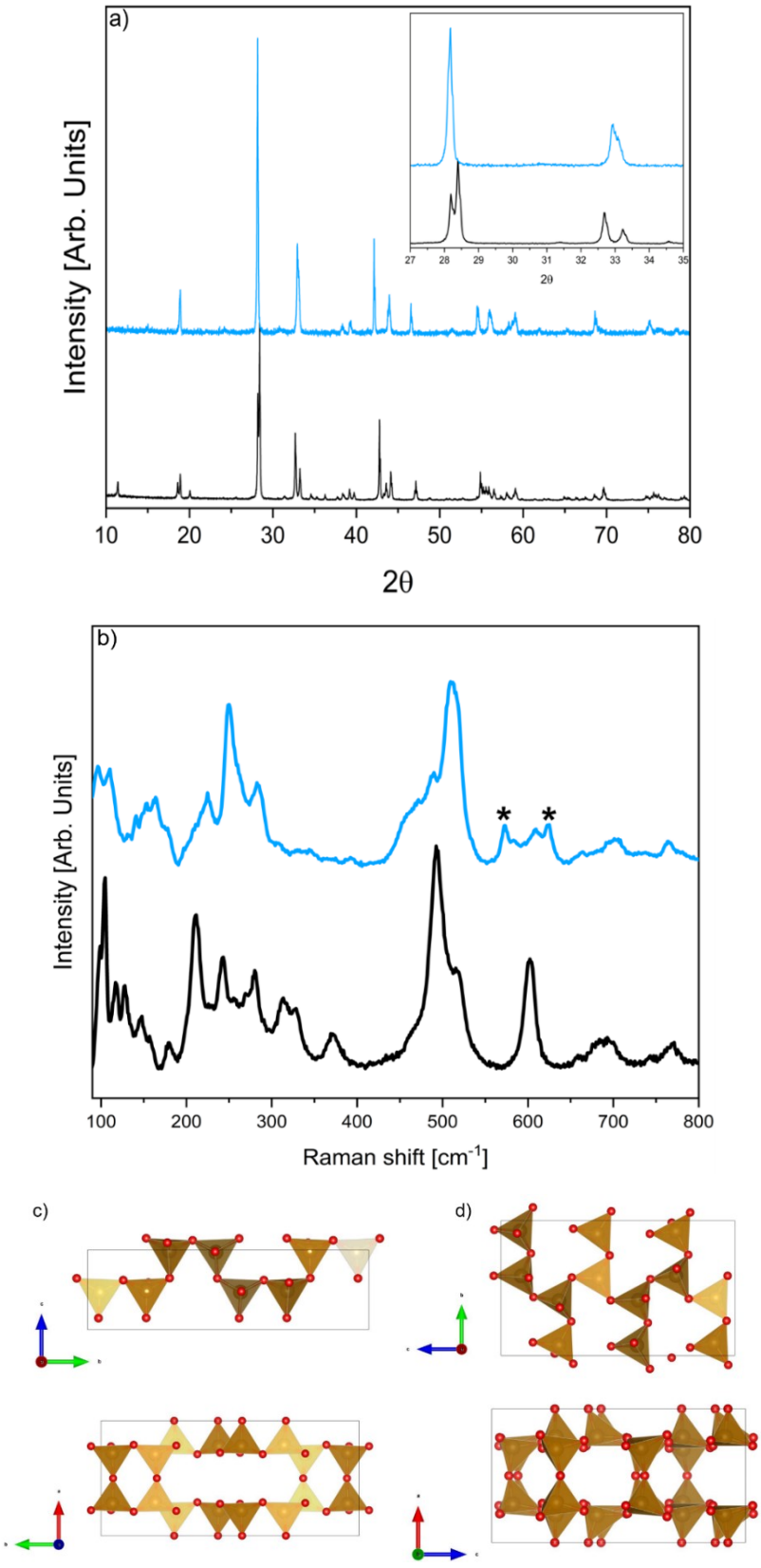

*Figure 8 – Comparison between γ- (black) and β'- (blue) BaFeO phases. (a): PXRD, (b) Raman. Black * indicates some peaks uniquely attributable to the β'-polymorph. The projection of the tetrahedra patterns along [100] and [001] directions for γ- phase and along [100] and [010] for β'-phase are shown.*

3.2.2 Electric characterization

Electric characterization of polycrystalline BaFeO samples was carried out on a polycrystalline ceramic pellet, produced by means of a specific sintering process (for the detailed purity analysis on the BaFeO pellet see paragraph 4.3.1). The temperature dependence of AC electrical resistivity (ρ) and dielectric constant (ε_R) were measured from T = 114 K to T = 370 K at 1 KHz (Figure 9a, b). ρ appears to be almost constant below T ~ 310 K, where a significant drop of about one order of magnitude is observed. This behaviour is describable by the Arrhenius equation $\rho = \rho_0 \exp(E_\rho/kT)$ formula, here with an activation energy E_ρ ~0.30 eV, which suggests that an unspecified thermally activated conductive mechanism has taken place, modifying the mobility of charge carriers of the material. A similar trend is observed for the dielectric constant, showing a variation of the trend linear at low temperatures and an exponential rise above ~310 K. However, it is important to consider that this phenomenon does not necessarily involve a symmetry transition of the crystal lattice.

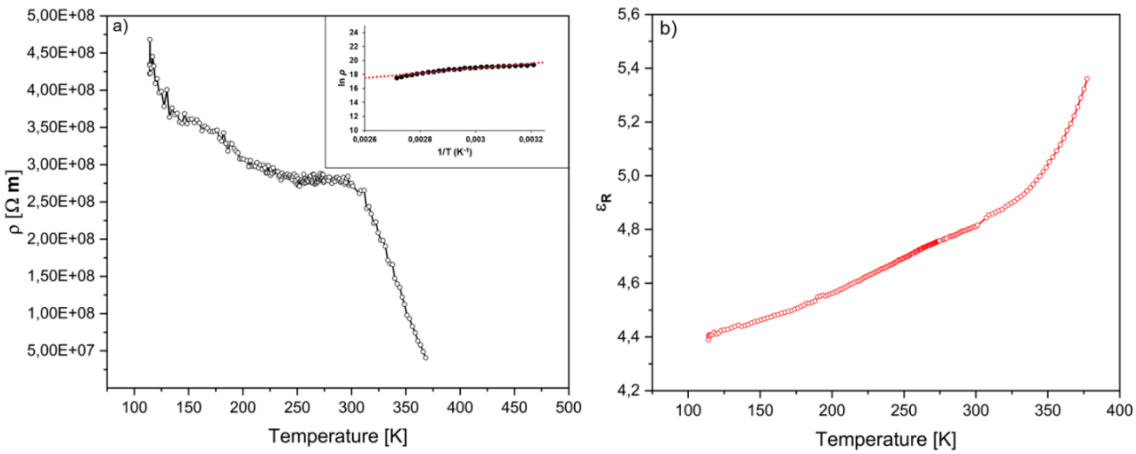

Figure 9 – Electrical resistivity (black curve) and dielectric constant (red curve) trend in the 110 – 380 K temperature range at 1 KHz frequency. Both measurements were performed on warming.

Ferroelectric characterization was carried out at room temperature, applying the PN measurement protocol, which has been previously used for the poling of ceramic ferrites with dielectric behavior [10]. Under repeated cycles of electric poling at this intensity, the system is gradually polarized until the complete depinning of the electric moment from the structure. The result is the definition of a current vs applied voltage loop characterized by two symmetric lobes followed by voltage-independent zero current, clearly pointing

out the presence of a depolarization process (Figure 10).

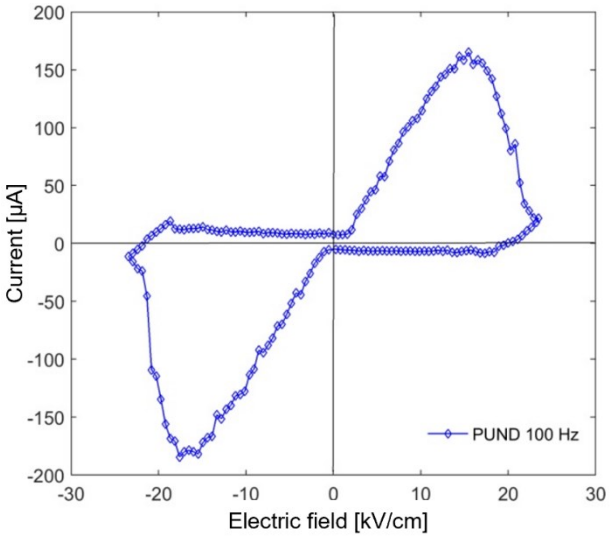

Figure 10 – Recorded current as a function of the applied electric field. The development of clear current lobes is a strong proof of the net change of the polarization.

This evidence indeed is not consistent with the presence of leakage currents, which would exhibit a constant increase with voltage. In the present case the current profile shows two maxima of reversed sign at intermediate applied voltage values, followed by a decrease as the voltage approaches the maximum applied value, as clearly shown also by the recorded currents developing during read voltage pulses (Figure 11b, c). This behavior is instead characteristic of a dielectric material, in which $I = dQ/dt = C\ dV/dt$ (C is the material capacitance). Within this framework, also the low dielectric losses observed near the maximum applied voltage (Figure 11a) caters for information about the capacitive nature of the material: in fact, the $tan\delta$ values, ranging from 0.035 to 0.06 at high electric field, are not very different from the behavior of an ideal dielectric ($tan\delta = 0$).

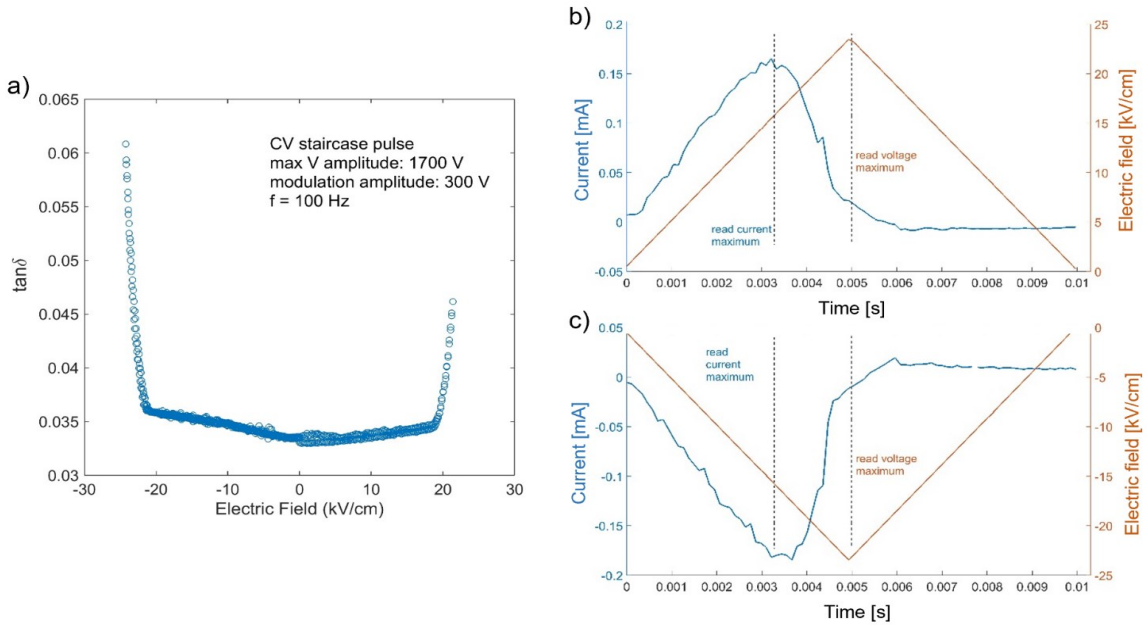

Figure 11 – a) tanδ plot as a function of electric field, showing the dielectric losses at ±20 kV/cm. b), c) Displacive currents collected on a ceramic BaFeO sample during the application of the positve and negative voltage pulses.

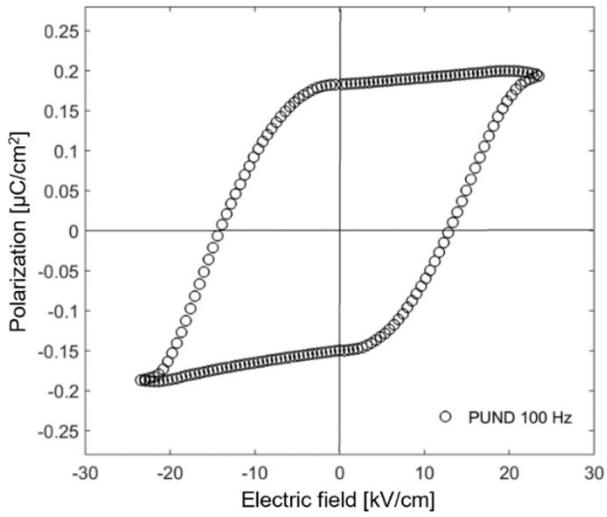

Figure 12 – PN hysteresis loop, which clearly confirms the ferroelectric beahaviour of BaFeO

So, it is possible to state that the electrical behavior of bulk γ-$BaFe_2O_4$ is primarily governed by its ferroelectric properties, despite the presence of minimal dielectric losses, as finally confirmed by the current-voltage data analysis. Indeed, the time integration of the current flow allows to obtain the electrical polarization as $\int_{0\ ms}^{10\ ms} IA\ dt$, reported in Figure 12 as a function of the applied electric field intensity. In this specific case, the

ferroelectric hysteresis loop exhibits a hard-like behavior with a coercive field of 12 kV/cm and a remnant polarization of 0.18 μC/cm^2, thus confirming the ferroelectric switching of the polarization.

The ferroelectric properties were further characterized by piezoresponse force microscopy (PFM) measurements performed on a sintered ceramic pellet. Figure 13 presents topography, lateral, and vertical PFM images of a sizable grain from the ceramic specimen. The ferroelectric domains with distinct polarization orientations are easily distinguished by means of their different amplitude and phase contrast, specifically displayed in the lateral PFM image. As can be seen, the domains arrange themselves in a regular pattern with straight boundaries, corresponding to non-180° (90° or 120°) domain walls; this texture without non-180° domains is typically observed in ferroelectric materials [11]. Particularly in ceramic materials, these domains form to minimize the mechanical energy associated with spontaneous strain at the ferro-to-paraelectric phase transition and to alleviate the mechanical stress arising at grain boundaries. In this case, three types of elastic domains separated by 120° domain walls exist, stemming from the disruption of the 6-fold rotation axis of the high-temperature *α*-polymorph, as observed in the SCXRD measurements. The coexistence of multiple polarization variants (domains) is a compelling indication of ferroelectricity in the studied material.

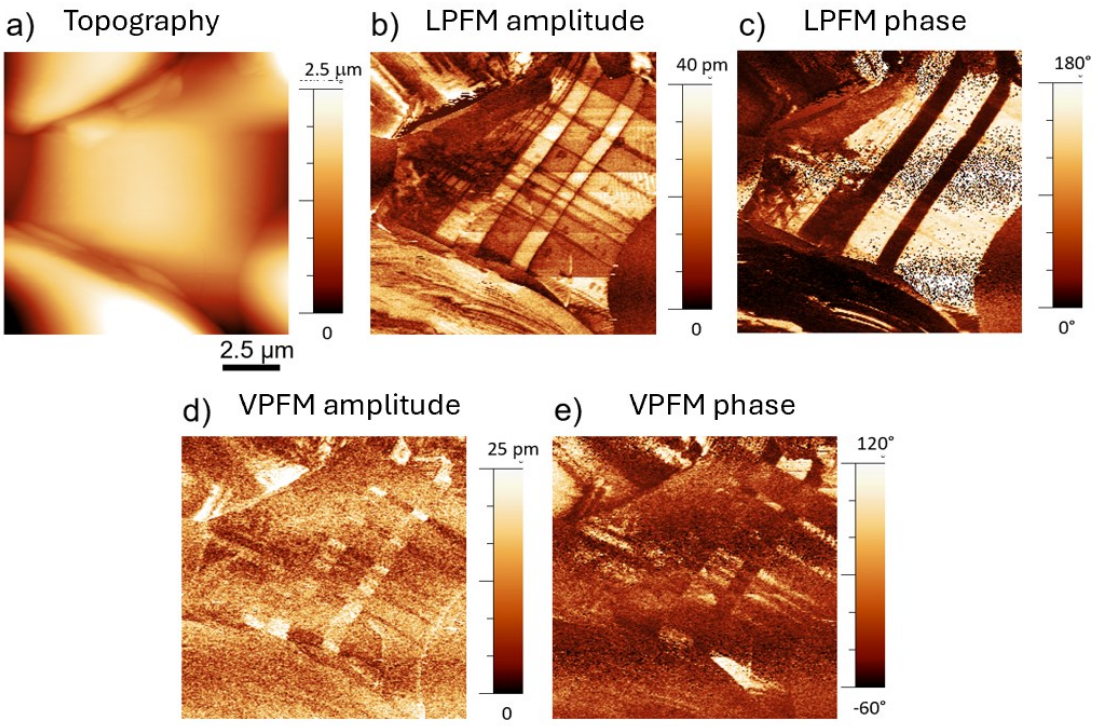

Figure 13 – Topography (a), lateral PFM (b, c), and vertical PFM (d, e) images. The amplitude (b, d) and the phase (c, e) PFM signals allow to visualize the ferroelectric domain walls and the orientations of polarization, respectively.

In Figure 14 an attempt to record the local piezoresponse hysteresis loops on the same analyzed area is shown, thus providing further evidence of the material's ferroelectric nature: the amplitude signal exhibits a characteristic butterfly shape, typical of ferroelectric materials, and the PFM signal undergoes a ~180° change, meaning that a switching of the direction of out-of-plane polarization has taken place. Note that the PFM signal is relatively small, in agreement with the small value of the remnant polarization detected by PN measurements. Conversely, the coercivity measured by PFM (~ 5 V) has a different physical interpretation compared to the bulk measurement: in the PN characterization, the coercive field represents the situation when the volumes occupied by domains with opposite polarities are equal, leading to zero total macroscopic polarization. On the other hand, the coercivity is determined when the piezoelectric response from a newly created domain beneath the PFM tip is equal to the response from an untouched volume. Furthermore, it is crucial to consider that macroscopic measurements involve the application of a homogeneous electric field to the specimen, while in a PFM experiment, the electric field generated by the tip (with a radius of 30 nm in our case) is strongly inhomogeneous, with a value far exceeding the applied voltage divided by the sample thickness.

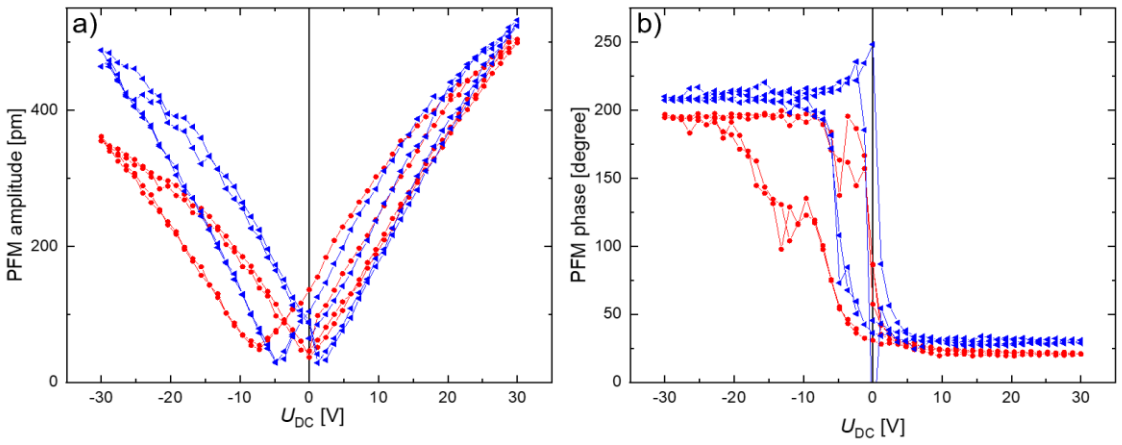

Figure 14 – Piezoresponse hysteresis loop of PFM amplitude (a) and phase (b), proving that the switching of polarization occurs. Two switching cycles (red and blue curves are the first and the second, respectively) are collected.

3.2.3 Magnetic characterization

Neutron powder diffraction (NPD) measurements carried out on γ-BaFeO polycrystalline sample allow the determination of the iron ions magnetic moments ordering. Data were collected on the WISH diffractometer (ISIS-UK) in the temperature range 300 – 1038 K and the obtained plot at average $2\theta = 152.7°$ shows the presence of two extra reflections occurring at T < 890 K, being incompatible with the C-centering of the nuclear space group and, thus, indicating a magnetic origin (Figure 15).

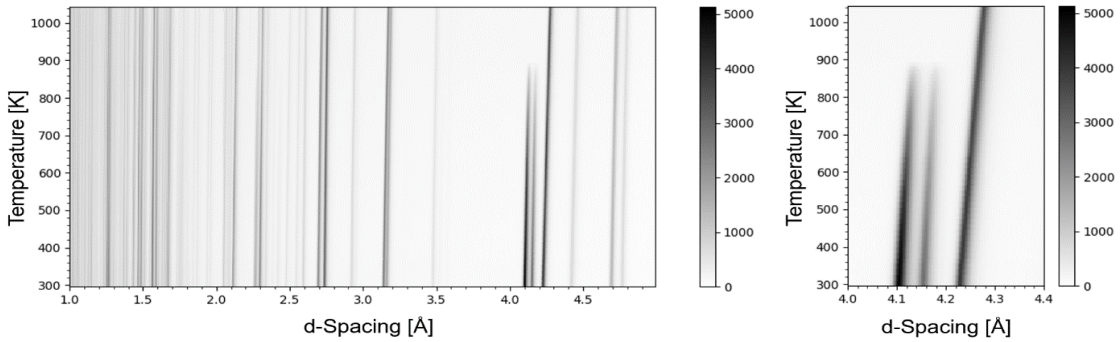

Figure 15 – Contour plot of the neutron data collected on the detector bank with average $2\theta = 152.7°$. Two extra reflections clearly arise below 890 K.

The high statistics data collected at 1038 K in the paramagnetic domain were refined by the Rietveld method, using the $Cmc2_1$ nuclear model derived from single-crystal diffraction data. The refinement yielded excellent agreement between the observed and

calculated data (R_p=3.07% and $_wR_p$=3.66%), allowing to further confirm the structural model determined by single-crystal X-ray diffraction with an average error of 0.5% for atomic coordinates. Moreover, as this technique allows to precisely refine the oxygen atom occupancies, by leveraging the high scattering length of the oxygen atoms compared to their X-ray scattering factor (relatively low compared to Ba and Fe), no significant deviation from the stoichiometric ratio was detected. Apart from temperature-induced modifications in the unit cell parameters and bond lengths, no other changes in the nuclear structure were observed within the explored temperature range. Figure 16 and Table II summarize Rietveld plots, structural parameters, and reliability factors.

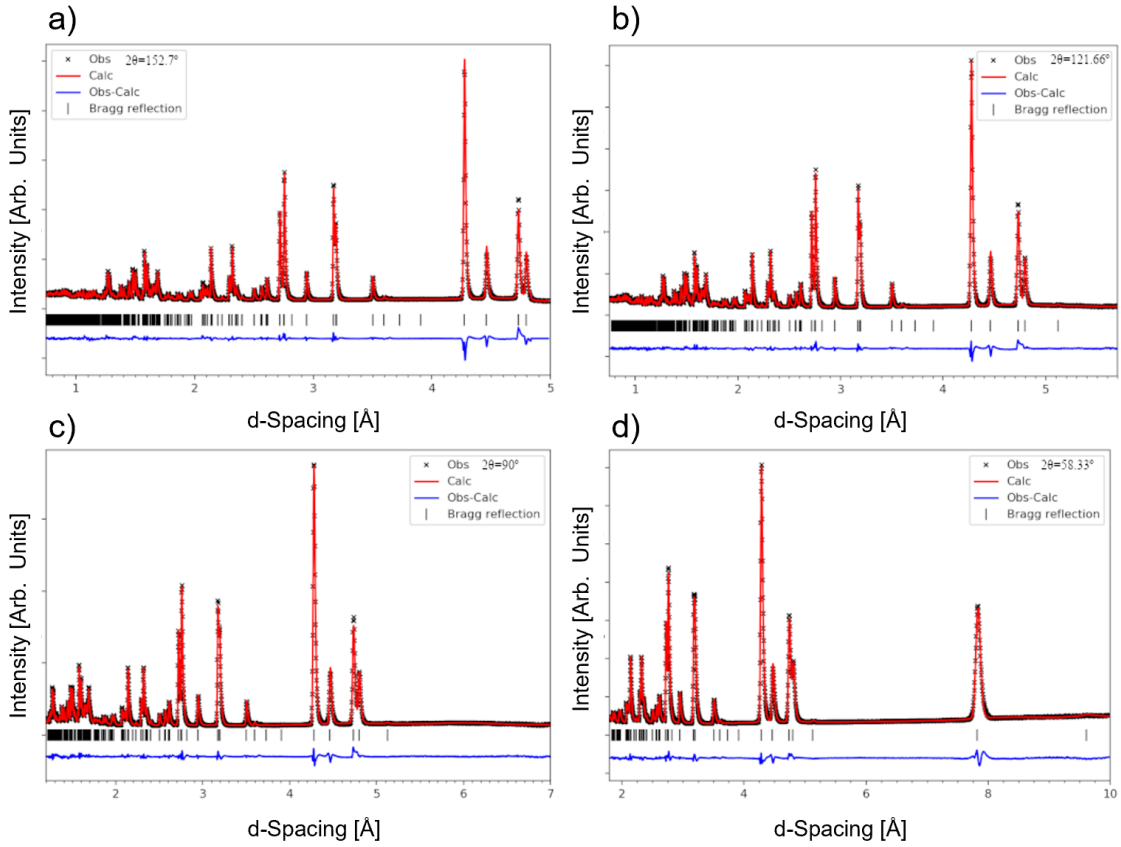

Figure 16 – Refinement of time-of-flight data by using Rietveld method. The patterns were collected on the detector banks with average 152.7 (a), 121.66 (b), 90 (c) and 58.33° (d) at 1038 K. Black crosses and red line represent observed and calculated data, while difference is reported as a blue line. The black tick marks indicate the position of the BaFeO reflections.

Table II – Crystal and structural parameters obtained from the refinement at 1038 K (see Figure 16)

$BaFe_2O_4$, 1038 K s.g. *Cmc2₁1'*(36) a = 8.55488(5) Å, b = 19.19690(13) Å, c = 5.43956(3) Å V = 893.324(10) Å^3 ρ= 4.655 g/cm^3 Z=8				
Rp		0.0307		
wRp		0.0366		
GooF		5.96		
Atom	x	y	z	U_{eq}
Ba1	0	0.1275(4)	0.0164(13)	0.0393(13)
Ba2	0.5	0.1194(3)	0.9998(14)	0.0244(12)
Fe1	0.2830(2)	0.04356(10)	0.4806(10)	0.0350(8)
Fe2	0.28988(18)	0.20976(9)	0.4846(10)	0.0163(5)
O1	0.5	0.04817(16)	0.4540(14)	0.070(2)
O2	0.2153(4)	0.1278(2)	0.6127(10)	0.0495(9)
O3	0.2106(4)	0.28917(19)	0.6454(12)	0.0635(11)
O4	0.5	0.21537(16)	0.5649(13)	0.0563(19)
O5	0.2229(3)	0.03683(17)	0.1492(11)	0.0192(8)

For what concerns the room-temperature data set (300 K), BaFeO turned out to be magnetically ordered with a propagation vector k = (1 0 0) and its magnetic structure was determined within the *P_Cca2₁* magnetic space group corresponding to the mY_4 irreducible representation and related to the parent *Cmc2₁* structure via the transformation {(0,1,0),(1,0,0),(0,0,-1)} with origin at (1/4, 1/4, 0). As a result, the magnetic structure exhibits a G-type ordering, with each Fe^{3+} moment antiferromagnetically coupled to its nearest neighbors. It is crucial to stress that this magnetic space group rules out the presence of any ferromagnetic component (Figure 17e). In Figure 17 and Table III Rietveld plots, structural parameters, and reliability factors are shown.

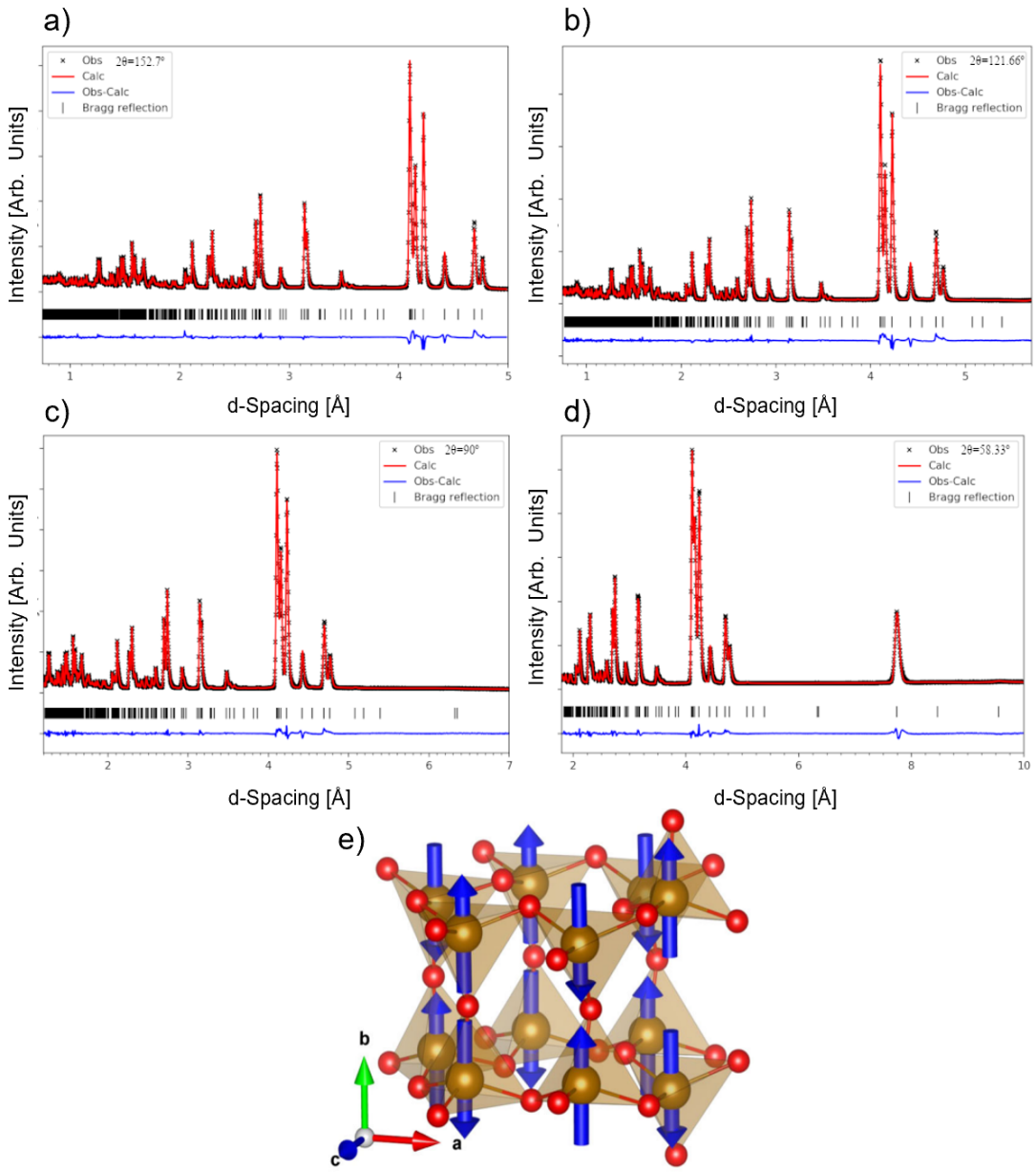

Figure 17 – a), b), c), d) Refinement of time-of-flight data by using Rietveld method. The patterns were collected on the detector banks with average 152.7 (a), 121.66 (b), 90 (c) and 58.33° (d) at 300 K. Black crosses and red lines represent observed and calculated data, while difference is reported as a blue line. The black tick marks indicate the position of the BaFeO reflections. e) Resulting orientation of the iron magnetic moments, which perfectly align with the b-axis, without any component along other axes, thus generating an antiferromagnetic order.

Table III – Crystal, structural parameters and refined moments obtained from the refinement at 300 K (see Figure 17)

$BaFe_2O_4$, 300 K s.g. P_Cca2_1 (36) a = 19.06414(12) Å, b = 8.45514(5) Å, c = 5.39014(3) Å V = 868.837(9) $Å^3$ ρ= 4.7862 g/cm^3 Z=8				
Rp		0.0325		
wRp		0.0411		
GooF		6.72		
Atom	x	y	z	U_{eq}
Ba1	0.3821(3)	0.25	0.000(3)	0.0158(9)
Ba2	0.8688(3)	0.25	0.024(3)	0.0129(9)
Fe1	0.79356(9)	0.02985(17)	0.528(2)	0.0193(6)
Fe2	-0.04074(9)	0.03894(15)	0.510(2)	0.0076(5)
O1	0.79853(13)	0.25	0.520(3)	0.0310(12)
O2	0.8770(2)	-0.0392(3)	0.382(2)	0.0247(7)
O3	0.04039(17)	-0.0399(3)	0.355(2)	0.0275(8)
O4	-0.03521(15)	0.25	0.416(3)	0.0316(12)
O5	0.78818(16)	-0.0275(2)	0.862(2)	0.0042(7)
Magnetic moments				
Atom	Mx	My	Mz	M_{tot}
Fe1	0	-3.740(4)μ_B	0	-3.740(4)μ_B
Fe2	0	3.740(4)μ_B	0	3.740(4)μ_B

The magnetic moments lie along the b-axis within experimental error, which is the a-axis of the parent $Cmc2_1$ structure, and the refined value at 300 K is 3.740(4) μB/Fe, whereas it tends to zero as temperature increases. Figure 18 shows the temperature evolution of the magnetic moment obtained from the Rietveld refinements. The fitting of the data with a critical law (red line) returns T_N = 890.5(3) K, thus indicating a high antiferro-to-paramagnetic transition point, and a β exponent of 0.285(2). The evolution of the lattice parameters is consistent with the temperature increase, apart from a very slight anomaly

at the Néel temperature, likely due to a magnetostrictive effect associated with the antiferromagnetic ordering.

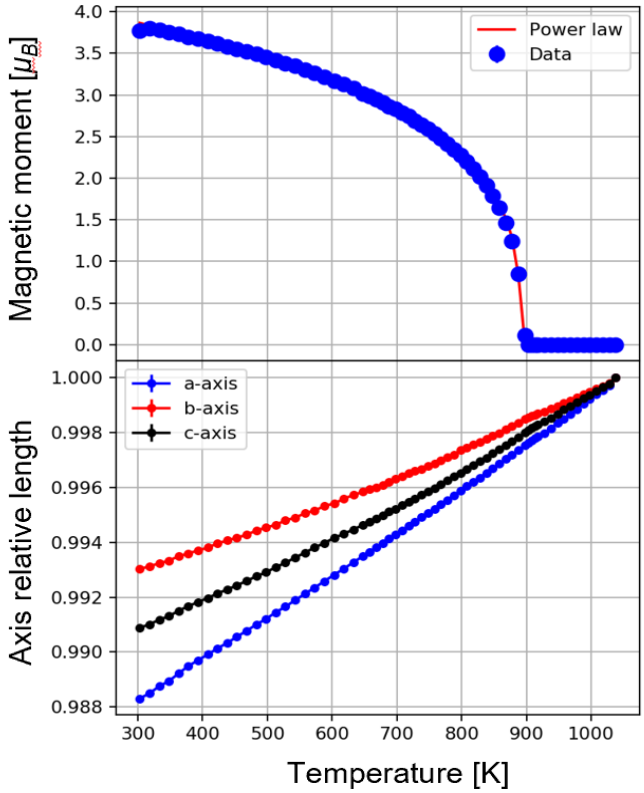

Figure 18 – Temperature evolution of the refined magnetic moment (top image) and of the lattice parameters.

The characterization of bulk magnetization was carried out on a BaFeO ceramic pellet by means of SQUID vibrating sample magnetometry (VSM) in the temperature range 300–1000 K. The zero-field cooling warming (ZFC) and field-cooled cooling (FCC) magnetization curves under a 2 T magnetic field show the paramagnetic transition at $T_{Néel}$ ≈ 890 K, in agreement with neutron diffraction data (Figure 19a). Both measurements reveal a residual magnetic moment at low temperature, seemingly contradictory to the antiferromagnetic (AFM) nature established by neutron diffraction. Anyway, the ZFC results might be explained by a certain canting of the magnetic moments, typically arising from partial non-collinearity of the AFM order. In this context, considering that NPD should be regarded as a phase-selective method, in contrast to magnetometry measurements that, while offering higher sensitivity, inevitably generate bulk-averaged data, this effect is more likely ascribed to the presence of undetected impurities. To confirm this assumption, detailed VSM studies at various temperatures (300, 800 and 1000 K) depict magnetization vs. magnetic field (Figure 19b). Note that field linear

behavior at high magnetic fields is compatible with the overall AFM nature. Nonetheless, the room temperature measurement displays a low-field weak hysteresis, which is likely correlated to other undetectable iron-containing phases, predominantly hexaferrite ($BaFe_{12}O_{19}$; $T_{Néel} \approx 720$ K) [12] and $BaFe_4O_7$ ($T_{Néel} = 850$ K) [13], as supported by the negligible residual magnetization values. Assuming the full residual magnetization of 0.0048 emu/g in the 300 K loops to be due to hexaferrite ($M_r = 32$ emu/g [14]) yields a weight fraction of 0.15%, below the diffraction detection limit. Similarly, interpreting the 800 K loop contribution as $BaFe_4O_7$ would result in a weight fraction of 0.16%, again below both X-ray and neutron diffraction sensitivity. A further confirmation is given by the collection of a hysteresis loop related to a two-phase BaFeO sample with hexaferrite (~ 30% wt). In this case, the saturation magnetization (1.5 μB/f.u.) is too high to be simply justified as weak ferromagnetic component emerging from the collinear AFM order of BaFeO (as an example, in $BiFeO_3$ single crystals the calculated magnitude of the canting of the magnetic moments results in a weak ferromagnetism of ~ 0.05 μB per unit cell [14]); otherwise, it is possibly ascribed to a spurious contribution arising from hexaferrite crystallites dispersed within the BaFeO matrix. Therefore, the shown larger loop is the consequence of a clear sample-dependent ferromagnetic behaviour (Figure 19c).

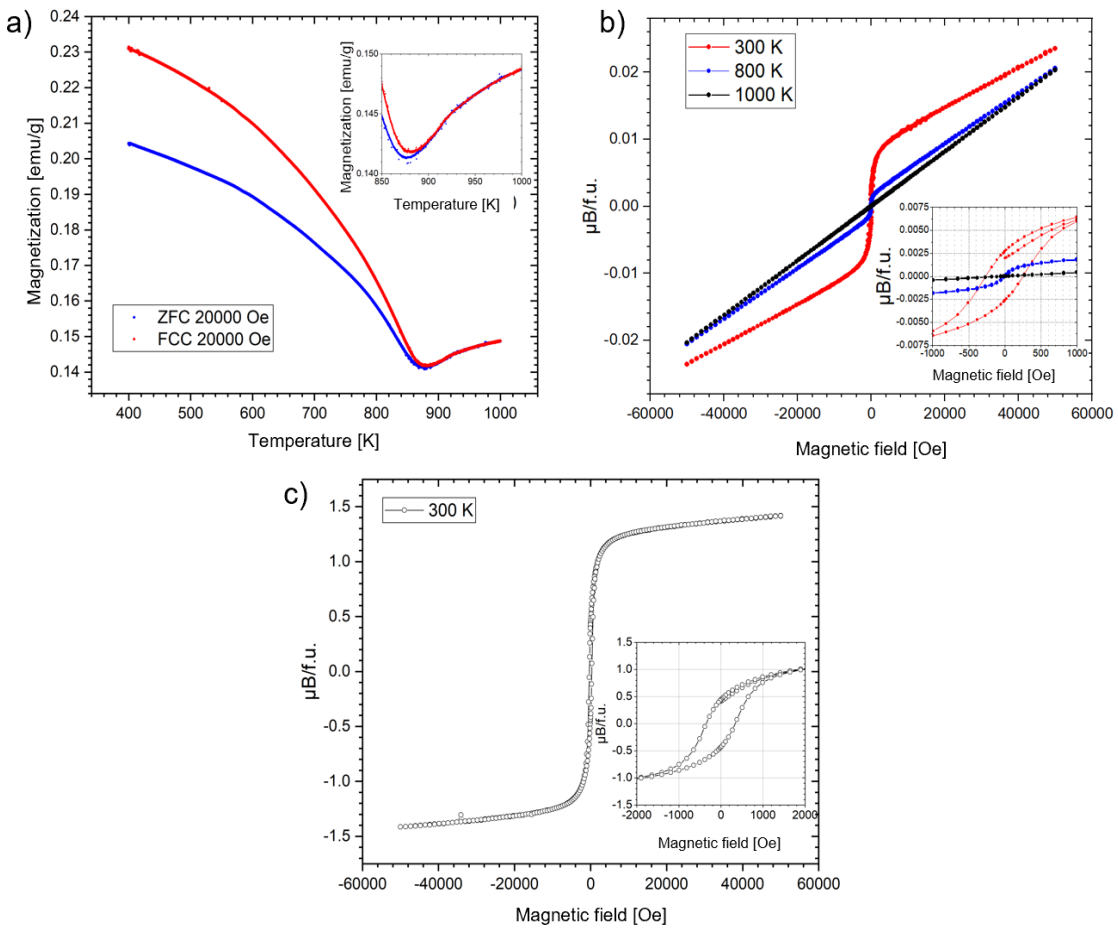

Figure 19 – a) ZFC (blue) and FCC (red) magnetization measurements as a function of temperature, exhibiting a net anomaly at ~ 890 K. The inset shows a descending branch of the AFM cusp, confirming the antiparallel ordered magnetic state of BaFeO, as pointed out by NPD. b) Magnetization versus field hysteresis loops collected at 300 K, 800 K, and 1000 K. The inset exhibits the sensible reduction of the low-field hysteresis loop above 750 K, likely due to the paramagnetic transition of hexaferrite byproduct. The residual ferromagnetic component at 800 K is ascribable to other impurities, such as $BaFe_4O_7$. c) Hysteresis loop collected at 300 K on a hexaferrite-enriched BaFeO sample, showing the increase of soft ferromagnetic component.

3.3 References

[1] B. H. Toby and R. B. Von Dreele *"What's new in GSAS-II"* Powder Diffraction (2014), 29, S2-S6

[2] Bruker, APEX2, SAINT, TWINABS Bruker AXS Inc., Madison (2014)

[3] G. M. Sheldrick *"Crystal structure refinement with SHELXL"* Acta Cryst (2015), A 71, 3–8

[4] G. M. Sheldrick *"A short history of SHELX"* Acta Cryst. (2008), A 64, 112–122

[5] L. C. Chapon, P. Manuel, P. G. Radaelli, C. Benson, L. Perrott, S. Ansell, N. J. Rhodes, D. Raspino, D. Duxbury, E. Spill and J. Norris *"Wish: The New Powder and Single Crystal Magnetic Diffractometer on the Second Target Station"* Neutron News (2011), 22:2, 22-25V.

[6] V. Petricek, M. Dusek and L. Palatinus *"Crystallographic computing system JANA2006: general features"* Z. Kristallogr. - Cryst. Mater. (2014), 229, 345–352

[7] B. J. Campbell, H. T. Stokes, D. E. Tanner and D. M. Hatch *"ISODISPLACE: a web-based tool for exploring structural distortions"* J. Appl. Crystallogr. (2006) 39, 607–614

[8] V. Shvartsman and A. L. Kholkin *"Nanoscale investigation of polycrystalline ferroelectric materials via piezoresponse force microscopy. Multifunctional Polycrystalline Ferroelectric Materials: Processing and Properties"* (eds L. Pardo and J. Ricote) Springer, Dordrecht (2011)

[9] D. A. Vinnik, E. A. Trofimov and D. A. Zherebtsov *"Experimental Study and Thermodynamic Modeling of Phase Equilibria in BaO-Fe_2O_3 System"* Materials Science Forum (2016), 843, 16–21

[10] D. Delmonte, F. Mezzadri, E. Gilioli, M. Solzi, G. Calestani, F. Bolzoni, R. Cabassi *"Poling-written ferroelectricity in bulk multiferroic double-perovskite $BiFe_{0.5}Mn_{0.5}O_3$"* Inorg. Chem. (2016), 55, 6308–6314

[11] G. Arlt *"Twinning in ferroelectric and ferroelastic ceramics: stress relief"* J. Mater. Sci. (1990), 25, 2655

[12] G. Tan and X. Chen *"Structure and multiferroic properties of barium hexaferrite*

ceramics" J. Magn. Magn. Mat. (2013), 327, 87–90

[13] T. Ferreira, G. Morrison, M. W. Chance, S. A. Calder, D. M. Smith and H. C. Loye *"$BaFe_4O_7$ and $K_{0.22}Ba_{0.89}Fe_4O_7$: canted antiferromagnetic diferrites with exceptionally high magnetic ordering temperatures"* Chem. Mater. (2017), 29, 2689–2693

[14] C. Ederer and N. A. Spaldin "Weak ferromagnetism and magnetoelectric coupling in bismuth ferrite" Phys. Rev. (2005), B 71, 060401

4 Growth of γ-BaFe2O4 thin films by Pulsed Electron Deposition technique

4.1 Physical vapour deposition-based techniques

Physical vapor deposition (PVD) techniques group different vacuum deposition methods to produce thin films and coatings on substrates. In PVD, the material is transformed from a condensed state to a vapor state and then back to the condensed state. This process is achieved by performing a direct thermal treatment on the material or by using a high-power laser/electron/ions beam, which is able to remove atoms, ions, or molecules from a solid source material and to deposit them on a solid substrate. This definition includes a large number of techniques, such as sputtering and thermal evaporation-based methods, whose advancement has enabled to achieve a high-sensitivity in the control of thin film thickness, composition and structure, thus proving to be able to satisfy many demands coming from different industrial areas. In fact, the deposition of coating layers allows to improve the mechanical properties and durability of materials. As an example, the application of high-power impulse magnetron sputtering technique, which exploits a high density plasma, generated by a glow discharge [1], allows to produce high-quality TiMg(RE)N (RE = Rare Earth) based coatings showing improved wear resistance against abrasion, hardness and toughness whit a low friction coefficient, which make this coating a proper method to protect mild steel substrates [2]. PVD coatings turned out to be useful also in biomedical applications, to improve mechanical properties and biocompatibility of implants [3], and in automotive and aerospace fields, thanks to their contribution in terms of increased tool life, reduced machining costs, and improved part quality [4, 5, 6, 7].

Beside the simple coating, the optimization of PVD techniques in crystal growth has also allowed to perform thin films growth for the functionalization of multilayer devices. Within framework, deposition techniques based on addressing a pulsed high-energy beam towards a target material turned out to be particularly promising. Especially, pulsed laser deposition (PLD), a PVD technology based on the ablation of the target upon a high-energy laser irradiation, has been widely used both in academic research and large-scale

industry, because of its huge versatility and the capability to perform deposition processes with a high control of the stoichiometry and thin film microstructure, and, to date, several thin film devices made of different materials such as nitrides, carbides, complex oxides and metalorganic composites have been successfully produced by using this technique [8, 9, 10, 11]. Also, PLD is particularly suitable for the deposition of those materials with properties affected by their long-range order, as it enables a precise control over crystallinity, orientation and strain of domains, which is crucial for the modulation of ferroelectric and magnetic properties. Even multiferroic $BiFeO_3$ owes its wide range of applications to PLD: in particular, it was demonstrated that heteroepitaxial constraints can dramatically enhance the ferroelectric properties of $BiFeO_3$ thin films deposited on $SrTiO_3$(100), thus producing a larger spontaneous polarization (50-60 μC/cm^2) than that measured in bulk samples (~ 6.1 μC/cm^2) [12].

4.1.1 Pulsed electron deposition: principles and applications

This thesis explores the use of pulsed electron deposition (PED), a physical vapor deposition technique similar to PLD but employing a pulsed electron beam instead of a laser. PED offers the ability to grow high-quality thin films from a single target across a wide range of substrate temperatures. This process involves vaporizing a ceramic target using pulsed electron beams with a high-power density, up to 10^8 W/cm^2, which is much higher than the power density required for thermodynamic evaporation (around 10^6 W/cm^2). The electron impingement causes the target surface to heat up rapidly, transforming it directly into plasma without the occurrence of a phase transition. This process allows the target stoichiometry to be preserved in the plasma and in the following thin film. Additionally, the high temperatures (thousands of Kelvins) in the plasma increase the mobility of deposited atoms on the substrate. This allows for the growth of thin films at lower deposition temperatures than would be required for bulk synthesis.

At this point, a key difference between PLD and PED due to the beam nature emerges: since in PLD the ablation process is driven by the laser beam absorption, its propagation within the target is ruled by Lambert-Beer's law ($I(x) = I(x_0)\exp[-\alpha(x-x_0)]$) and, especially, by the absorption coefficient α of the material at a precise wavelength. This mechanism can be a limiting factor if the target material is a wide bandgap dielectric (such as SiO_2, MgO, Al_2O_3, etc.), because of its transparency to the laser wavelength [13].

Conversely, thanks to its ablation process, PED does not present such limitations. All these characteristics make PED an ideal PVD method for depositing a wide range of materials with different chemical and physical properties and even complex phase diagrams, starting simply from the bulk material with the desired stoichiometry. Numerous examples of materials successfully deposited using PED are reported in the literature, including zinc oxide-based semiconductors, oxides, hydroxyapatite, FeS_2, high-temperature superconductors like $YBa_2Cu_3O_{7-x}$, and many others. In fact, the number of PED publications in the last three years already exceeds 60% of those published in the previous decade (Figure 1) [14, 15, 16, 17, 18].

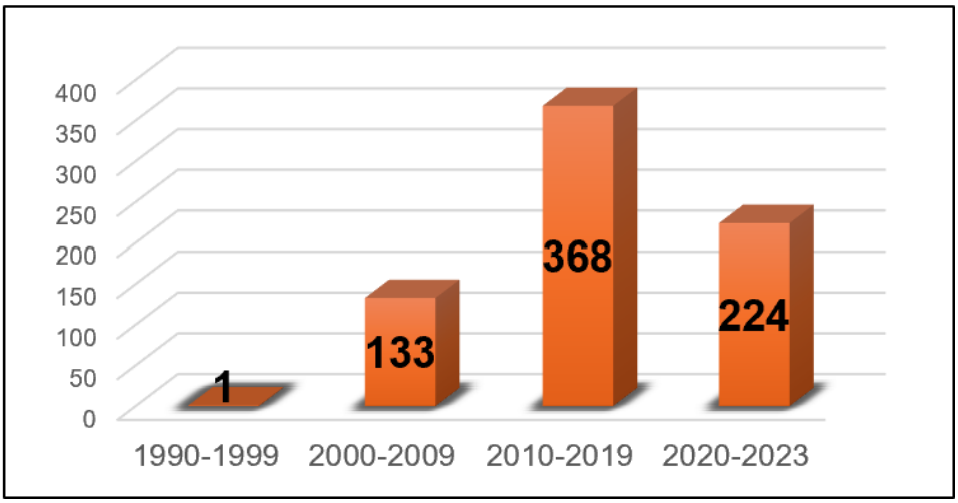

Figure 1 – PED-related publications. The data were taken from Google Scholar.

PED instrumentation utilizes a hollow cathode made of a metal tube with a narrow outlet facing a flat anode. Electron pulses are generated within the cathode, assisted by a background gas that promotes ionization and electron production. The plasma discharge is initiated by a specialized circuit operating at adjustable frequencies. Electrons are pushed forward by applying high voltages, and the resulting currents are guided through an insulating alumina tube positioned at the cathode's core towards the target, which functions as the anode. Typically, the tube is tilted at a 45-degree angle in relation to the target surface, and the substrate is set above it. Overall, the discharge process takes 100 nanoseconds.

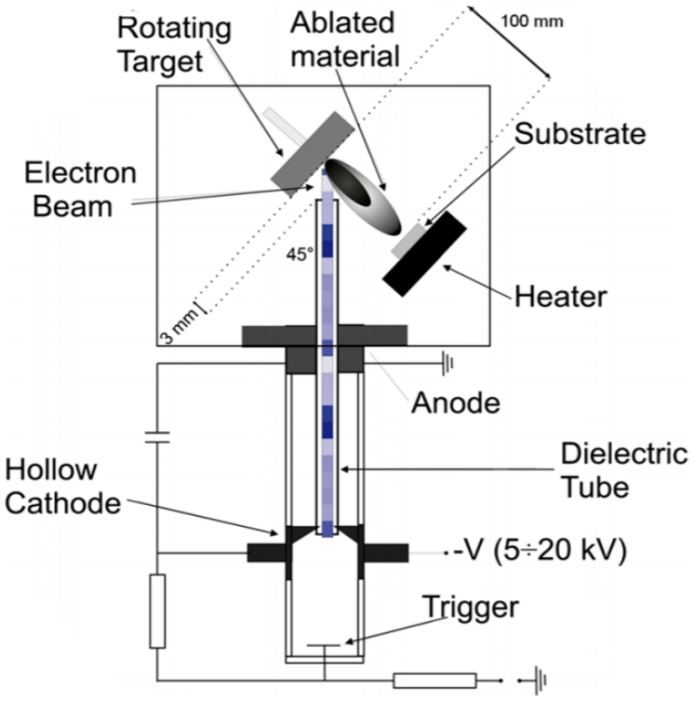

Figure 2 – Schematic representation of a PED source [19].

A direct consequence of the discharge development is the poly-energetic nature of the electron beam, as opposed to the monochromatic beam generated in PLD. As a result, different energy means different velocity, so the electron energy and beam power are functions of time. The beam can be divided into 3 contributions as a function of the electron energy:

I. the head of the beam, containing the most energetic electrons but very few and reaching deep layers of the target;
II. a series of electrons with intermediate energy and still low current;
III. a final tail of electrons with the highest current but the lowest energy.

The composition of the electron beam significantly impacts the formation of the material plasma. To achieve efficient ablation, high-energy electrons must exceed a certain threshold value, which varies depending on the target material (typically around 10^7 W/cm^2). In PED, two main ablation mechanisms coexist: electronic ablation, the most prevalent one, arises from the interaction between the electron beam and the electron

shells of target atoms. This interaction ionizes and excites the atoms, creating electron-hole pairs in the lattice, and is responsible for the rapid expansion of the plasma plume. The second mechanism, macroscopic ablation, is the major drawback in PLD and PED processes. It originates from the high-energy electrons and involves the "hydrodynamic ablation", which results in the plasma formation in subsurface layers of the target, causing its expansion and the ejection of solid debris (even with dimensions of tens of micrometers) or liquid particulate towards the substrate. This side effect can be mitigated by modulating the voltage applied to the electron beam, but this comes at the expense of increasing the proportion of low-energy electrons (from the tail of the beam), which can lead to stoichiometry issues for materials with incongruent melting points. Therefore, thin film deposition in PED is a result of the combined action of high-energy ablation and thermal evaporation, resulting in a thickness distribution similar to that observed in PLD [20].

The present chapter is focused on the optimization of the PED parameters, including e-beam power, temperature and substrate type, to understand and enhance plasma plume formation and BaFeO stoichiometric transfer to the substrate. The effects of the e-beam-on-target interaction on the composition of the obtained thin film was analyzed by applying different fluid-dynamic models, considering both ablation and evaporation.

4.2 Methods

4.2.1 Thin films synthesis

BaFeO films were grown in a high vacuum chamber equipped with a PEBS-20 commercial source, supplied by Neocera Inc., MD, USA (Figure 3), which ensures the cathode cooling by limiting the pulse repetition rate as a function of the accelerating voltage, thus reducing the overall operating power. Indeed, the energy distribution of the electron beam also depends on the cathode's temperature, as its overheating may result in the emission of electrons, by thermo-ionic effect, having generally low energy, thus extending the discharge tail and resulting in an increased incongruent evaporation. In this specific setup, the maximum operating power of the gun is set at 15W, so that the pulse repetition rate is maximum (10Hz) for voltages up to 14kV, and then decreases down to 5 Hz at 20 kV. The chamber was pumped down to a base pressure of approximately

2.0×10^{-4} Pa. The pulsed electron beam was ignited at a 16 kV discharge voltage. The pulse repetition rate is 6 Hz. During deposition, O_2 gas (5 N purity) is introduced at a pressure of approximately 1.0×10^{-2} Pa to ignite the electron beam and stabilize beam propagation towards the target. Further details on the synthesis process are provided in the following section. The starting target material consists of 5 mm-thick cylindrical pellets of BaFeO, produced through solid-state reaction (1300°C x 12h in air). The films were deposited on various substrates: i) 7.5 × 2.5 cm^2-wide quartz, ii) 1x1 cm^2 SiO_2/Si, iii) 1x1 cm^2 Pt-coated quartz wafer, and iv) 1x1 cm^2 polished MgO single crystal. Prior to the PED process, the substrates underwent a procedural rinse in acetone/ethanol/isopropanol. The distance between the target and substrate ranged from 5 to 7 cm. The substrate temperature was monitored using a type-K thermocouple and a 2.4 μm IR pyrometer (Fluke Endurance 3M). The devices were positioned behind a ZnSe-bandpass viewport at 45° to the sample surface. The substrate temperature varied between 700 °C and 800 °C, while the number of pulsed discharges is in the 3-10 $x10^4$ range. At the end of each BaFeO deposition, a 20-minute-long annealing treatment at 670°C in an oxygen-enriched environment (5 x 10^{-1} Pa) was carried out.

Figure 3 – Deposition chamber installed at IMEM – CNR (Parma).

4.2.2 X-ray diffraction techniques and Raman spectroscopy

The structural characteristics of the films, such as their crystal quality and preferred grain orientation, were analyzed by X-ray powder diffraction technique (XRPD) using a Rigaku Smartlab XE diffractometer equipped with a HyPix3000 detector. Cu-K_α wavelength was used with a Ni filter placed on the diffracted beam to eliminate the K_β component. For Bragg-Brentano measurements both the incident and diffracted optical paths were equipped with 5.0° soller slits and a 5 mm length limiting slit was applied to fit the size of the films. The detector operation mode was set to 1D. Pole figures were obtained using a Euler cradle, equipped with a Schultz slit to reduce the defocusing effects at high χ. The incident beam was parallelized by a parabolic mirror and shaped using 5.0° Soller slits and 0.2 mm vertical slits. The detector was operated in 0D mode. Pole figures were acquired through 360° ϕ scans at fixed χ values (5° intervals), ranging from 0° to the experimental limit of 75°. The background signal was measured and subtracted for each measurement. Proper homemade Matlab code was used for data plotting and analysis. Raman spectroscopic analyses were conducted using a Horiba LabRam HR Evolution micro-Raman spectrometer coupled with a confocal Olympus microscope. The system

employed 10x, 50x, ULWD50x, and 100x objectives, achieving spatial resolutions of ~1 μm. The micro-Raman setup was equipped with a He-Ne laser emitting at 632.8 nm, BraggRate notch filters, silicon CCD + InGaAs diode array detectors, 300-600-1800 lines/mm gratings, and density filters. Prior to each measurement, the spectrometer was calibrated using the standard silicon Raman peak at 520.6 cm^{-1}. The spectra presented here were obtained using the 100x objective, with an acquisition time of 60 seconds and ten repetitions and employing a 50% density filter.

4.2.3 Scanning electron microscopy and energy dispersive X-ray spectrometry

The samples were analyzed for morphology and thickness using a scanning electron microscope (FEG-SEM, Zeiss Auriga Compact) operating at 25 kV. Compositional analysis was performed on BaFeO targets and films using an Energy Dispersive X-Ray spectrometer (EDX).

The optical properties were determined using a JASCO V-770 spectrophotometer equipped with an integrating sphere. The spectrophotometer operated in both diffuse reflectance and transmission modes in the wavelength range of 400-2000 nm.

4.3 Results and Discussion

4.3.1 BaFeO target synthesis

One of the most important aspects to control in the PED technique is the quality of the starting target [21]. The target requirements are as follows: i) purity, ii) a nominal stoichiometry equal to that desired on the film iii) compactness and resistance to erosion. To meet the specified requirements, the BaFeO targets were produced in several stages. The first one involved the solid-state reaction of the precursors and sintering of the pellets (Figure 4). Initially, equimolar quantities of $BaCO_3$ and Fe_2O_3 were mixed and milled to guarantee optimal contact between the reactants. The solid mixture was heated at 1300°C for 12 hours in air. Subsequently, an acid aqueous solution, (HNO_3 0.1M) was used to rinse the resulting reaction product to eliminate $BaCO_3$ residuals. In particular, segregation of $BaCO_3$ at the surface of the BaFeO crystallites as the result of reaction with air CO_2, could potentially limit the sintering process needed to achieve the proper ceramic quality. BaFeO powders were then cold-pressed at 200 bar in a 1"-diameter press mould, and the sintering was performed in a furnace at 1000°C for 24 hours in air.

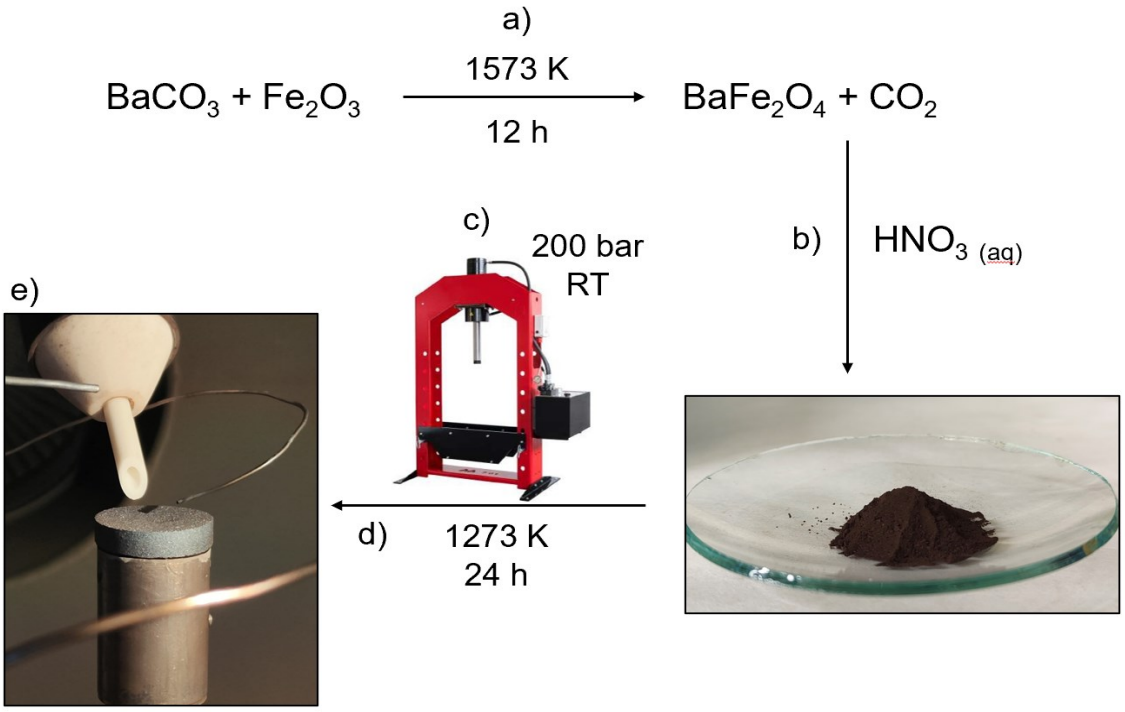

Figure 4 - Summary of all steps to synthesize the BaFeO target for PED: a) solid-state reaction to obtain the BaFeO powder; b) elimination of $BaCO_3$ residuals through acidic washing; c) cold pressing of BaFeO powders at 200 bar in in a 1-inch diameter pellet d) sintering of BaFeO pellet in furnace; e) mounting of the target in the PED system.

The XRD patterns of the as-synthesized BaFeO powders and of the sintered target are reported in Figure 5. In the latter case the measurement was made on a scratched sample taken from the pellet surface. It is clear from the results that both the processes did not result in any impurities or formation of $BaFe_2O_4$-related polymorphic phases.

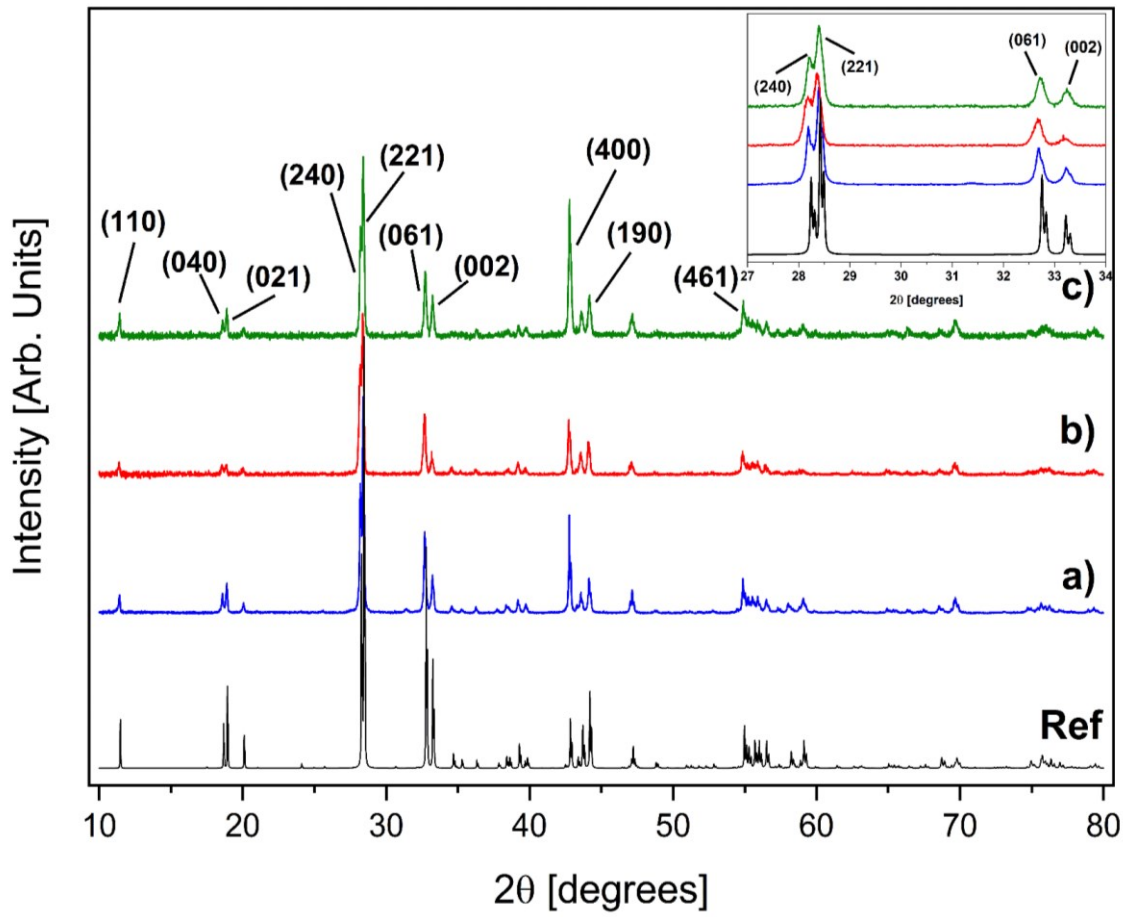

Figure 5 – X-ray powder diffraction patterns collected after each synthesis step: a) as-grown BaFeO powders; b) sintered BaFeO target; c) BaFeO pellet surface after first film deposition. The reference pattern (black) is calculated from the single-crystal dataset described in Chapter 3. The main hkl reflections are indexed as well. In the inset a close-up of the XRD reflections at low diffraction angles.

Additionally, Raman measurements conducted at various points on the powder, before and after the sintering process, did not reveal the presence of any byproducts (see Figure 6). In particular, the most prominent peaks at 211 cm^{-1}, 372 cm^{-1} and 611 cm^{-1} are uniquely attributable to the γ-$BaFe_2O_4$ phase [22]. No characteristic intensities related to β'-phase were detected.

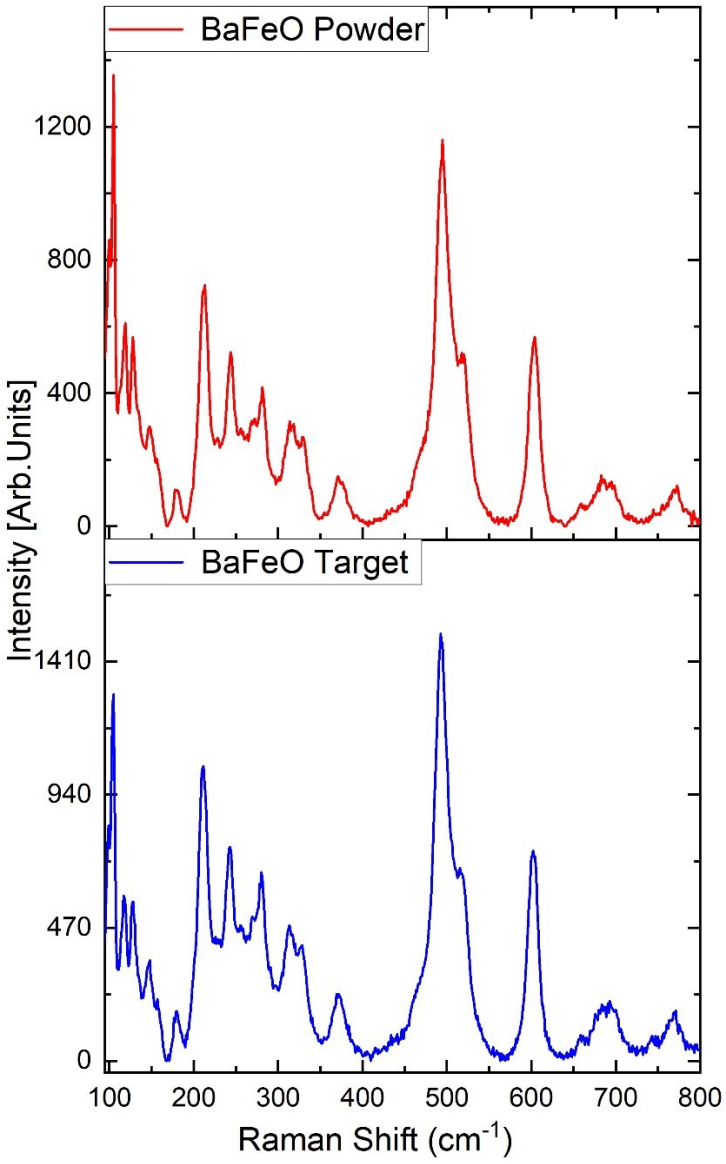

Figure 6 – Raman spectra of the BaFeO powder before (up) and after (bottom) the sintering process in the furnace.

To verify the chemical stability of the target during PED ablation, a PXRD analysis was conducted on a sample of the pellet obtained by scratching its surface, after a short deposition process. The BaFeO PXRD pattern in Figure 5c remained unchanged compared to the starting powder, indicating good chemical and mechanical stability of the material also under the high energy conditions produced by the PED electron beam.

4.3.2 Analysis of plasma plume

To assess the effects of the plasma plume profile on thickness, structure and chemical composition of the BaFeO films, preliminary PED depositions were carried out on a large quartz substrate (7 x 2.5 cm^2). The choice of the substrate mainly depends on the possibility of performing a deposition without imposing any epitaxial constraint. The quartz has been then divided into six equally spaced sections with an area of 1.0 x 2.5 cm^2. As represented in Figure 7, Sections #1 and #6 are the farthest points from the plume center, while #3, #4 and #5 are the regions where the central part of the plume has impinged on.

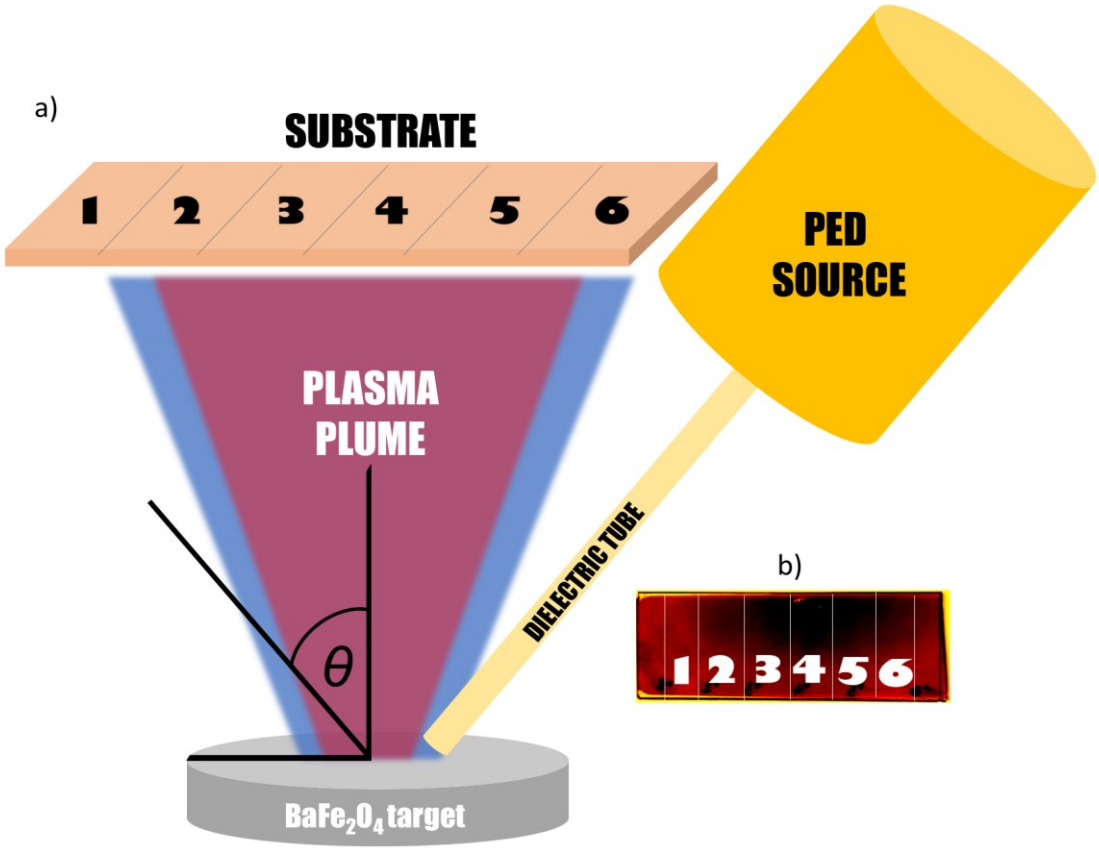

Figure 7 – a) Schematic representation of the PED process and respective positions of source, target, and substrate. b) Saturated image of the real quartz substrate after the BaFeO deposition with the respective section numbers. The black region indicates a larger thickness of BaFeO.

Table I lists the growth parameters used to study the plume distribution.

Table I – Operating parameters of BaFeO deposition by PED.

e-beam Voltage	16 kV
Repetition rate	6 Hz
Target-to-substrate distance	7 cm
Working chamber pressure	0.15 Pa
Substrate temperature	800°C
Total pulses	$1x10^5$

The number of total pulses was chosen in order to achieve films with a maximum thickness on section #4, t (0) = 3000 nm.

I. Thickness analysis

The assessment of the thickness profile, i.e., how the plasma plume is distributed along the substrate, has been performed by capturing SEM cross-section images at different values of the inclination angle θ, formed between the target normal and the line connecting the target to the measured point on the substrate (Figure 8). The SEM cross-sectional images were taken along the major axis of the substrate, starting from the center of the plume, corresponding to the minimum target-substrate distance with $\theta = 0°$, toward the furthest region located at angle $\theta = 30°$ from the center. The film thickness profile was measured by probing 10 points on each substrate section, for a total of 60 measured points (Figure 8). The values of t(θ), normalized with respect to respect to the maximum thickness, t(0) = 3000 nm, are plotted in Figure 9.

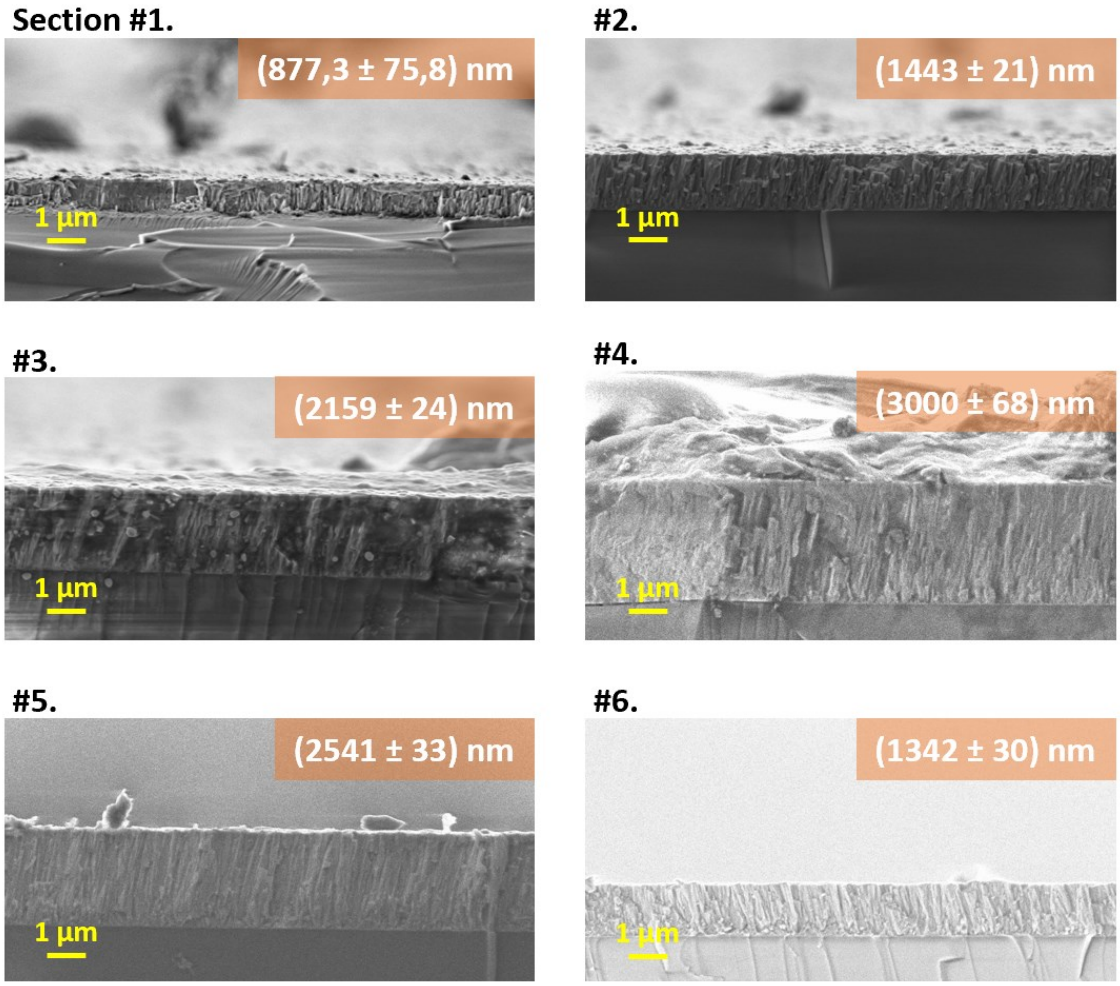

Figure 8 – Cross-sectional SEM images of BaFeO films on quartz taken at different sections of the large 7.5 x 2.5 cm^2 substrate (from Section #1 to #6).

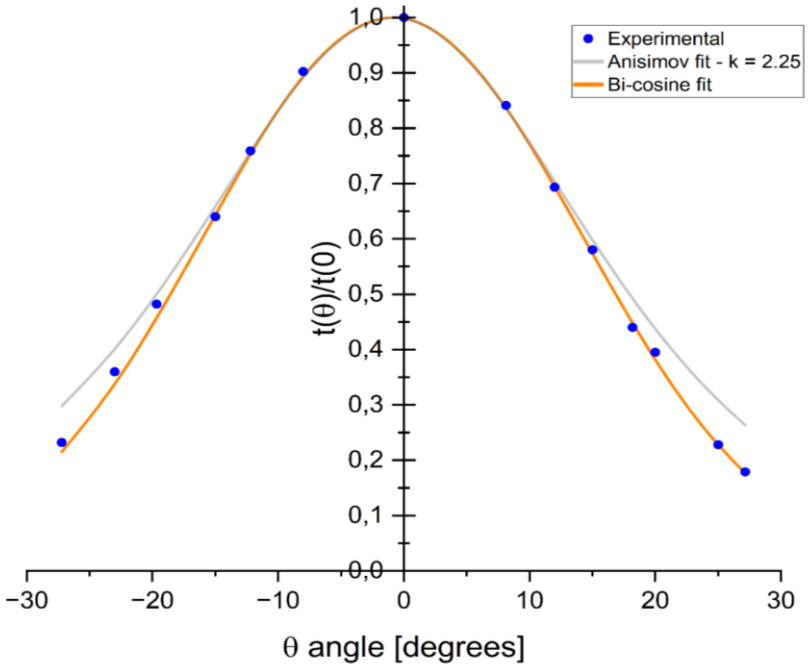

Figure 9 - Thickness profiles of the BaFeO film as a function of the inclination angle θ. The blue dots represent the experimental data, while solid lines line represent the best fits according to the Anisimov model (grey curve) and the bicosine model (orange curve).

The data were initially fitted with the theoretical profile described in the Anisimov's model [23], which considers the plume formation in high-energy deposition techniques as an adiabatic plasma expansion occurring at supersonic velocity from a single point on the target. The ratio between the film thickness measured at an angle θ and that measured at θ=0 is given by the following equation:

$$t(\theta)/t(0) = (1 + k^2\theta)^{-\frac{3}{2}} \quad (1),$$

where k is a variable parameter related to the adiabatic expansion velocity of the plume. The higher the value of k, the higher the expansion velocity. The best fit of the experimental curve is obtained when k = 2.25, with a R^2 value = 0.998. However, as it appears in Figure 5, Anisimov's model does not perfectly fit the experimental thickness profile for larger θ values. Another non-Maxwellian angular distribution model is usually used for fitting the film thickness produced by PED or PLD, even at larger angles. According to this model, in high energy ablation processes the velocity of ablated species

is usually described by a bi-component distribution, due to different plume formation mechanisms on the target. The first component is due to the adiabatic expansion from the target, as in Anisimov's model. It is characterized by a sharp velocity distribution, which implies a great stream velocity. A second broader component, not considered in the Anisimov's model, is due to a slow isotropic velocity distribution, typically with zero stream velocity. Hence the angular distribution can be described by the linear combination of two cosine functions [24,25]:

$$F(\theta) = t(\theta)/t(0) \; = \; a\cos\theta \; + \; (1 \; - \; a)\cos^{p}\theta \quad (2).$$

The first cosine term describes the broad distribution as a function of θ; the second one is the narrower component, strongly dependent on the exponent $p >> 1$. The data fitting is done by adjusting the main parameters of the function, namely, a, p, and s (the shift of the experimental point with the greatest thickness with respect to the real center of the plume):

$$F(\theta) = \; \{a * cos\,cos\,(\theta - s) \; + (1 - a) * [cos\,cos\,(\theta - s)\,]^{p}\} * [cos\,cos\,(\theta - s)\,]^{3} \quad (3),$$

getting a theoretical curve with a R^2 coefficient as high as possible. The $\cos^3\theta$ corrective term is added for considering the planar geometry of the substrate [20]. The application of the bi-component model can fit very well the experimental curve, using the parameters reported in Table II:

Table II – Bi-component distribution parameters maximizing the fitting with the experimental curve.

a	0.05
p	12
s (°)	-0.86
R²	0.9995

Venkatesan et al. [26] also identified a similar bicosine plume distribution in the process of PLD for YBCO films, with $p = 11$. They found that the $\cos^p(\theta)$ component comes from the ablation mechanism of the target bulk, while the $\cos\theta$ contribution results from the melting and isotropic evaporation of the superficial target layers, due to the residual surface heating after laser impact. The same distribution profile ($a = 0.11$, $p = 15$) was obtained under similar laser energy conditions in the case of (Pr,Sr)MnO_3 films deposited by PLD [27]. Pattini et al. [28] conducted a study showing that comparable plume distribution mechanisms arise when depositing $CuGaSe_2$ films via PED. They found that when the e-beam voltage is 16 kV, a thermal isotropic evaporation occurs from the surface of the target (a = 0.03), whilst the forward-peaked component ($p = 4$) is attributed to the high-energy congruent ablation underneath.

Since the experimental plume distribution observed in the present work is very close to what reported in the above literature works, one can conclude that similar mechanisms could occur in the case of BaFeO films deposited by PED. It thus emerges that a small but not negligible thermal evaporation mechanism ($a = 0.05$) occurs simultaneously with the ablation during the BaFeO deposition process at 16 kV.

The influence of the expansion velocity on the collisions involving the plasma species inside the high-energy pulsed plumes is widely recognized to affect the angular expansion of vapours from the target. This relationship can be described directly by the effect of the plasma pseudo-Mach number, M, (calculated as the ratio of the plasma velocity to the speed of sound), on the p exponent of the non-thermal expansion, as expressed below:

$$p = 1 + 2.13\frac{\gamma^{1/2}M}{\gamma^{1/2}M+1} + \gamma M^2 \quad (4),$$

where $\gamma = 1.67$ represents the ratio between the specific heats at a constant pressure and volume for a monatomic gas. Thus, it can be inferred from the equation above that, for the BaFeO target ablated at 16 kV, the plume expansion velocity is about 2.4 times the speed of sound. As a useful parameter for assessing the energetic impingement of the plasma on the thin film growth on the substrate, M denotes the ratio of directed kinetic energy to random thermal motion in the plasma [29].

Since $\theta = \arctan(x/d)$, where $d = 7$ cm is the target-substrate distance and x is the distance between the measured point on a planar substrate and its center, the two cosine components have been deconvoluted and plotted in Figure 10a as a function of the distance x. The $\cos^p(\theta)$ component, which is the main result of the fast, high-energy plume formation process, prevails on the other one over the 6 cm-wide substrate. At wider distances from the substrate center, the $\cos^p(\theta)$ contribution rapidly tends to zero until its contribution completely disappears at $\theta > 30°$. The broader and more "isotropic" distribution, whose effect is always minor over the entire substrate, becomes increasingly important at larger distances.

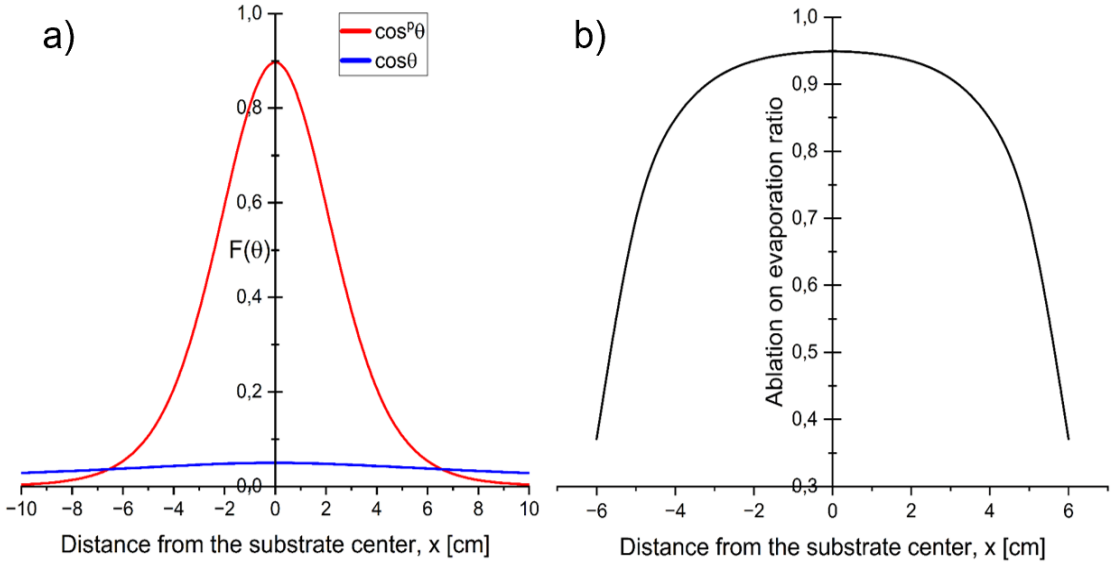

Figure 10 - a) Comparison of the distribution of the two components of the bicosine model over the substrate. b) Ablative/evaporative contribution ratio trend calculated on different sections of the substrate.

The weights of the two components at different distances from the center of the substrate, are graphed in Figure 10b. As it appears in Figure 6c, within 3 cm from the substrate center, the ablative component always contributes over 90% to the formation of the BaFeO film. The ablative contribution decreases as the distance increases, and at 6 cm from the center, it only contributes slightly over one third, while the thermal component dominates.

II. Structural analysis

The stuffed tridymite-like texture and purity were studied using XRPD and Raman spectroscopy at various locations on the substrate.

The XRPD patterns measured on the six regions of the substrate are displayed in Figure 11. All the XRPD measurements on the film are compared with that related to the polycrystalline ceramic target prepared as specified in section 3.1. The diffraction patterns from outer sections (#1, #2, #3) exhibit three high-intensity peaks, which are identified as BaFeO reflections originated by the (h00) family of lattice planes. The comparison with the starting target powder pattern suggests the tendency of BaFeO films to grow preferentially along certain crystallographic directions.

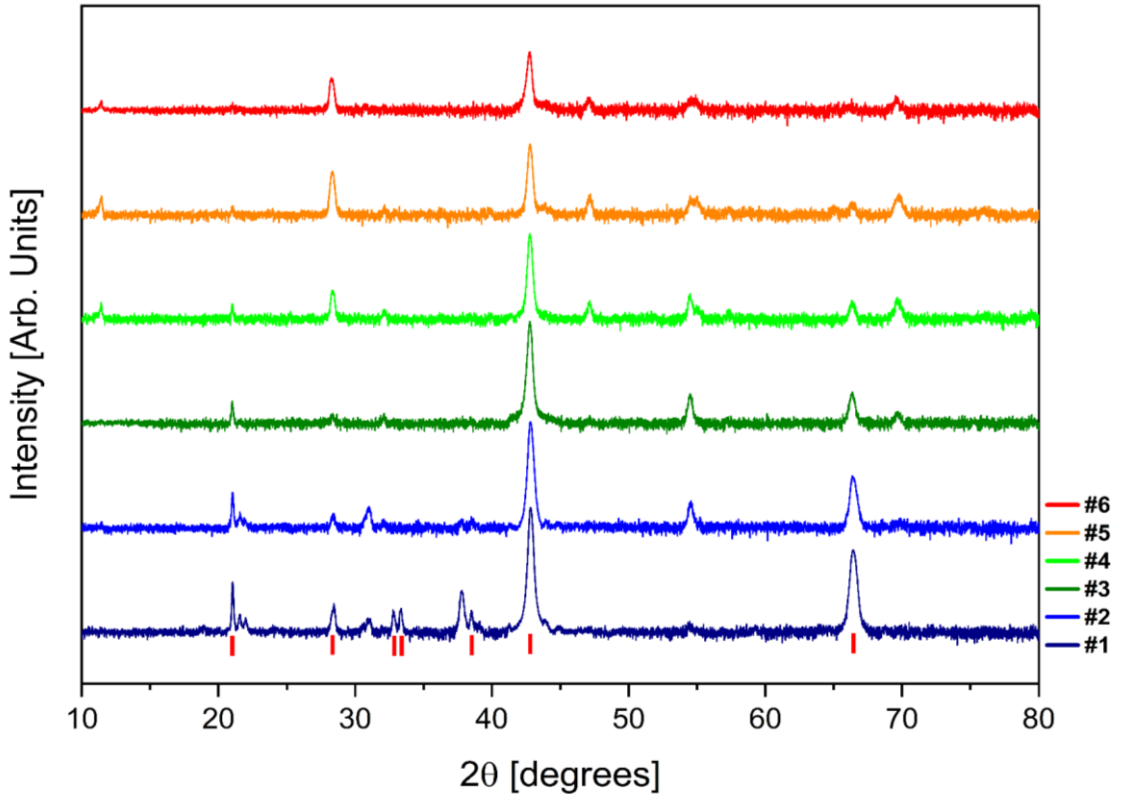

Figure 11 - XRD patterns of the BaFeO film measured on different sections of the substrate and compared with the pattern of the starting target (intensity is in log scale). Red ticks indicate the most intensive BaFeO reflections. The scale factor of intensities has been remodeled in order to make all minor peaks visible.

Besides that, the presence of a spurious phase was observed, as revealed by a series of low intensity reflections not fitted by the BaFeO diffraction pattern (Figure 12), and an

optimal matching was found with a Ba-rich structure, $Ba_2Fe_2O_5$ [30]; however, the amount of this secondary phase gradually vanishes moving from peripheral (#1, #2 and #6) to central sections (#3, #4 and #5), where only several peaks ascribed to BaFeO phase are detected.

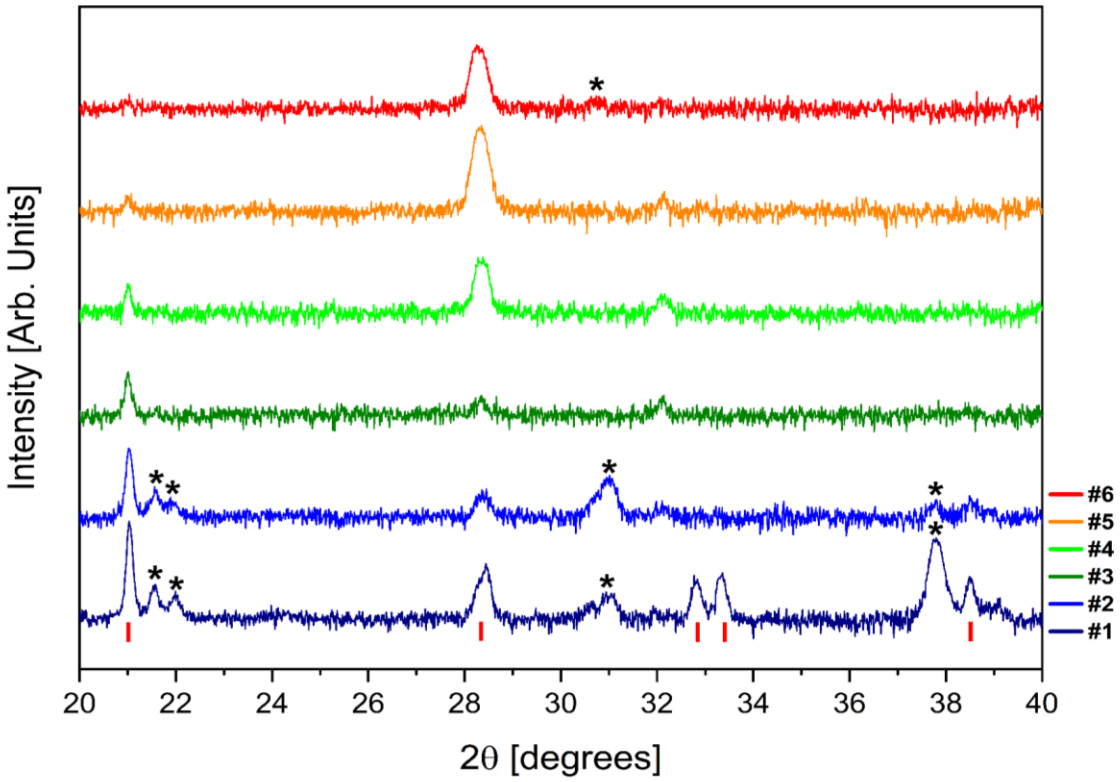

Figure 12 - Detail of XRD in the 20°-40° 2θ range, where the presence of peaks belonging to the secondary $Ba_2Fe_2O_5$ phase can be detected (*).

Raman analysis was performed by collecting measurements at the center of each substrate section. This technique is suitable to take localized measurements on individual spots of the material surface. Globally, no net differences in Raman-bands patterns were found by the comparison with the BaFeO ceramic target (Figure 13a), apart from a weak band appearing on peripheral substrate sections at approximately 65 cm^{-1} (Figure 13b). This band, which is absent in the BaFeO powder pattern and, so, is likely ascribed to the $Ba_2Fe_2O_5$ phase, confirms the increase of secondary phases when moving away from the central section of the film, consistently with the XRPD measurements.

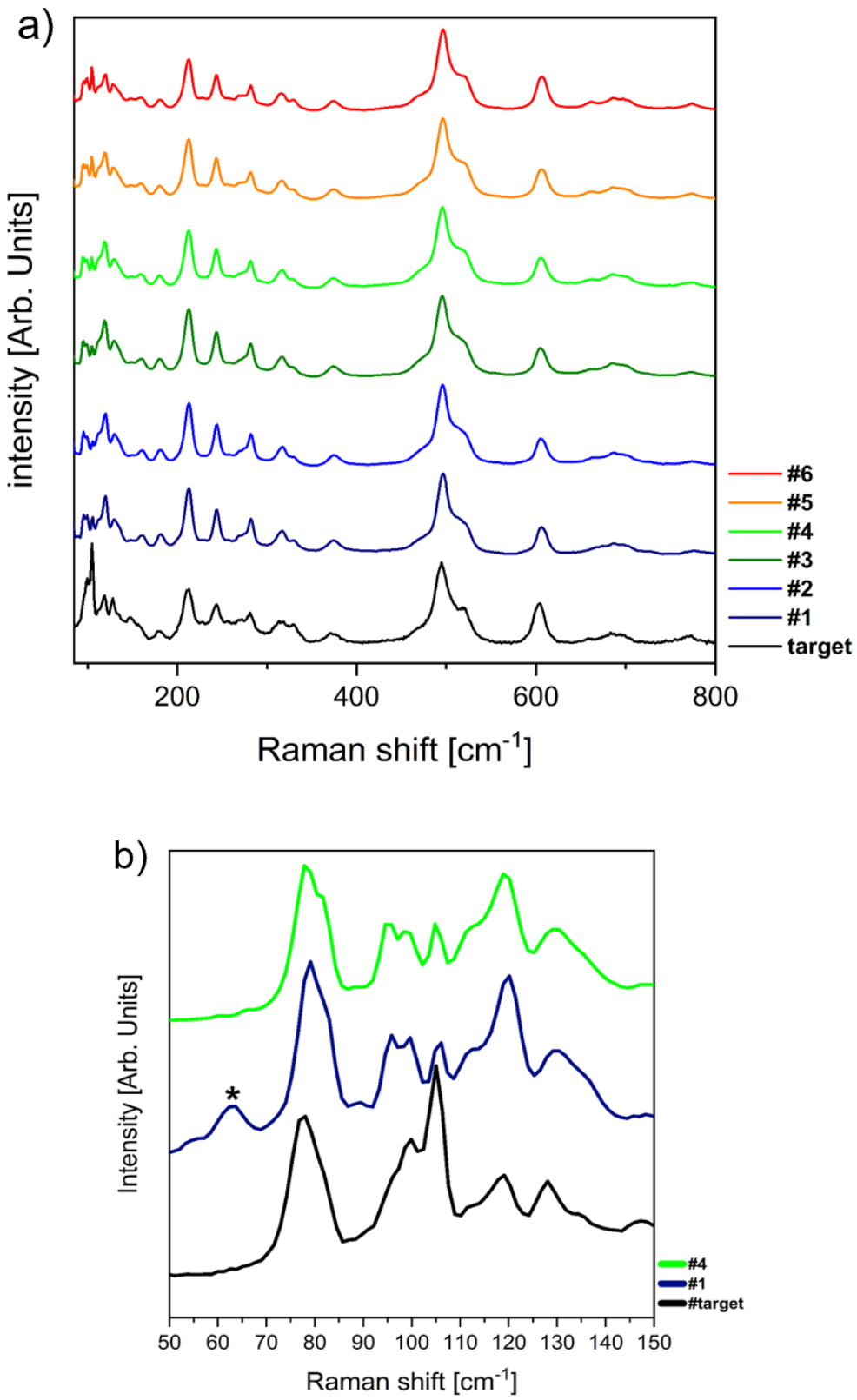

*Figure 13 – a) Raman spectra of the BaFeO film measured on different sections of the substrate and compared with the spectrum of the starting target. b) Raman spectra close-up in the 50÷150 cm^{-1} wavenumber range for the starting target, the peripheral section #1 and the central section #4. The * symbol highlights the presence of a spurious Raman mode not ascribable to the γ-$BaFe_2O_4$ phase.*

All the above-described results are observed to follow a pattern similar to that of the plume distribution discussed in the previous paragraph. In the central sections of the sample, where the film is thicker and where the ablative $\cos^p(\theta)$ component is dominant over the evaporative $\cos(\theta)$ one, both XRPD and Raman confirm the only existence of the stoichiometric phase of $BaFe_2O_4$. In the peripheral sections of the substrate, where the evaporative $\cos(\theta)$ contribution is a small but detectable factor, a barium-rich secondary phase ($Ba_2Fe_2O_5$) becomes visible in the XRPD. Additionally, the Raman spectrum shows a band that is not apparently related to the $BaFe_2O_4$ phase. Table III summarizes the crystalline phases observed in the different substrate sections.

Table III – Summary of the phases observed in each section analyzed on the substrate.

Substrate Section	**Observed phases**
#1	$BaFe_2O_4 + Ba_2Fe_2O_5$
#2	$BaFe_2O_4 + Ba_2Fe_2O_5$
#3	$BaFe_2O_4$
#4	$BaFe_2O_4$
#5	$BaFe_2O_4$
#6	$BaFe_2O_4 + Ba_2Fe_2O_5$

III. Compositional analysis

Energy dispersive X-ray spectroscopy (EDX) was used to evaluate the chemical composition of the BaFeO film along the substrate. Although some experimental limits, such as the poor electrical conductivity of both quartz substrate and BFO film and the unavoidable errors in determining the oxygen percentage, due to the presence of silica signals, rule out the possibility to get a quantitative description of the film composition (especially in the thinnest film sections), the obtained information still helps to understand the relative Ba:Fe ratio variation as a function of the deposition radius. Figure 14a shows both all the spots of the BFO film at which measurements were taken and their corresponding values in terms of barium, iron (III), oxygen and Ba/Fe ratio percentages

(Figure 14b, c, d and e respectively). Considering the elements composition in $BaFe_2O_4$ (Ba≈14.3%; Fe≈28.6%; O≈57.2%; Ba:Fe = 0.5), it is easily understood that Ba/Fe ratio is globally greater than 0.5, which means that a certain out-of-stoichiometry amount of barium ions was deposited during the process, thus leading to the formation of impurities, as actually has emerged from PXRD and Raman patterns. At the same time, when moving towards the central sections it can be easily observed that all the atomic percentages tend to the nominal BaFeO values.

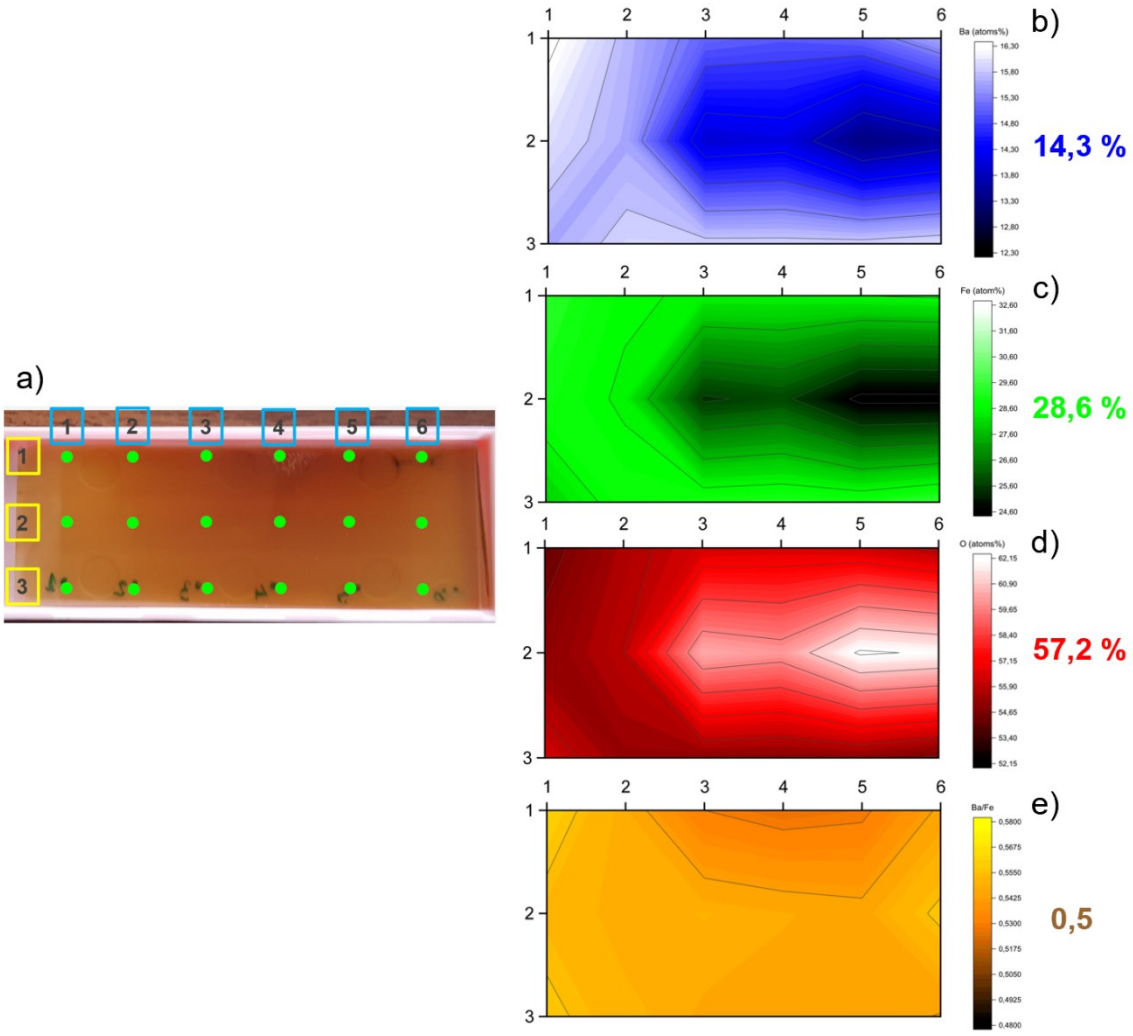

Figure 14 – a) Schematics of EDX-based mapping experiment performed on the BFO/quartz system: each film section (blue boxes) was divided into three parts (yellow boxes), where the measurements were acquired (green spots). A strip of carbon tape was applied on the top of the film, i.e. along the first horizontal section. b)-c)-d) Distribution of barium, iron and oxygen atomic percentages, respectively, and e) the derived Ba/Fe ratios collected along the film. All data were interpolated with the Origin software. The values on the right side are referred to the nominal BaFeO composition.

Table IV shows the atomic content of barium, iron (III) and oxygen measured along the major axis of the substrate (yellow section 1 in Figure 14a), i.e. where the center of the plume has been localized. The extrapolated percentage excess of Ba with respect to the stoichiometric $BaFe_2O_4$ is also reported.

Table IV – Chemical composition of the BaFeO film measured on various sections of the substrate, together with the excess of Ba over the stoichiometric composition.

Substrate section	**%Ba**	**%Fe**	**%O**	**%Ba excess**
#1	16.4	29.3	54.3	14.7
#2	15.7	28.7	55.6	9.8
#3	15.1	28.5	56.4	5.2
#4	15.0	28.5	56.5	4.9
#5	15.1	28.6	56.3	5.1
#6	15.6	28.7	55.7	9.2

By combining the experimental plot from Figure 10b and the data in Tables III and IV into the same diagram displayed in Figure 15, we can simultaneously examine the spatial distributions of the plasma expansion mechanisms, crystalline phases and Ba excess as a function of the substrate position. It is self-evident the very strong correspondence between the contribution of the thermal evaporation mechanism and the barium content excess on the film. A possible hypothesis is that these two effects are correlated: the thermal evaporation process from the target surface leads to an excess formation of barium in the plume. This phenomenon is more prominent at increasing deposition angles, as illustrated in Figure 10, since the evaporative component gains importance over the ablative component. Moreover, based on the XRD and Raman analyses, even the secondary Ba-rich $Ba_2Fe_2O_5$ phase becomes detectable at higher angles. Therefore, it is suggested that the evaporative contribution in the plume, which itself contains an excess of barium with respect to the stoichiometric phase, is responsible for the formation of the secondary phase $Ba_2Fe_2O_5$.

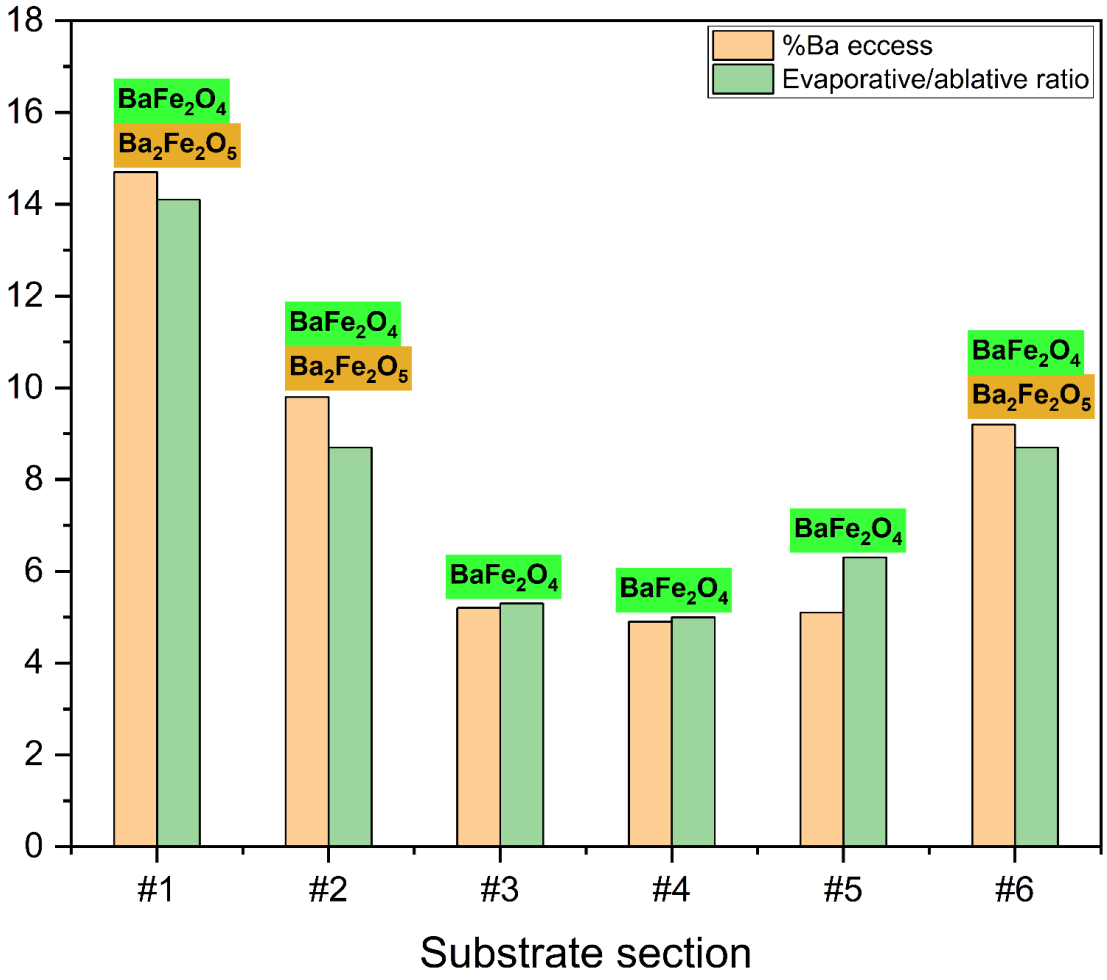

Figure 15 – Trends in the ratio of evaporative to ablative components (green), excess Ba (orange) and detected crystalline phases as a function of the analyzed substrate sections.

It could be that the excess of Ba in the plume leads to the growth of the $Ba_2Fe_2O_5$ secondary phase directly on the substrate, however, this extra Ba content should also produce other preferred phases in an oxygen-rich environment, including BaO. Nevertheless, the sole spurious phase appearing is $Ba_2Fe_2O_5$.

As the second hypothesis, $BaFe_2O_4$ and $Ba_2Fe_2O_5$ could have originated directly from the target, and subsequently ejected, transported as vapour and condensed on the substrate. Assuming that all high-energy ablated species reaching the substrate are deposited with unitary sticking probability, it is possible that the phases already present in the plume are then deposited with the same ratio on the film. The relative abundance of the two species coming from the plume can be written as a simplified linear combination of two phases, $BaFe_2O_4$ and $Ba_2Fe_2O_5$, starting from the elemental composition measured by EDX and

listed in Table V.

It can be deduced that the plume arriving towards the center of the substrate exhibits the following formula:

$$13\ BaFe_2O_4 + Ba_2Fe_2O_5,$$

while in the furthest region of the substrate, section #1, located about 30° from the center of the plume, the composition is 3.5x richer in $Ba_2Fe_2O_5$:

$$13\ BaFe_2O_4 + \frac{7}{2}\ Ba_2Fe_2O_5$$

It is clear that as one moves from the center towards the periphery of the substrate, the spurious phase is increasingly present on the film, as the evaporative contribution of the plume, and becomes detectable by XRD and Raman analysis. Since the thermal evaporation component arises from the shallower part of the target, it can be inferred that the anomalous $Ba_2Fe_2O_5$ phase emanates from the surface of the target, whereas the γ-$BaFe_2O_4$ is produced internally within the target. To provide an explanation for the origin of the spurious phase on the target surface, it is necessary to emphasize that the evaporative component is the result of the change of state from solid to liquid and then to vapour under thermodynamic equilibrium. In this regime, state transitions are regulated according to the BaFeO phase diagram [31] shown in Figure 16. The diagram highlights the difficulty in obtaining a pure γ-$BaFe_2O_4$ phase, mainly due to the transfer of several chemical elements with significantly different atomic masses. During the PED process, the excess heat generated as a result of the interaction between the e-beam and the target moves towards the surface, where it tends to increase the temperature of the first layers, even up to a few thousand degrees [32]. In this particular scenario, by starting with a mixture of BaO and Fe_2O_3 consisting of equal parts, surplus heat can melt the surface target and ultimately create the vapour. After the e-beam pulse, the surface liquid cools along the left curve shown in the diagram. As it condenses, it tends to become richer in Ba and generates the $Ba_2Fe_2O_5$ phase on the surface, alongside with the γ-$BaFe_2O_4$ phase. The heat produced by the following electron beam pulse melts and evaporates an area in which γ-$BaFe_2O_4$ and $Ba_2Fe_2O_5$ phases coexist. These phases are then distributed in the

plume according to previous analysis. The double phase is then restored on the target during the cooling process between the pulses. This cyclic process proceeds throughout the PED deposition.

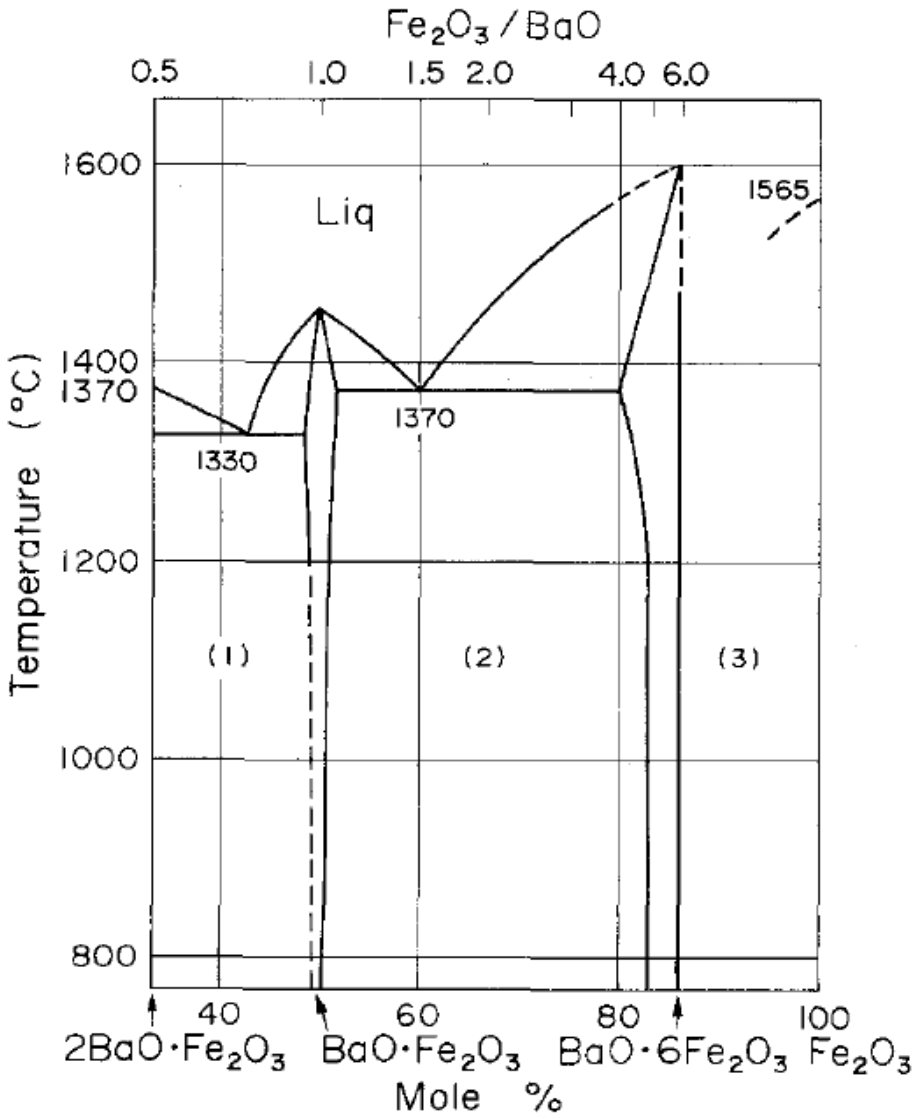

Figure 16 – Phase diagram of the Ba–Fe–O system. Reproduced with permission from [31]. (1) 2BaO · Fe_2O_3 + BaO · Fe_2O_3; (2) BaO-Fe_2O_3 + $Ba_{0.6}Fe_2O_3$; (3) BaO-6Fe_2O_3 + Fe_2O_3. In Section (1), both $Ba_2Fe_2O_5$ and γ-$BaFe_2O_4$ phases coexist.

4.3.3 Role of substrate type on BaFeO crystal quality

Another aspect investigated in this study is the role of the substrate on the PED growth of BaFeO thin films (Figure 17a). The substrate is not just the mechanical support over

which a film adheres. The substrate may itself serve as an active part of a BaFeO film-based device (such as a metal layer), or it may go on to influence crystal growth depending on the starting crystal structure and morphology, by promoting epitaxial growth or a polycrystalline structure with a preferential orientation of grains. For this study, 1x1 cm^2-large amorphous (quartz), microcrystalline (SiO_2/Si and platinum-coated quartz), and single-crystalline (MgO) substrates were exploited. Depositions were carried out at the same operating PED conditions reported in Table I. The substrate temperature was varied between 700°C and 800°C. To get quantitative information regarding the preferred crystallographic orientation, the texture coefficients (T_C) related to some crystallographic orientations (hkl) have been determined by the following relation:

$$TC(hkl) = \frac{\frac{I(hkl)}{I_0(hkl)}}{\sum_n \frac{I(hkl)}{I_0(hkl)}} \times 100$$

Where I and I_0 represent the intensities of the observed reflections in the experimental XRD pattern and in an ideally randomly oriented powder distribution, respectively. For this analysis, the following n = 10 different crystallographic directions of the γ-$BaFe_2O_4$ phase were considered: (110), (040), (021), (111), (240), (221), (061), (002), (400) and (190). According to the above formula, if the T_C value related to a specific direction is greater than 10%, then it will be a preferred growth orientation of the resulting thin film.

I. $BaFe_2O_4$ films on amorphous and microcrystalline substrates

The analysis of the PXRD patterns of the BaFeO films deposited on amorphous and microcrystalline substrates reveals that no secondary phases are observed within the detection limits of the employed experimental conditions (Figure 17b). This aspect confirms the plume distribution represented in Figure 6c: on substrates smaller than 1 cm^2, the ablative component is by far the most prevalent, and leads to the sole formation of γ-$BaFe_2O_4$. XRD patterns of BaFeO grown on quartz (Q_{800}) and on Pt-coated quartz substrates (Pt_{800}) at 800°C have similar distribution of the peaks. Conversely, on SiO_2/Si, the deposition at 800°C (Si_{800}) produces an extremely different XRD pattern compared to previous case. Instead, an extra test carried out at 700°C (Si_{700}) revealed a diffraction pattern similar to Q_{800} and Pt_{800}, thus suggesting that depositions on silicon are

significantly influenced by the growth temperature. As a result, although only the γ-$BaFe_2O_4$ phase is formed, the intensities of individual reflections vary with temperature, resulting in notably different T_C values.

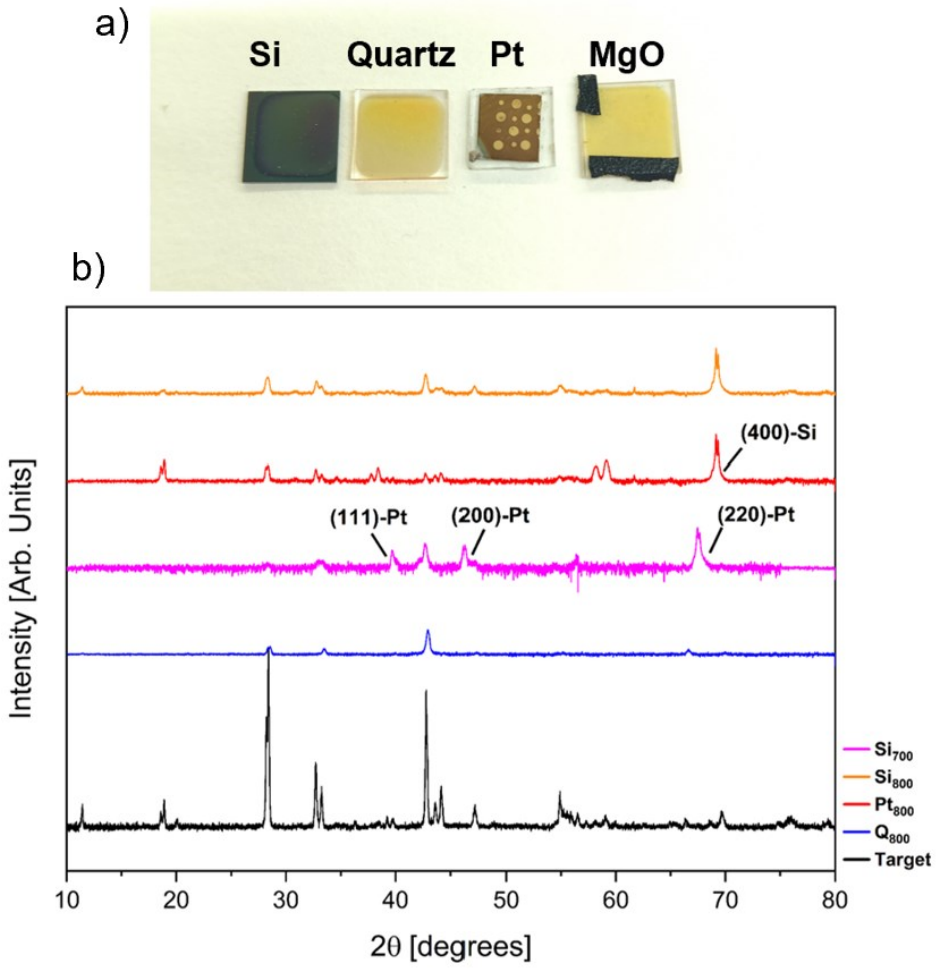

Figure 17 – a) examples of BaFeO films samples deposited on silicon, quartz, platinum and monocrystalline MgO substrates (dots on platinum are made of metallic gold); b) PXRD patterns collected for BaFeO samples grown on different substrates in 10-80° 2θ range. The intensities are reported in log scale to facilitate the visualization of all BaFeO reflections The measurement related to the BaFeO target is reported as a reference (black).

The T_C values extracted from the diffraction patterns show few differences (see Figure 18). The grain preferred orientation in BaFeO film on quartz and Pt-coated quartz ('Q_{800}' and 'Pt_{800}' respectively) is similar, with (h00) preferential orientation. In contrast, depositing BaFeO on SiO_2/Si at 800°C ("Si_{800}") led to a higher occurrence of (0k0)- and (0kl)- oriented crystalline domains. On the contrary, the (h00) reflections dominate in the Si_{700} sample grown at 700°C, akin to the observations made on quartz and platinum. This

suggests that temperature plays a crucial part in choosing the preferred crystal growth orientation on this type of substrate.

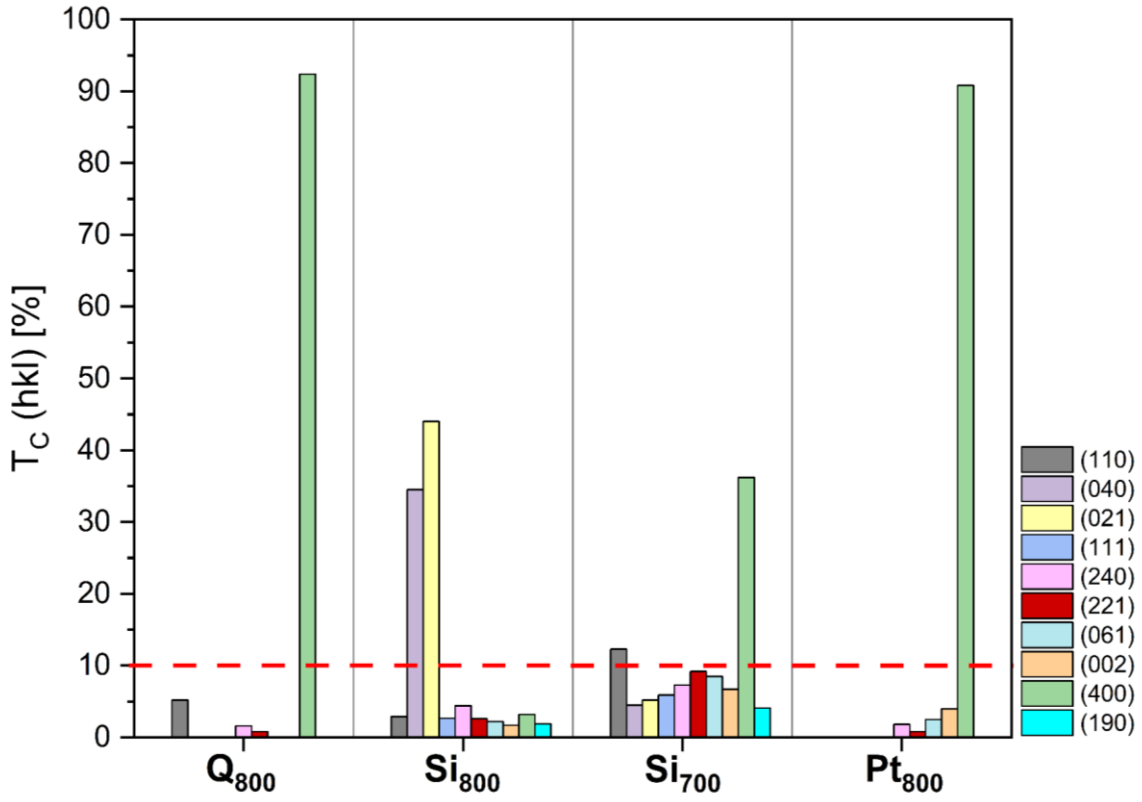

Figure 18 – The extrapolated T_C distributions related to ten (hkl) lattice planes. Values above the dashed red line indicate that the corresponding reflection represents a preferred growth orientation.

It is not trivial to give a comprehensive explanation of the differences in T_C that occurred based on the type of substrate. However, a rough interpretation of these results could be found by taking into account the different thermal conductivity of the materials, which could have some effect on the local temperature actually perceived by the plasma on the substrate surface. In fact, the reduction in temperature and the choice of poorly conducting substrates such as quartz seem to result in very similar textures. However, this hypothesis needs to be confirmed and further studies are underway.

In summary, it can be concluded that all the substrates under study not only allowed the deposition of BaFeO film with the same stoichiometry of the starting target, but they also determined a preferential growth control of crystalline domains through a probable combination of temperature and substrate properties. Moreover, these results suggest that

the PED technique is optimal to produce barium ferrite films on a number of key substrates for the electronics industry.

II. $BaFe_2O_4$ films on MgO single crystals

Considering the relevant dependence of the crystal structure on the starting substrate, the growth of BaFeO on a cubic single crystal MgO-(111) substrate (1 x 1 cm^2) was tested. Such a configuration should be able to produce a heteroepitaxial arrangement of type (h00)-BaFeO/(111)-MgO: in fact, since the (111)-planes of a face centered cubic-type unit cell are precisely the closed packed planes of the lattice, being crystallographically equivalent to the basal (001)-planes of a hexagonal closed packed structure, the growth of the BaFeO layers would be oriented so as to have its six FeO_4 tetrahedra-membered ring oriented precisely parallel to the plane of the substrate (Figure 19). As shown in Table V, the lattice mismatch values (*f*), here calculated by considering the average oxygens distances of FeO_4 sequences running along their three directions, are around values suitable for epitaxial growth (~4-6%); moreover, the negative value indicates that the BaFeO structure will presumably undergo biaxial compression along the entire interface between layers.

Table V – Lattice parameters and structural properties of MgO and $BaFe_2O_4$.

	Lattice parameters	Space group	Lattice constants (Å)	***f***
MgO (111)	a = 4.221 Å; α = 90°	*Fm-3m*	2.978 (O-O)	**- 5.46% (d_1)**
$BaFe_2O_4$	a = 8.437 Å; b = 18.998 Å; c = 5.384 Å; α = 90°	*$Cmc2_1$*	d_1 = 3.15 d_2 = 3.12 d_3 = 3.17	**- 4.55% (d_2)** **- 6.06% (d_3)**

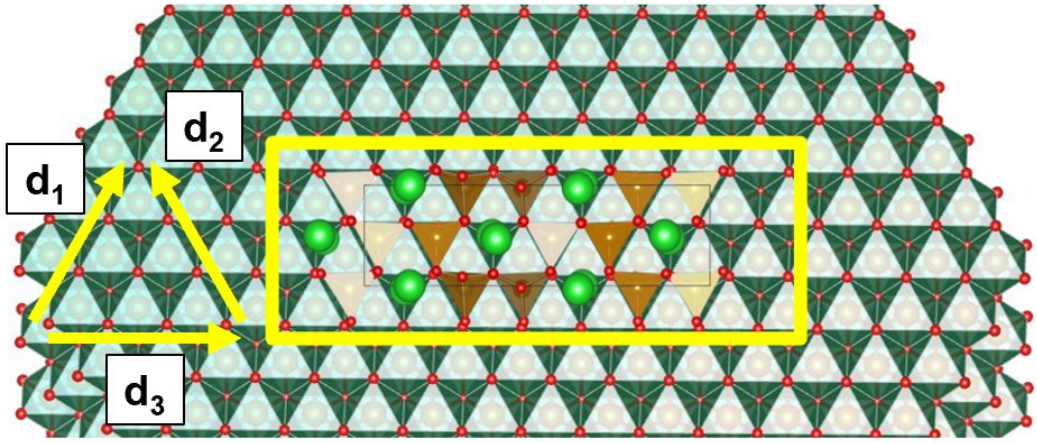

Figure 19 – Superposition of MgO (green, below) and BaFeO structures projected on (111)- and (100)-lattice planes, respectively. d1, d2 and d3 represent the three directions along which (h00)-BaFeO lattice planes undergo the biaxial strain induced by the lattice mismatch f.

The BaFeO deposition was carried out by replicating the same experimental conditions listed in Table I, unlike the total number of discharges which was reduced to $3x10^4$ pulses for obtaining thinner layers and avoiding thickness-induced lattice strains.

Figure 20 shows a preliminary collection of SEM images acquired on the deposited film, which reveals the presence of several hexagonal-shaped crystalline domains stacked in such a way as to form columns of variable width and height (100-500 nm and 80-100 nm, respectively, as evidenced by the images collected on the tilted sample), with some of them partially inverted. Similar architectures are presumably an effect of the growth orientation of BaFeO grains. The presence of macroscopic defects such as cracks and holes due to thermal deformations and poor adhesion of the ablated material to the substrate is not observed.

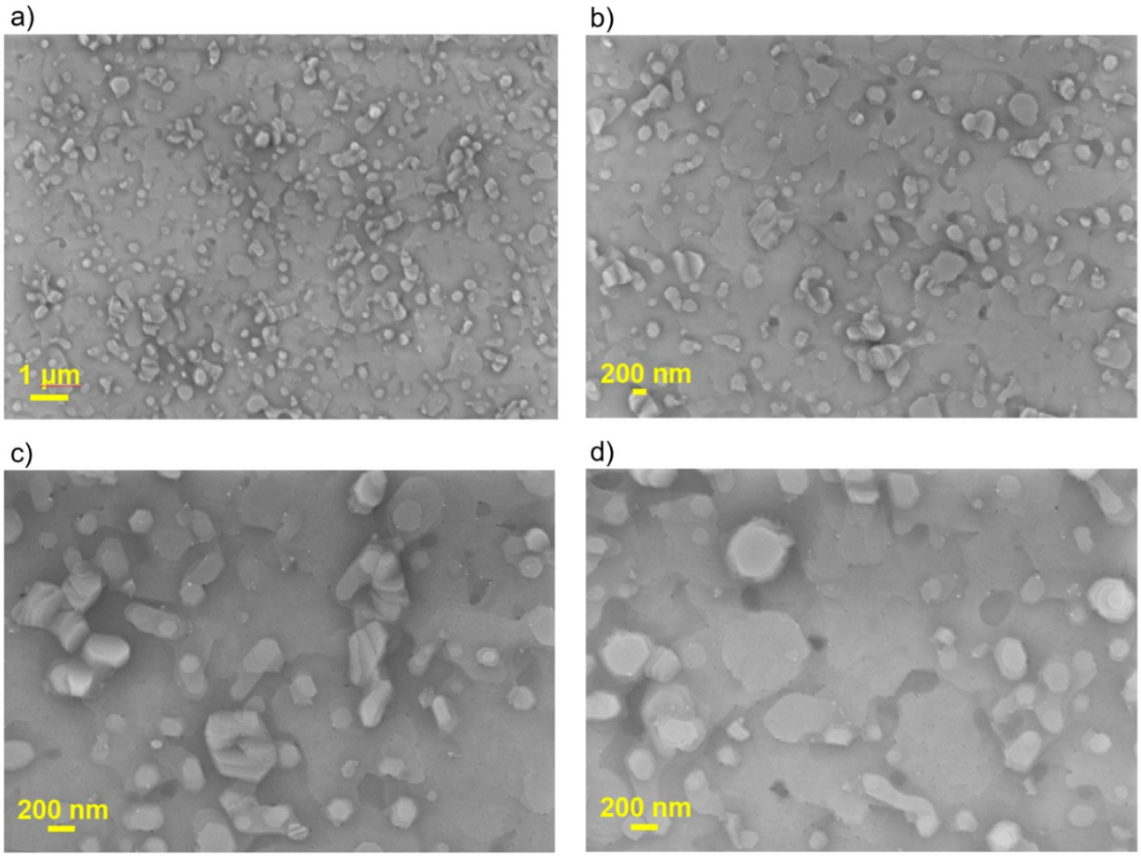

Figure 20 – Planar SEM images collected with a 20k X (a), 30k (b), 60k (c,d) magnification.

The PXRD pattern shown in Figure 21 shows that the set of planes with (h00) Miller indices constitute the unique out-of-plane orientation, although other marginal peaks attributable to BaFeO are present. No impurities or other BaFeO polymorphs are detected.

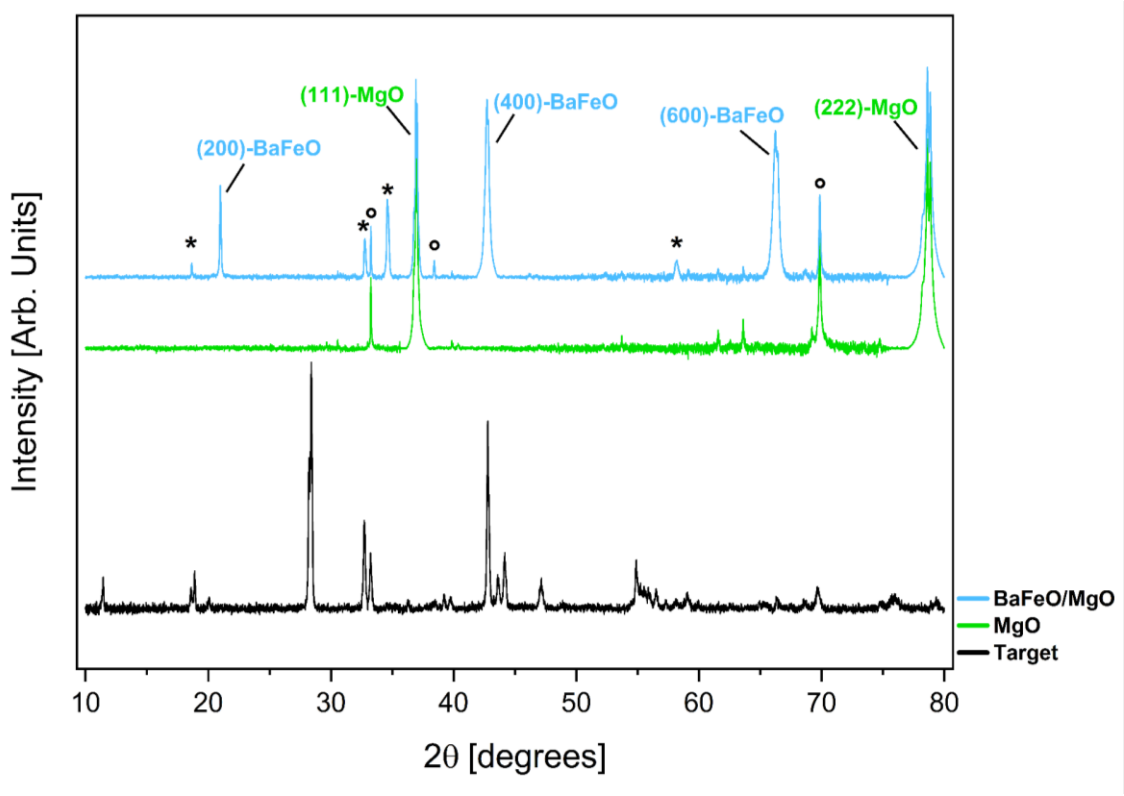

*Figure 21 – XRD patterns of a BaFeO film grown on MgO substrate (blue). *-Symbols indicate other BaFeO reflections, ° ones refer to the copper X-ray source-related spurious peaks arising from the intense (h00)-$BaFe_2O_4$ and (hkl)-MgO reflections. The XRD patterns of MgO substrate (green) and of BaFeO starting target (black) are also shown for comparison.*

In addition to the standard *θ-2θ* measurement, polar figures of the reflections having the highest XRD intensity were collected. As can be seen in Figure 22, the same analysis was carried out even for the sample grown at 800°C on quartz, to highlight the net effects of the substrate on the lattice texture. The reflection intensity was collected as a function of the χ and *φ* angles, at a constant $2\theta = 28.45°$, corresponding to the (221)-peak position. The film grown over the MgO-(111) substrate shows six peaks at $\chi \approx 40°$. Considered that, as per the *θ-2θ* measurements, the (400) is found as the normal direction (ND), the {221} are expected, based on the angle between the direct space (400) and (221) vectors, at $\chi = 42.01°$, in excellent agreement with the reported data (Figure 22a). The multiplicity of the (hkl) reflections in an orthorhombic crystal system is 8, with only four of these available in the polar figure measurement (the other four are expected below the equatorial plane). In the present case however 12 intensities are detected at the same χ value, with *φ* periodicity of about 60° (Figure 22b). Such behavior can be explained by

comparing the lattice geometries of the substrate and BaFeO. MgO in (111) direction displays a three-fold symmetry axis, while BaFeO, with pseudo-hexagonal symmetry, is not symmetry-invariant upon three-fold rotations. Therefore, BaFeO can nucleate with the same probability having the *bc* plane rotated by 120°, giving rise to three *a*-axis sharing twin variants (Figure 22d).

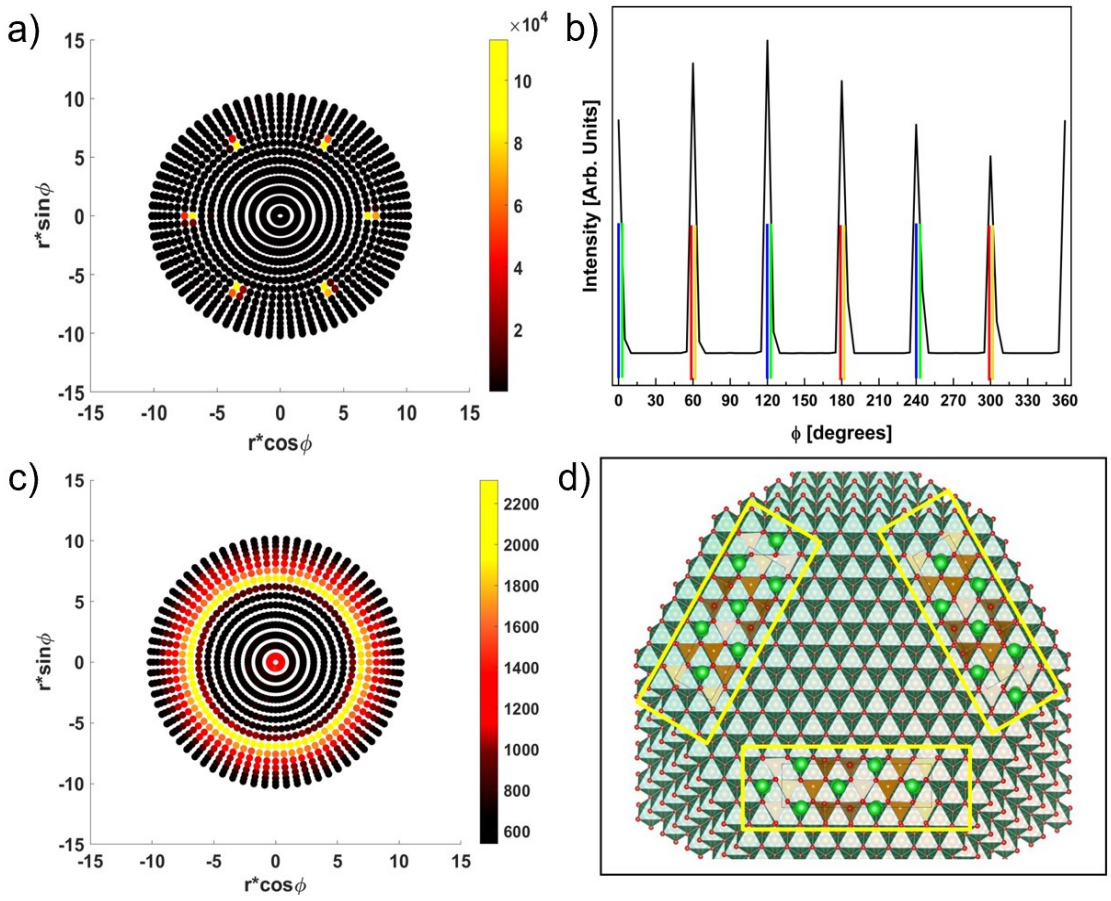

Figure 22 – Pole figures of BaFeO/MgO-(111). a)-c) (221)-reflections collected for BaFeO/MgO-(111) and for Q_{800}, respectively, in polar coordinates. b) φ-scan collected for the (221) reflection at 2θ = 28.45° and χ=40°: the pattern is obtained by the combination of the {221} family of reflections (vertical lines with same color) with the three possible twin variants (different colors). d) The three possible orientations of the BaFeO unit cell on the MgO(111) substrate.

Conversely, the polar figure collected in the same conditions for the film grown on quartz shows a continuous "ring" of intensity along the entire φ-scan at the same χ angle range, thus suggesting that the crystalline domains, despite being characterized by a specific ND preferential orientation, lack of in-plane coherence, giving rise to fiber-like texture (Figure 22c). Furthermore, the presence of nonzero intensity in the ND for the (221)

reflection, as well as at about 35° and 55° suggests that part of the crystallites have grown with different orientations, being related to the (110) and (061) reflections (Figure 23a, b). Such results, in agreement with the previously *θ-2θ* pattern, suggest the presence of a distribution of preferential orientations rather than a single one.

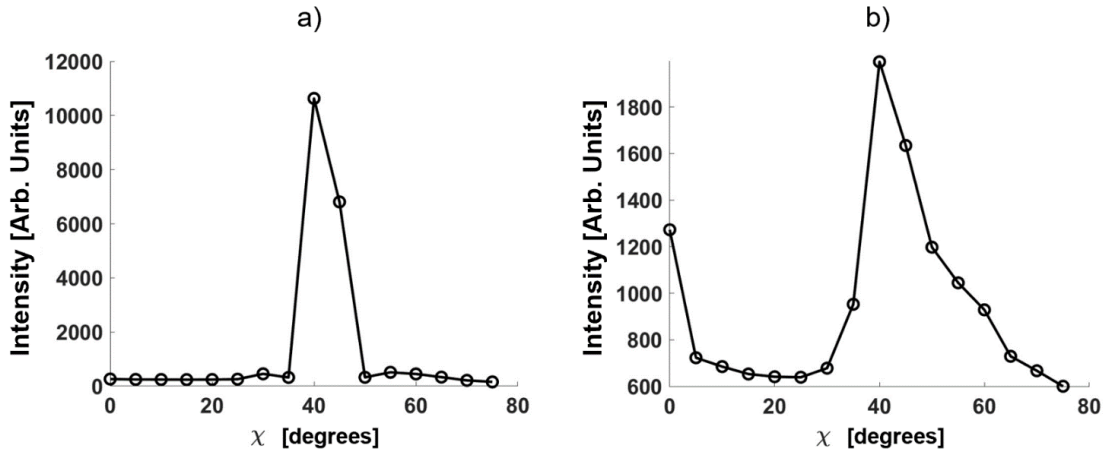

Figure 23 – a)-b) χ-scans collected for BaFeO/MgO-(111) and BaFeO/quartz films, respectively. A sharper peak is observed at ~ 40°, as a result of the epitaxy.

Considering all the described net differences, this exploratory structural study proves that the use of monocrystalline (111)-MgO substrates is effective in inducing not only a crystal growth along a single out-of-plane orientation, but also good heteroepitaxy of the BaFeO layers. This result opens up the possibility of realizing PED epitaxial systems by integrating BaFeO with other epitaxial substrates or epilayers, thus extending the range of functionalities for novel devices, as is the case of $BiFeO_3$ [33].

4.4 References

[1] A. Anders *"Discharge physics of high-power impulse magnetron sputtering"* Surface and Coatings Technology (2011) 205, S1-S9

[2] H. Hoche, C. Pusch and M. Oechsner *"Corrosion and wear protection of mild steel substrates by innovative PVD coatings"* Surface and Coatings Technology (2020), 391,125659

[3] G. M. Uddin, M. Jawad, M. Ghufran, M. W. Saleem, M. A. Raza, Z. U. Rehman, S. M. Arafat, M. Irfan and B. Waseem *"Experimental investigation of tribomechanical and chemical properties of TiN PVD coating on titanium substrate for biomedical implants manufacturing"* Int. J. Adv. Manuf. Technol. (2019),102, 1391-1404

[4] A. Biksa, K. Yamamoto, G. Dosbaeva, S. C. Veldhuis, G. S. Fox-Rabinovich, A. Elfizy, T. Wagg and L. S. Shuster *"Wear behavior of adaptive nano multilayered AlTiN/MexN PVD coatings during machining of aerospace alloys"* Tribology International (2010), 43, 8,1491-1499

[5] P. E. Hovsepian, Q. Luo, G. Robinson, M. Pittman, M. Howarth, D. Doerwald, R. Tietema, W. M. Sim, A. Deeming and T. Zeus "*TiAlN/VN Superlattice Structured PVD Coatings: A New Alternative in Machining of Al Alloys for Aerospace and Automotive Components"* Surf. Coat. Technol. (2006), 201, 265-272

[6] K. Bobzin, C. Kalscheuer, M. P. Möbius, C. Schulze and M. M. Marti *"High power pulsed magnetron sputtering tailored low temperature CrAlN + MoWS coatings for dry tribological contacts"* J. Vac. Sci. Technol. (2024), 42 (1), 013404

[7] K. Piotrowska, A. Granek and M. Madej *"Assessment of Mechanical and Tribological Properties of Diamond-Like Carbon Coatings on the $Ti_{13}Nb_{13}Zr$ Alloy"* Open Engineering (2020), 10, 536-545

[8] B. Yannick, B. Florent, T. Teddy, L. Anna-Sophie, M. Chirandjeevi, D. Christophe, G. Florence *"Review of graphene growth from a solid carbon source by Pulsed Laser Deposition"* Frontiers in Chemistry (2018), 6

[9] A. Yousif, M. M. Duvenhage, O. M. Ntwaeaborwa and H. C. Swart *"Role of Ga particulates on the structure and optical properties of $Y_3(Al,Ga)_5O_{12}$:Tb thin films*

prepared by PLD" Physica B: Phys. of Cond. Matter (2018), 535, 319-322

[10] L. Guoqiang, W. Wenliang, Y. Weijia and W. Haiyan *"Epitaxial growth of group III-nitride films by pulsed laser deposition and their use in the development of LED devices"* Surface Science Reports (2015), 70, 380-423

[11] J. Faupel, C. Fuhse, A. Meschede, C. Herweg and H. U. Krebs *"Microstructure of pulsed laser deposited ceramic–metal and polymer–metal nanocomposite thin films"* Appl. Phys. (2004)*, A* 79, 1233-1235

[12] J. Wang, J. B. Neaton, H. Zheng, V. Nagarajan, S. B. Ogale, B. Liu, D. Viehland, V. Vaithyanathan, D. G. Schlom, U. V. Waghmare, N. A. Spaldin, K. M. Rabe, M. Wuttig and R. Ramesh *"Epitaxial $BiFeO_3$ multiferroic thin film heterostructures"* Science (2003), 299, 1719-1722

[13] M. D. Strikovski, J. Kim and S. H. Kolagani *"Plasma Energetics in Pulsed Laser and Pulsed Electron Deposition"* Springer Handbook of Crystal Growth (2010), 1193–1211

[14] S. Tricot, C. Boulmer-Leborgne, M. Nistor, E. Millon and J. Perrière *"Dynamics of a pulsed-electron beam induced plasma: application to the growth of zinc oxide thin films"* J. Phys. D. Appl. Phys. (2008), 41, 175205

[15] M. Nistor, N. B. Mandache and J. Perrière *"Pulsed electron beam deposition of oxides thin films"* J. Phys. D. Appl. Phys. (2008), 41, 165205

[16] M. Nistor, F. Gherendi, M. Magureanu and N. B. Mandache *"Time-resolved spectroscopic study of a pulsed electron beam ablation plasma"* J. Optoelectron. Adv. Mater. (2005), 7, 979–984

[17] R. Henda, O. Al-Shareeda, A. McDonald and A. Pratt *"Deposition of iron pyrite via pulsed electron ablation"* Appl. Phys. A Mater. Sci. Process (2012), 108, 967–974

[18] Q. Jiang, F. Matacotta, M. Konijnenberg, G. Müller and C. Schultheiss *"Deposition of $YBa_2Cu_3O_{7-x}$ thin films by channel-spark pulsed electron beam ablation"* Thin Solid Films (1994), 241, 100-102

[19] S. Rampino, F. Bissoli, E. Gilioli and F. Pattini *"Growth of $Cu(In,Ga)Se_2$ thin films by a novel single-stage route based on pulsed electron deposition"*, Prog. Photovolt: Res.

Appl. (2013), 21, 588–594

[20] D. B. Chrisey and G. K. Hubler *"Pulsed Laser Deposition of Thin Films"* New York:Wiley (1994), 217

[21] D. Delmonte, R. Manfredi, D. Calestani, F. Mezzadri, L. Righi, M. Mazzer, F. Pattini, S. Rampino, G. Spaggiari and E. Gilioli *"An affordable method to produce $CuInS_2$ 'mechano-targets' for film deposition"* Semicond. Sci. and Tech. (2020) 35, 045026

[22] F. Orlandi, D. Delmonte, G. Calestani, E. Cavalli, E. Gilioli, V.V. Shvartsman, P. Graziosi, S. Rampino, G. Spaggiari, C. Liu, W. Ren, S. Picozzi, M. Solzi, M. Casappa and F. Mezzadri *"γ-$BaFe_2O_4$: a fresh playground for room temperature multiferroicity"* Nat.Commun. (2022), 13, 7968

[23] S. I. Anisimov, D. Bauerle and B. S. Luk'yanchuk *"Gas dynamics and film profiles in pulsed-laser deposition of materials"* Phys. Rev. (1993), B 48, 16, 12076

[24] H. Dang, M. Zhou and Q. Qin *"Optical emission spectrometric characterization of plumes generated from laser ablated $Pr_{0.67}Sr_{0.33}MnO_3$"* Applied Surface Science (1999), 140, 118-125

[25] R. F. Wood, J. N. Leboeuf, D. B. Geohegan, A. A. Puretzky and K. R. Chen *"Dynamics of plume propagation and splitting during pulsed-laser ablation of Si in He and Ar"* Phys. Rev. (1998), B 58, 1533

[26] T. Venkatesan, X. D. Wu, A. Inam and J. B. Wachtman *"Observation of two distinct components during pulsed laser deposition of high Tc superconducting films"* Appl. Phys. Lett. (1988), 52, 1193

[27] H. Dang and Q. Qin *"Angular distribution of laser-ablated species from a $Pr_{0.67}Sr_{0.33}MnO_3$ target"* Phys. Rev. (1999), B 60, 11187

[28] F. Pattini, M. Bronzoni, F. Mezzadri, F. Bissoli, E. Gilioli and S. Rampino *"Dynamics of evaporation from $CuGaSe_2$ targets in pulsed electron deposition technique"* J. of Physics D: Applied Physics (2013), 46, 245101

[29] R. Kelly *"On the dual role of the Knudsen layer and unsteady, adiabatic expansion in pulse sputtering phenomena"* J. Chem Phys. (1990), 92, 5047-5056

[30] X. D. Zou, S. Hovmoller, M. Parras, J. M. Gonzalez-Calbet, M. Vallet-Regi and J.C.

Grenier *"The complex perovskite-related superstructure $Ba_2Fe_2O_5$ solved by HREM and CIP"* Acta Crystallographica Section (1993), A 49, 27-35

[31] H. Kojima *"Fundamental Properties of Hexagonal Ferrites with Magnetoplumbite Structure"* Handbook of Ferromagnetic Materials (1982), 5, 305-391

[32] C. W. Schneider and T. Lippert *"PLD plasma plume analysis: a summary of the PSI contribution"* Appl. Phys. A Mater. Sci. Process (2023), 129,138

[33] D. Sando, A. Barthélémy and M. Bibes *"$BiFeO_3$ epitaxial thin films and devices: past, present and future"* J. Phys.: Condens. Matter (2014), 26, 473201

5 Preliminary screening of mixed stuffed-tridymite compounds

This chapter reports the preliminary results obtained from a screening of substitutional solid solutions performed on the reference structure of barium monoferrite , aimed at exploring the possible properties changes and tolerance of the stuffed trydimite structure upon chemical subtitutions. The choice of the substituting ions was mainly influenced by the reference literature on stuffed tridymites, but other types of substitution were attempted on both the A and B cationic sites, especially taking into account chemical species with ionic radii as similar as possible to iron(III) ions (in the range of ±0.1 Å); other features, such as the most stable oxidation state and the preferred coordination number with oxygen ions, were also considered. All the structural modifications attempted were probed using X-ray diffraction techniques.

5.1 Methods

5.1.1 Synthesis

All polycrystalline samples were produced via solid-state reaction, usually starting from the same conditions used for the synthesis of BaFeO (see chapter 3). After an optimization of the synthesis temperature, all the obtained compositions were pressed into a pellet, thermally treated for a second (and a third, if needed) time remove the possible unwanted phases and homogenize the solid solution.

The single crystal here used for structural characterization of iron-gallium solid solutions are merely extracted from the mixture after the synthesis process, without carrying out any specific reactions to perform the crystal growth.

For what concerns X-ray based technique and electric measurements, refer to previous chapters.

5.2 Results and discussion

5.2.1 Unresolved substitution trials

Table I display a list of unsuccessful substitution tests performed by using different transition metals on both A- and B-site of the monoferrite structure. In all these cases it was found tricky to determine the effectiveness of the process via solid-state reaction, as many by-products were obtained. Globally, given the explored synthesis conditions, ions exhibiting several oxidation states and able to be integrated in other coordination systems, as perovskite and spinel structures, seem not to be well stabilized within the stuffed trydimite structure.

Table I – Summary of the attempted chemical substitutions on BaFeO structure which have systematically produced impurities.

Compounds	Reactants	Synthesis conditions			Detected products
		Theoretical composition	Temperature (K)	Dwelling time (h)	
$Ba_{1-x}Fe_2Mn_{x/2}O_4$	$BaCO_3$ Fe_2O_3 MnO_2	x = 0.2; 0.5	1573	12	$BaFe_2O_4$ $BaFe_{12}O_{19}$[1]
$BaFe_{2-x}Mn_xO_4$	$BaCO_3$ Fe_2O_3 Mn_2O_3	x = 0.05; 0.1; 0.25; 0.5	1473	//	$BaFe_2O_4$ $Ba_2Fe_6O_{11}$[2] $BaMnO_{3-\delta}$[3]
$BaFe_{2-x}Cr_xO_4$	$BaCO_3$ Fe_2O_3 Cr_2O_3	x = 0.05; 0.25	1573	//	$BaFe_2O_4$ $BaFe_{12}O_{19}$ $BaCrO_4$[4]
$Y_xBa_{1-x}Fe_{2-x}Zn_xO_4$	$BaCO_3$ Fe_2O_3 Y_2O_3 ZnO	x = 0.1; 0.25; 0.5	1473	//	$BaFe_2O_4$ $BaFe_{12}O_{19}$ $Ba_2Fe_6O_{11}$ $ZnFe_2O_4$[5] $YFeO_3$[6]
$Ba_{1-x}K_xFe_{2-x}Si_xO_4$	$BaCO_3$ Fe_2O_3 K_2CO_3 SiO_2	x = 0.1	1573	//	$BaFe_2O_4$ Undetected impurities
$BaFe_{2-2x}Co_xSi_xO_4$	$BaCO_3$ Fe_2O_3 SiO_2 CoO	x = 0.1; 0.2	1573	//	$BaFe_2O_4$ Undetected impurities
$BaFe_{2-2x}Co_xMn_xO_4$	$BaCO_3$ Fe_2O_3 CoO + MnO_2	x = 0.025; 0.05	1473	//	$BaFe_2O_4$ $BaCo_{0.5}Mn_{0.5}O_{2.87}$[7]

Among these compositions, $BaFe_{2-x}Mn_xO_4$ shows that a certain degree of solubility of manganese ions cannot be ruled out for x-values ranging from 0.05 to 0.5, since the cell volume, obtained from the refinements performed on the respective diffraction patterns (using the Rietveld method, R-values ~9-10%), decreases significantly by increasing manganese fraction in the starting mixture. However, it is not clear whether the substitution process affects the variation of the oxidation state of Mn(III) species. Furthermore, given the unavoidable presence of impurities ($Ba_2Fe_6O_{11}$ and a barium manganite with formula $BaMnO_{3-\delta}$), extracting unambiguous information from any bulk characterization is quite complex. The summary of lattice information obtained for this

solid solution is reported in Figure 1 and Table II.

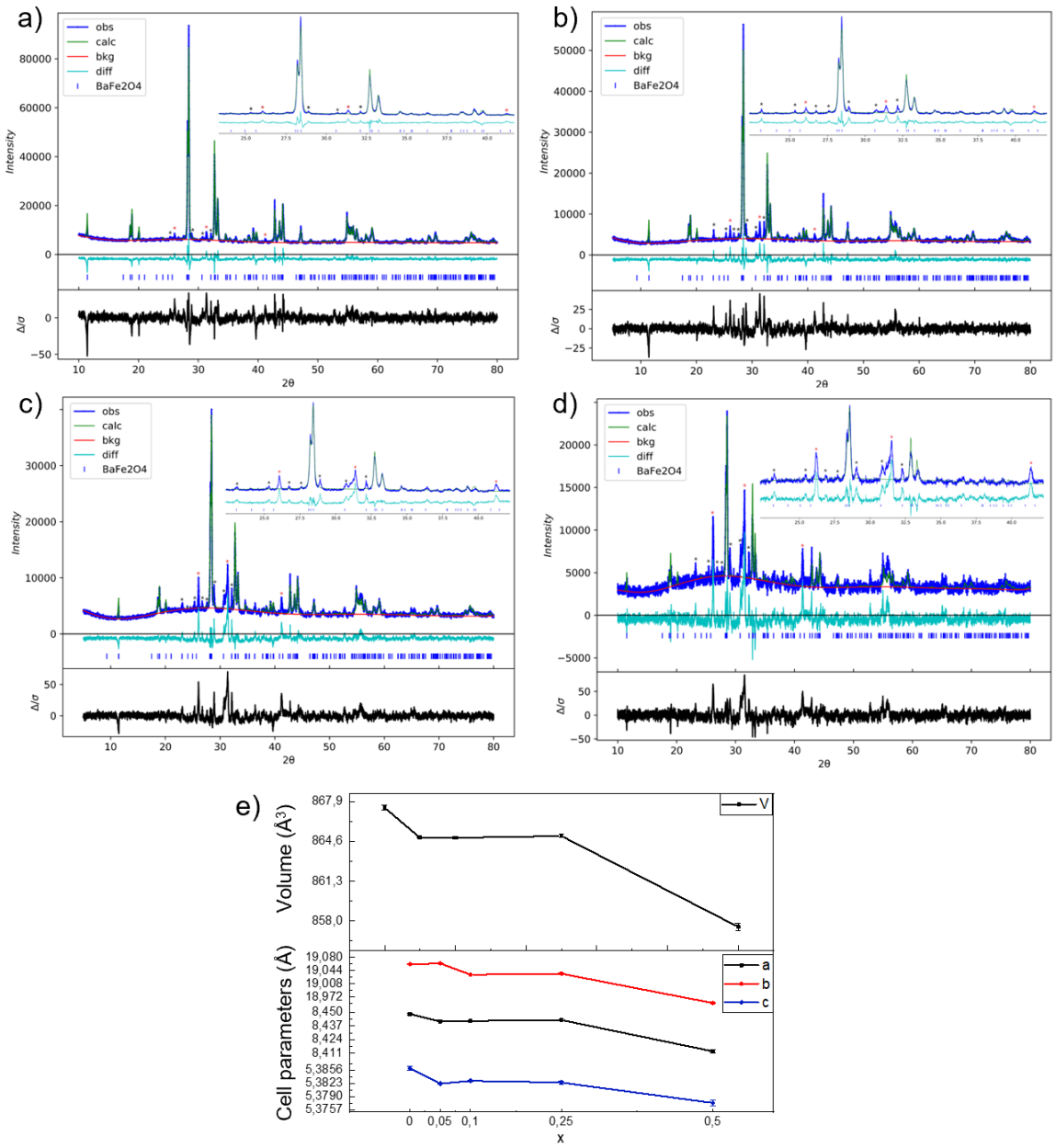

*Figure 1 – a), b), c), d) Rietveld refinements of PXRD patterns for x = 0.05/0.1/0.25/0.5 composition, respectively. Observed (+, blue), calculated (line, green) and difference (line, light blue) patterns are reported. Red line is the background, while the red and black * indicate $Ba_2Fe_6O_{11}$ and $BaMnO_{3-\delta}$ impurities. e) Variation of lattice parameters at increasing x-values.*

Table II – Refined lattice parameters of $BaFe_{2-x}Mn_xO_4$ compounds and phase percentage compositions of the obtained solid mixtures

x	a (Å)	b (Å)	c (Å)	Volume (Å^3)	$BaFe_2O_4$	$BaMO_{3-\delta}$	$Ba_2Fe_6O_{11}$
0.05	8.4414(2)	19.0368(5)	5.3822(2)	864.91(5)	88.5 %	4.4 %	7.1 %
0.10	8.4418(3)	19.0332(8)	5.3829(2)	864.90(8)	70.2 %	7.0 %	22.8 %
0.25	8.4427(6)	19.0359(13)	5.3825(4)	865.05(14)	59.2 %	14.5 %	26.3 %
0.50	8.4128(12)	18.955(2)	5.3774(7)	857.5(3)	42.1 %	26.3 %	31.6 %

5.2.2 Iron-gallium stuffed-tridymite solid solutions

Interesting results were obtained using Ga^{3+} as the substituting cation. Such ion is known s to form a stuffed tridymite framework with barium as the stuffing cation, $BaGa_2O_4$ (BGO), whose structure is describable by the non-centrosymmetric point group *6* (as already shown in paragraph 2.2.2). Considering the possibility for both pure monoferrite and monogallate systems to host a ferroelectric ordering, it might be interesting an investigation of the magnetic properties arising from a solid solution of both B-site cations, in order to try to induce a weak ferromagnetic component in both structures. As a consequence, a series of partial substitutions with different *x* values has been performed, described by the following reaction:

$$2\ BaCO_3 + (2\text{-}x)\ Fe_2O_3 + x\ Ga_2O_3 \rightarrow 2\ BaFe_{2-x}Ga_xO_4 + 2\ CO_2$$

The effects on the resulting lattice parameters have been checked by using Rietveld refinement method to fit the collected PXRD patterns. The following table (Table III) summarizes all the tested compositions.

Table III – Summary of the attempted syntheses related to $BaFe_{2-x}Ga_xO_4$

Chemical Composition	Structure
$BaFe_{1.95}Ga_{0.05}O_4$	γ-$BaFe_2O_4$-like (*$Cmc2_1$*)
$BaFe_{1.75}Ga_{0.25}O_4$	γ-$BaFe_2O_4$-like (*$Cmc2_1$*)
$BaFe_{1.6}Ga_{0.4}O_4$	γ-$BaFe_2O_4$-like (*$Cmc2_1$*)
$BaFe_{1.5}Ga_{0.5}O_4$	γ-$BaFe_2O_4$-like (*$Cmc2_1$*)
$BaFe_1Ga_1O_4$	$BaGa_2O_4$-like (*$P6_3$*)
$BaFe_{0.5}Ga_{1.5}O_4$	$BaGa_2O_4$-like (*$P6_3$*)
$BaGa_2O_4$	$BaGa_2O_4$-like (*$P6_3$*)

I. 0 < x < 0.5 compositions

All the compositions are synthetized at 1573 K, and no melting was detected. No differences between the first and second treatments ace have been detected, apart from the x = 0.4 and 0.5 compositions, exhibiting a by-product which disappears after the second furnace step.

In order to determine the lattice parameters of the obtained phases, Rietveld refinement was performed by using the structure of γ-$BaFe_2O_4$ as the crystallographic model. In this specific case, the results are obtained without refining the atomic positions and their displacement parameters, as being unavoidably affected by the crystal cell content, i.e. by the variable amount of gallium cations; since these are atoms with similar atomic numbers, it is reasonable to assume that the error in the refinement of intensities is limited. Nonetheless, the refinements give acceptable R (~7-8%) (Figure 2, Table IV). The relative variation of cell parameters compared to the starting BaFeO powder is shown in Figure 3a, in which the shortening of b and c lattice constants at increasing Ga^{3+} concentration is evident, as expected by adding cations with a slightly smaller ionic radius ($r_{Fe(III)} \approx 0.49$ Å versus $r_{Ga(III)} \approx 0.47$ Å in tetrahedral coordination). A divergent trend is observed for the *a* lattice parameter, whose value seems to be enhanced by the increasing presence of gallium cations. As a result, the total volume cell tends to settle around a value of roughly 864 $Å^3$ at the highest gallium contents (Figure 3b). It is hard to come up with an univocal explanation of this result by means of these preliminary analysis; considering the chemical differences between the two ions in terms of electron configuration, this increase might be due to a possible asymmetric deformation of the GaO_4 tetrahedra, resulting in a slight tilting affecting the cell parameter. Further characterizations are needed to confirm or revise this interpretation. Anyway, all these results suggest that gallium has been effectively integrated into the BaFeO structure.

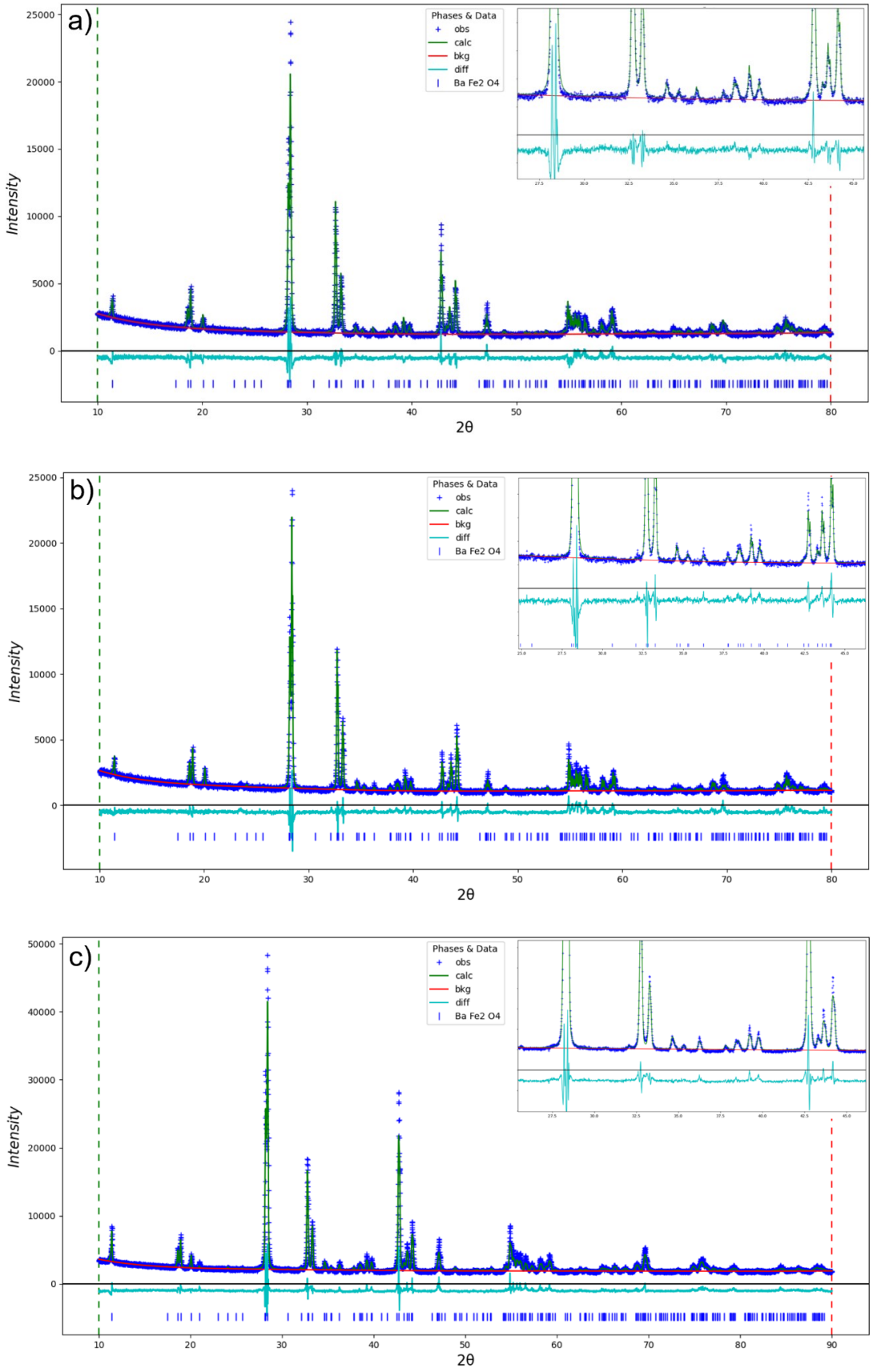
a)
b)
c)
Phases & Data
obs
calc
bkg
diff
Ba Fe2 O4
Intensity
2θ

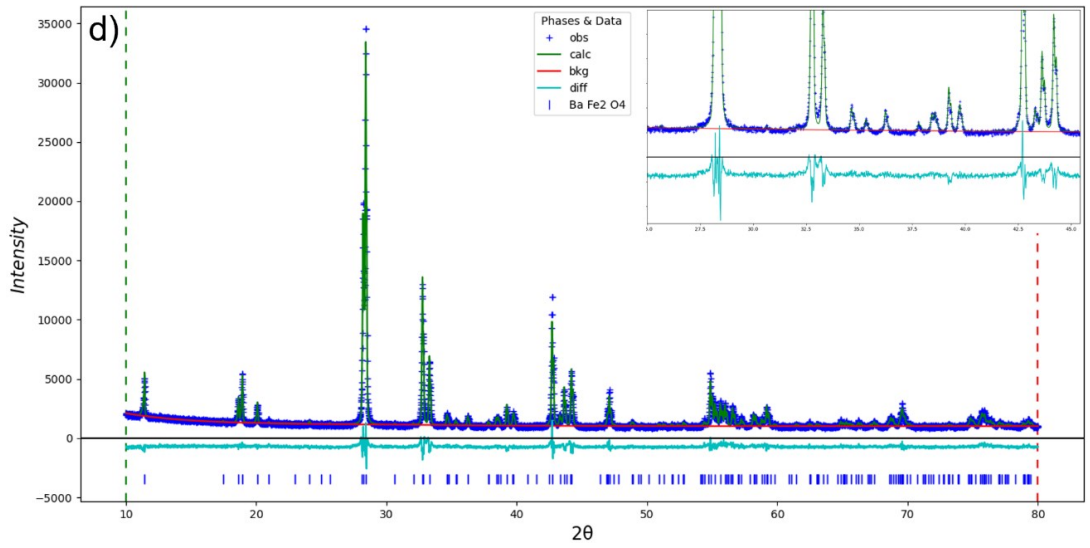

Figure 2 – Refined PXRD patterns obtained from 0.05 (a), 0.25 (b), 0.4 (c) and 0.5 (d) x-values. Observed (+, blue), calculated (line, green) and difference (line, light blue) patterns are reported. Red line is the background.

Table IV – Refined lattice parameters of $BaFe_{2-x}Ga_xO_4$ compounds

$BaFe_{2-x}Ga_xO_4$	**a (Å)**	**b (Å)**	**c (Å)**	**Volume (Å^3)**
x = 0.05	8.4435(2)	19.0375(5)	5.3835(2)	865.36(5)
x = 0.25	8.4465(2)	19.0250(3)	5.37730(9)	864.10(2)
x = 0.4	8.45504(9)	19.0145(4)	5.37572(12)	864.25(2)
x = 0.5	8.45759(8)	19.0116(3)	5.37487(7)	864.24(12)

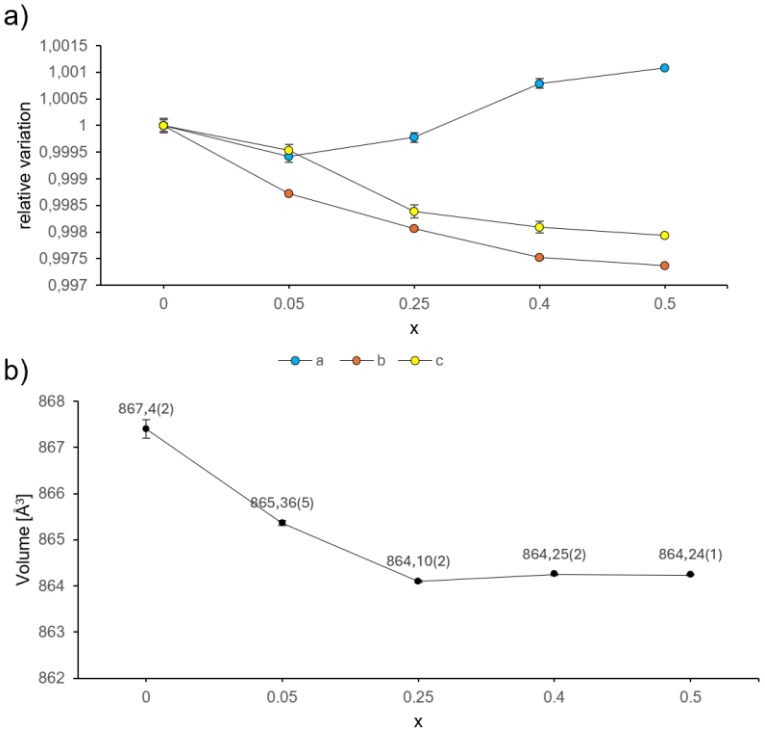

Figure 3 – a) Relative variation of lattice paramters with respect to the starting BaFeO composition (see chapter 3).

Blue, orange and yellow points represent the trend of a-, b- and c-parameters, respectively. b) The resulting cell volume variation for each composition.

II. 1 < x < 2 compositions

The syntheses performed with Ga^{3+} amounts exceeding x=1 do not show any reflections belonging to *γ*-BaFeO phase. Since small crystals (~100 μm) were detected within the polycrystalline matrix obtained from the solid-state synthesis, single-crystal diffraction data were collected to solve its room temperature structure. The obtained reciprocal lattice was indexed on the basis of a hexagonal cell with a' ≈ 2a, where a is the in-plane parameter of the original tridymite lattice. The refinement, carried out on 2536 independent reflections with 88 parameters and 1 restraint, has yielded an R_1 value of 5.74% by using the $P6_3$ space group. The final lattice parameters are a = 10.8235(3) and c = 8.6622(2) and all the refinement results are listed in Table V. Noteworthy, the non-centrosymmetric nature of the observed space group allows to host a net polarization oriented along the hexagonal c-axis.

Table V – Summary of $BaFeGaO_4$ crystal data and its refinement parameters. Atomic parameters were anisotropically refined.

$BaFe_{1.3}Ga_{0.7}O_4$, 293K s.g. $P6_3$ (173) a = b = 10.8235(3), c = 8.6622(2) Å V = 878.81(5) Å^3 ρ= 4.942 g/cm^3 Z=8							
Formula weight, 322.73 g/mol							
Wavelength		MoK$_\alpha$ (0.71073 Å)		Reflections		2536	
μ		15.537		Reflections (I > 4σ(I))		2117	
F(000)		1120.0		Parameters/restraints		88/1	
h		17		R1		0.0574	
k		17		R (I > 4σ(I))		0.0339	
l		14		wR2		0.0729	
θmin- θmax		2.173- 35.198		wR (I > 4σ(I))		0.0704	
Tmin-Tmax		0.339-0.7462		GooF (S)		1.027	
		x	y	z	s.o.f.	U$_{eq}$	Site
Ba	Ba1	0.00000	0.00000	0.25081	1.000	0.0121(2)	2a
Ba	Ba2	0.50918	0.02962	0.72762	1.000	0.01403(13)	6c
Fe	Fe1	0.32808	0.16790	0.42953	1.000	0.0052(3)	6c
Ga	Ga2	0.66667	0.33333	0.47170	0.660	0.0146(6)	2b
Fe	Fe2	0.66667	0.33333	0.47170	0.340	0.0146(6)	2b
Ga	Ga3	0.17110	-0.15860	0.53282	0.710	0.0093(4)	6c
Fe	Fe3	0.17110	-0.15860	0.53282	0.290	0.0093(4)	6c
Fe	Fe4	0.33333	-0.33333	0.55010	1.000	0.0093(4)	2b
O	O1	0.66667	0.33333	0.26160	1.000	0.058(4)	2b
O	O2	0.32210	0.22790	0.23560	1.000	0.0211(2)	6c
O	O3	-0.00450	-0.17090	0.51940	1.000	0.0125(13)	6c
O	O4	0.31190	-0.01190	0.42140	1.000	0.022(2)	6c
O	O5	0.32940	-0.49950	0.48930	1.000	0.018(2)	6c
O	O6	0.49140	0.28840	0.54420	1.000	0.033(2)	6c

	U$_{11}$	U$_{22}$	U$_{33}$	U$_{23}$	U$_{13}$	U$_{12}$
Ba1	0.0127(2)	0.0127(2)	0.0107(5)	0.000	0.000	0.00637(12)
Ba2	0.0113(3)	0.0195(2)	0.0099(2)	0.0002(3)	-0.0001(6)	0.0067(2)
Fe1	0.0064(6)	0.0056(12)	0.0031(5)	-0.0031(9)	-0.0011(3)	0.0027(11)
Ga2	0.0080(8)	0.0080(8)	0.0280(13)	0.000	0.000	0.0040(4)
Fe2	0.0080(8)	0.0080(8)	0.0280(13)	0.000	0.000	0.0040(4)
Ga3	0.0090(11)	0.0066(9)	0.0134(6)	-0.0008(8)	-0.0014(8)	0.0047(5)
Fe3	0.0090(11)	0.0066(9)	0.0134(6)	-0.0008(8)	-0.0014(8)	0.0047(5)
Fe4	0.0062(7)	0.0062(7)	0.0155(9)	0.000	0.000	0.0031(3)
O1	0.072(7)	0.072(7)	0.031(9)	0.000	0.000	0.036(3)
O2	0.045(4)	0.021(3)	0.007(3)	0.002(3)	0.001(4)	0.023(4)
O3	0.012(3)	0.010(3)	0.015(3)	-0.006(3)	-0.004(3)	0.005(3)
O4	0.026(5)	0.019(4)	0.030(4)	0.017(4)	0.021(4)	0.017(4)
O5	0.011(3)	0.009(4)	0.034(5)	-0.007(3)	0.000(4)	0.006(3)
O6	0.011(4)	0.050(6)	0.031(5)	-0.027(4)	-0.001(3)	0.010(4)

In addition, the crystal has turned out to be affected by merohedric twinning, which was considered throughout the refinement, with the twin law [(0 -1 0), (-1 0 0), (0 0 1)], corresponding to an apparent mirror perpendicular to the *ab* plane and giving birth to two

twin variants. For what concerns the lattice framework, the MO_4 (M = Fe/Ga) tetrahedra are oriented in two different ways, as each unit belongs to two ditrigonal-shaped rings with UUUDDD pattern and one with UDUDUD pattern, and are arranged in stacked layers rotated by 60°. Thus, the layers form the typical tridymite-like [001]-oriented cavities, filled by the barium stuffing cations, which result to be slightly shifted in [001] projection. Interestingly, iron and gallium ions are characterized by a precise distribution within the independent B-sites: two are totally occupied by Fe^{3+} ions, while other two are gallium-enriched, so that the tetrahedra are alternately occupied by the two chemical species. Conversely, the refinement of barium ions converges to full occupancy, without revealing any vacancies at the A-site. This arrangement also affects the variability of the bond lengths, whose values are summarized in Table VI, showing that gallium-oxygen bonds are shorter.

Table VI – Summary of Fe-O and Ga-O bonds

Fe - O bonds	**length (Å)**	**Ga - O bond**	**length (Å)**
Fe1-O2	1.814(9)	Ga2 O6	1.819(7)
Fe1-O3	1.863(8)	Ga2 O1	1.819(17)
Fe1-O4	1.866(9)	Ga3 O4	1.831(8)
Fe1-O6	1.872(8)	Ga3 O3	1.841(8)
Fe3-O2	1.876(9)	Ga3 O2	1.876(9)
Fe3-O5	1.887(9)	Ga3 O5	1.887(9)
Fe4-O1	1.832(17)		
Fe4-O5	1.854(7)		
Mean	**1.858(4)**	**Mean**	**1.846(4)**

Overall, the composition resulting from the refinement of the atom sites occupancies is $BaFe_{1.3}Ga_{0.7}O_4$, meaning that a certain amount of Ga^{3+} has not been integrated into the solid solution. The chemical composition of the same crystal sample has been assessed by an EDS analysis, whose results, shown in Figure 4c, confirm the iron-rich formula obtained from the crystallographic data ($Fe^{3+} \approx 61\%$ and $Ga^{3+} \approx 39\%$), corresponding to the $BaFe_{1.22}Ga_{0.78}O_4$ stoichiometry. Actually, the $BaFeGaO_4$ structure was already known to belong to the hexagonal symmetry [8]. However, although this crystallographic model is extremely similar to the one described above, it does not result completely reliable, as it presents a sort of atomic disorder, precisely on the O4-oxygen position, which is not well described by its thermal parameters. Figure 4a, b points out this main differences.

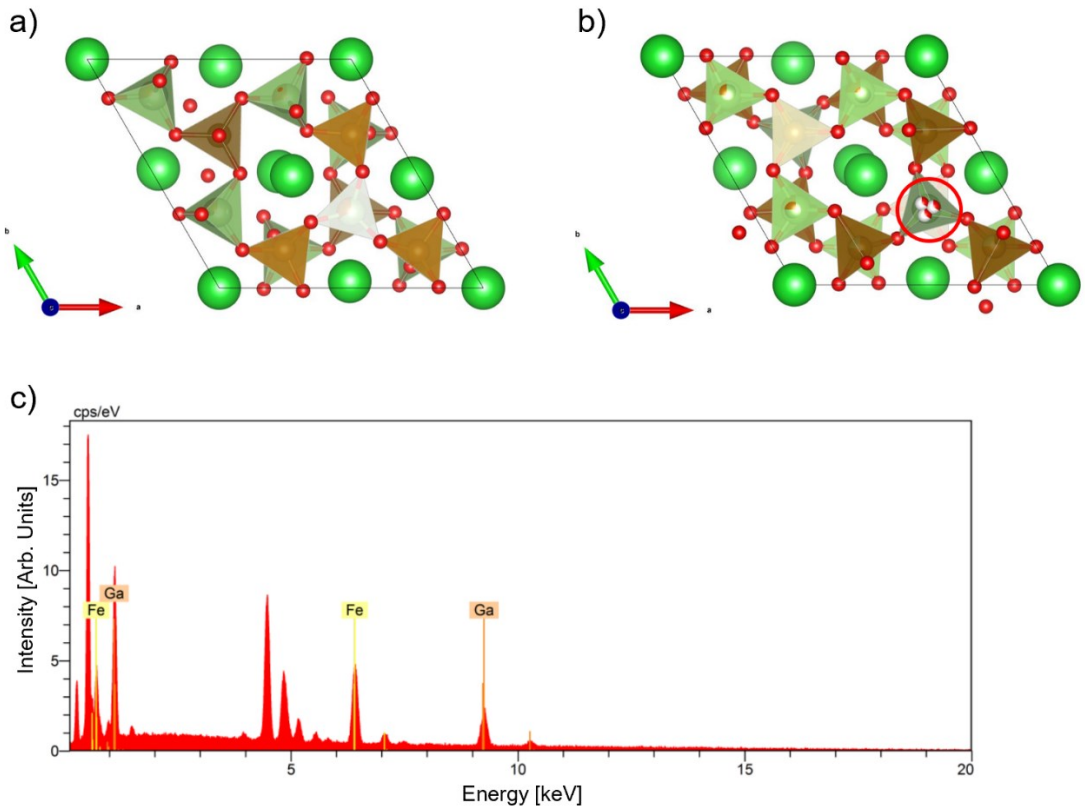

Figure 4 – Comparison between the here described $BaFeGaO_4$ crystallographic model (a) and the one found in literature (b). The red circle points out the uncertainty of the O4 oxygen position. c) EDX analysis on iron/gallium content in the nominal $BaFeGaO_4$ compound.

The above-described extrapolated structure has been used to perform Rietveld refinements on the nominal x =1 composition, highlighting the presence of one spurious peak at ~ 30° *2θ*, hardly attributable to a specific by-product (Figure 5a). Likely, this impurity comes out from that gallium excess amount which has not entered the stuffed tridymite framework. The structural model proves to be suitable also for other gallium-rich compositions, as in the case of x = 1.5, whose pattern does not exhibit any peak ascribable to impurities (Figure 5b). Even in this case, the lattice parameters are determined by performing Rietveld refinements (R_B ~ 7%), whose results show a net decrease of all lattice parameters for x = 1.5, as a result of the smaller size of Ga^{3+} ions (Table VII).

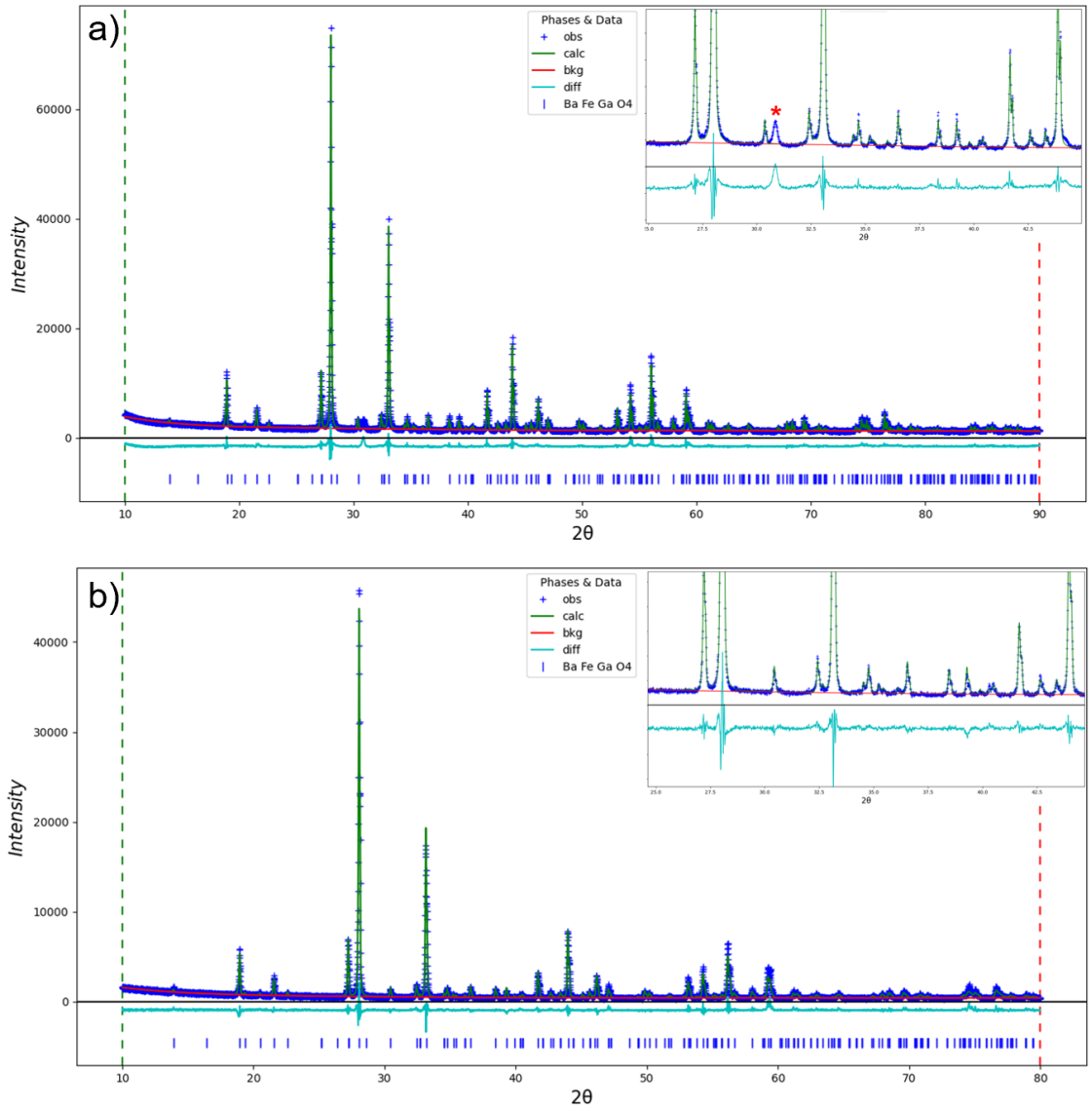

Figure 5 – Refined PXRD patterns obtained from 1 (a) and 1.5 (b) nominal x-values. Observed (+, blue), calculated (line, green) and difference (line, light blue) patterns are reported. Red line is the background. The previously obtained $BaFeGaO_4$ model was used as calculated pattern.

Table VII – Refined lattice parameters of $BaFe_{2-x}Ga_xO_4$ compounds with x = 1 and x =1.5

$BaFe_{2-x}Ga_xO_4$	**a (Å)**	**c (Å)**	**Volume (Å^3)**
x = 1	10.8246(2)	8.65868(6)	878.63(2)
x = 1.5	10.7961(5)	8.6546(12)	864.10(2)

5.2.3 Iron-aluminum stuffed-tridymite solid solutions

The chemical substitution of iron (III) with aluminum (III) was attempted following the

chemical reaction:

$$2\ BaCO_3 + (2\text{-}x)\ Fe_2O_3 + x\ Al_2O_3 \rightarrow 2\ BaFe_{2-x}Al_xO_4 + 2\ CO_2$$

The tridymite-type crystalline framework of $BaAl_2O_4$, already studied in the literature (see paragraph 2.2.2), is isostructural to $BaGa_2O_4$; consequently, it is expected that the behavior of Al^{3+} ions in the BaFeO lattice to be similar to that described for gallium in the previous paragraph. The compositions analyzed here are two: x = 0.1, 0.25. For the compound $BaFe_{1.9}Al_{0.1}O_4$, it was possible to obtain the pure phase attributable to γ-BaFeO after the first treatment; on the contrary, in the case of x = 0.25, three thermal treatments were necessary to eliminate all the detectable byproducts. The comparison between the PXRD patterns collected after each step (Figure 6) shows, in fact, the progressive reduction of the intensities of the peaks related to the impurity, which was identified as belonging to the composition $BaAl_2O_4$, and the consequent shift of the BaFeO peaks to the right, as a result of the integration of smaller ions than Fe(III) ones (0.39 Å for Al^{3+} versus 0.49 Å for Fe^{3+}).

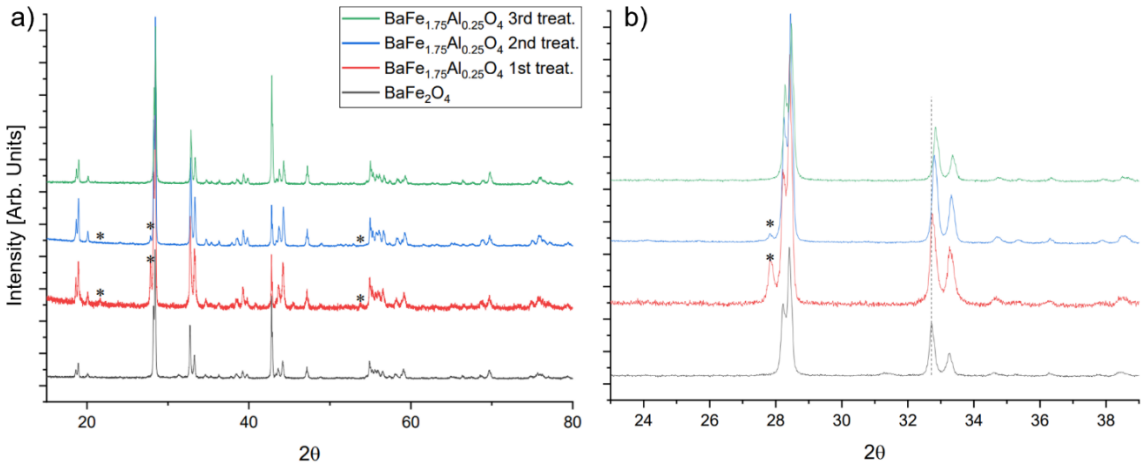

*Figure 6 – a) PXRD patterns related to $BaFe_{1.75}Al_{0.25}O_4$ collected after first (red), second (blue) and third (green) heating treatment. b) A magnified image of the patterns pointing out the progressive elimination of impurities (black *).*

The lattice parameters obtained from Rietveld refinements (R_B ~8%, Figure 7) reveal a trend similar to that observed for Fe-Ga series, in which the *b* and *c*- lattice parameters progressively decrease, while a slight increase of a is observed (Table VIII). A deeper characterization on the potential tilting of MO_4 tetrahedral units is needed to understand

this phenomenon; within this framework, the precise determination of oxygen positioning at different aluminum cations amounts by combining X-ray diffraction analysis with the neutron diffraction techniques, which are highly sensible to lighter atoms, might be a proper solution to further study these structures.

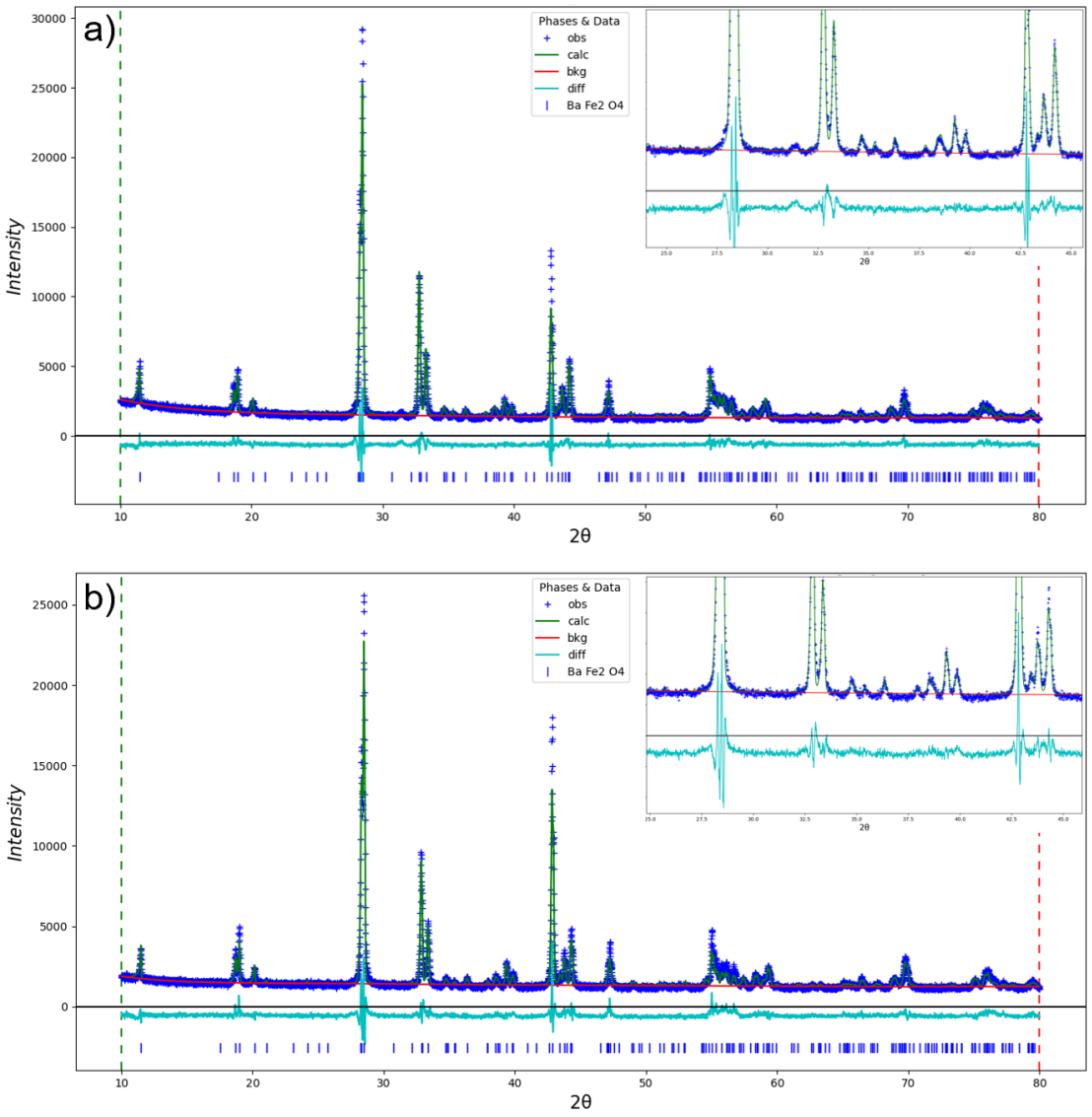

Figure 7 – Refined PXRD patterns obtained from 0.1 (a) and 0.25 (b) x-values for $BaFe_{2-x}Al_xO_4$. Observed (+, blue), calculated (line, green) and difference (line, light blue) patterns are reported. Red line is the background.

Table VIII – Refined lattice parameters of $BaFe_{2-x}Al_xO_4$ compounds with x = 0.1 and x =0.25

$BaFe_{2-x}Al_xO_4$	**a (Å)**	**b (Å)**	**c (Å)**	**Volume (Å^3)**
x = 0.1	8.4390(12)	19.0122(4)	5.3775(12)	862.79(2)
x = 0.25	8.4416(11)	18.9774(5)	5.3698(2)	860.24(3)

A first electric characterization was carried out on a disc-shaped ceramic pellet made of $BaFe_{1.75}Al_{025}O_4$ compound (thickness ~ 150 μm). The AC resistivity trend was assessed at a temperature ranging from 200 to 350 K (at the same frequency of 1 kHz, Figure 8). Room temperature values are comparable with those found for BaFeO composition (~ $3x10^8$ Ω m); moreover, a similar drop is observed over ~ 300 K, once again describable by Arrhenius fit. The activation energy is slightly higher (0.36 eV) than previous one determined for BaFeO compound; this result might be consistent with the plausible increment of the band-gap value due to the presence of electrons poor Al^{3+} ions.

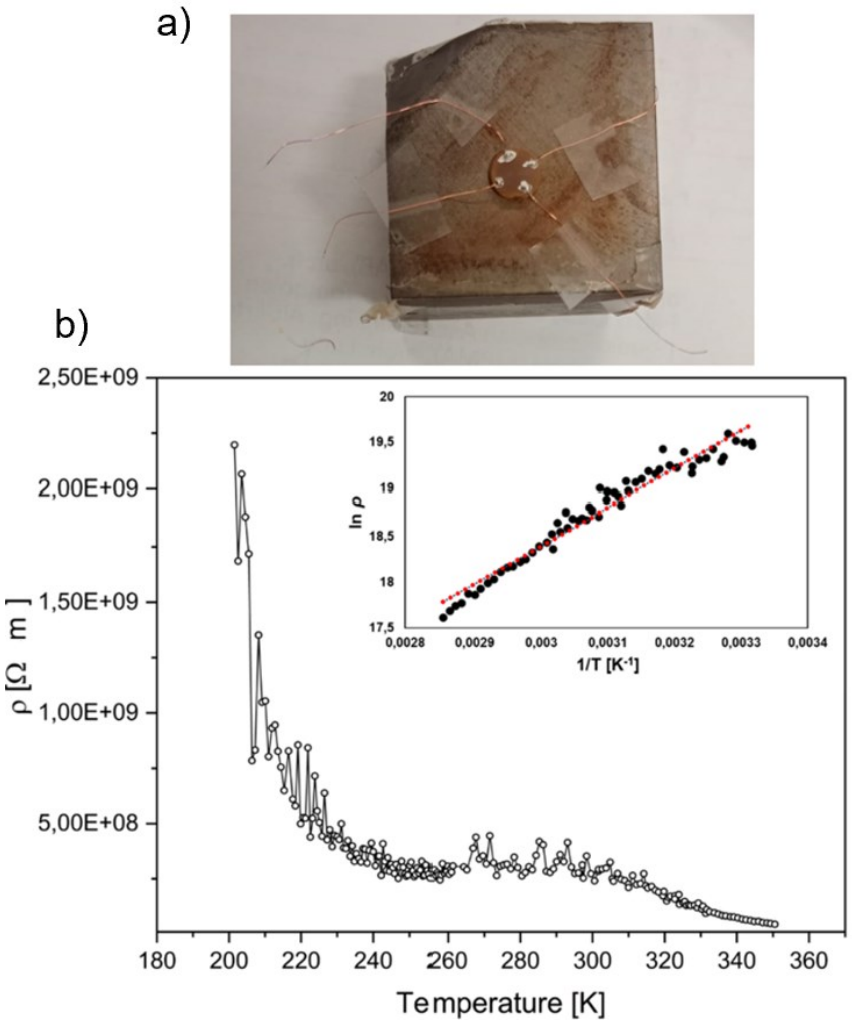

Figure 8 – a) Ceramic pellet made of $BaFe_{1.75}Al_{0.25}O_4$ with contacts for the electric characterization (copper wires were glued by using conductive silver paste); b) Electrical resistivity trend in the 200 – 350 K temperature range at kHz frequency. The inset shows the result from the Arrhenius fit performed on the 310 – 350 K temperature range.

For what concerns the ferroelectric analysis, a protocol based on dynamic hysteresis

measurement (DHM) was applied exploiting triangular voltage pulses of frequency 20 Hz with maximum voltage amplitude of 1300 V. The collection of such DHM response provides interesting information about the dielectric nature of the material which can be established by the linear trend of electrical polarization vs. V (Figure 9a). Noteworthy, a current invariant dependence vs. time along a linear increase of the voltage amplitude indicates the pure capacitive nature of the material at RT (Figure 9b) and it is confirmed by the characteristic discontinuity to symmetrical negative values at the change of voltage bias derivative, in a similar way to what was observed in the case of BaFeO (see paragraph 3.2.2). In this initial state, the measured average dielectric constant (ε_r) was estimated to be about 10.7. Preliminary attempts to test the possible ferroelectric character have been carried out in the last weeks. Through a proper fatigue cycles of repeated high voltage bias switching, it was possible to gradually increase the remnant polarization of the compound, reaching a maximum residual polarization of (~ 0.015 μC/cm^2) "written" after 10^9 electric poling cycles (Figure 10b). This protocol leads the opening of a weak hysteretic minor loop over the applied electric field (Figure 10a), pointing out the ferroelectric nature of $BaFe_{1.75}Al_{0.25}O_4$, although the estimation of a coercive field is at this stage not possible, being the system still far from the saturation state of its dipole. Unluckily, it was not possible to get closer the saturation due to technical reasons i.e. we reached the maximum voltage allowed by our HV amplifier in the reported fatigue cycle. Better results could be obtained in the next future testing thinner samples.

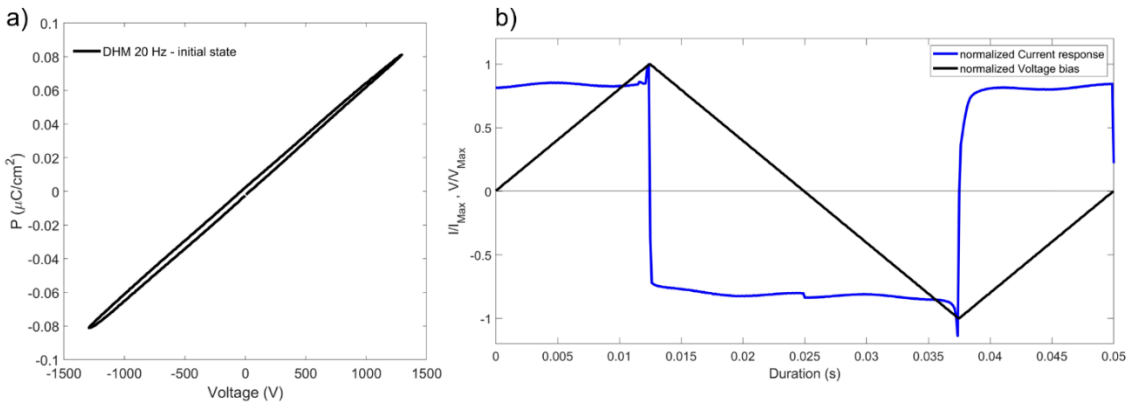

Figure 9 – a) DHM collected at the initial state, showing the typical curve generated by a dielectric material. b) Normalized voltage bias applied over time (black curve) and the resulting current response (blue curve), which follows the rapid charge/discharge path of a classic capacitor.

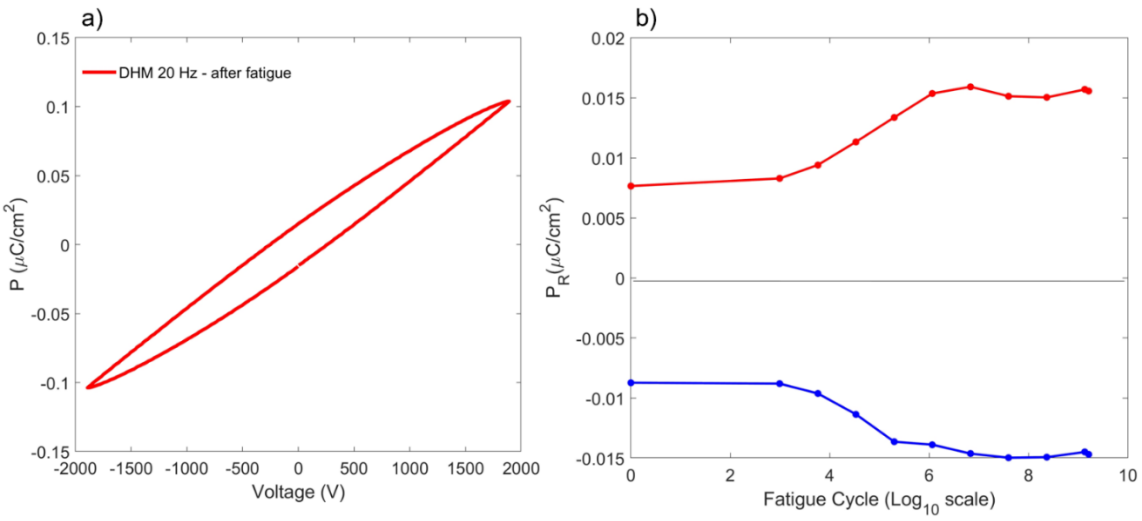

Figure 10 – Final polarization over applied electric field minor loop (a), collected after the full fatigue cycle carried out to induce a residual polarization (b).

5.3 References

[1] A. Collomb, P. Wolfers, P and X. Obradors *"Neutron diffraction studies of some hexagonal ferrites: $BaFe_{12}O_{19}$, $BaMg_2$ W and $BaCo_2$ W"* J. of Magn. and Magn. Mat. (1986), 62, 57-67

[2] J. C. Boivin, D. Thomas, G. Pouillard and P. Perrot *"Determination de la structure cristalline du ferrite de baryium $Ba_2Fe_6O_{11}$" Journal of Solid State Chemistry* (**1979**), *29*, 101-108

[3] J. J. Adkin and M. A. Hayward *"Structure and magnetism of 4H-Ba Mn $O_{(3-x)}$ ($0<x<0.35$) and 4H-$Ba_{0.5}Sr_{0.5}MnO_{(3-x)}$ ($0< x< 0.21$)" Journal of Solid State Chemistry* (2006), *179*, 70-76

[4] R. W. G. Wyckoff R. W. G. *The Structure of Crystals* by Interscience Publishers (1951),
3, 46-47

[5] P. F. The, S. S. Pramana, K. Chunjoong, C. Chieh-Ming, C. Cheng-Hao, Y. Sharma, J. Cabana and S. Madhavi *"Electrochemical Reactivity with Lithium of Spinel-type $ZnFe_{2-y}Cr_yO_4$($0 \leq y \leq 2$)"* Journal of Physical Chemistry C (2013), 117, 24213

[6] D. Boulay, E. N. Maslen, V. A. Streltsov and N. Ishizawa *"A synchrotron X-ray study of the electron density in $YFeO_3$*" Acta Crystallographica Section B (1995), 51, 921-929

[7] L. Miranda, J. Ramirez-Castellanos, A. Varela, J Gonzalez-Calbet, M. Parras, M. Hernando, M. T. Fernandez-Diaz and M. G.Hernandez *"Structural chemistry and magnetic properties of the Ba $Mn_{0.4}Co_{0.6}O_{2.83}$ hexagonal perovskite"* Chemistry of Materials (2007), 19, 1503-1508

[8] V. Kahlenberg, J. B. Parise, Y., Lee and A. Tripathi *"Characterization of the stuffed framework structures BaAlGaO4 and BaFeGaO4"* Zeitschrift für Kristallographie - Crystalline Materials (2002), 217, 6, 249-255

6 Conclusions and perspectives

This PhD thesis has systematically investigated the structural, electrical, and magnetic properties of *γ*-BaFeO single crystals and polycrystalline powders. Single crystal X-ray diffraction (SCXRD) revealed that *γ*-BaFeO crystallizes in the orthorhombic non-centrosymmetric space group *Cmc2₁*, with an off-centering of the Fe^{3+} ions along the c-axis, leading to the formation of ferroelectric domains. Structural analysis by TEM confirmed the twinning detected in SCXRD data. The ferroelectric properties were characterized by frequency-dependent P(V) measurements using a positive-negative (PN) protocol and by piezo force microscopy (PFM). The PN measurements revealed a hard-like hysteresis loop with a coercive field of 12 kV/cm and a remnant polarization of 0.18 $\mu C/cm^2$. The PFM measurements showed a butterfly-shaped hysteresis loop, further confirming the ferroelectric nature of the material. Neutron powder diffraction (NPD) measurements revealed a G-type antiferromagnetic ordering with a propagation vector k = (1 0 0) and a magnetic moment of 3.740(4) μB/Fe at 300 K. The antiferromagnetic transition temperature was determined to be 890.5(3) K. Bulk magnetization measurements carried out by SQuID vibrating sample magnetometry (VSM) showed a paramagnetic transition at 890 K, in agreement with the NPD data. However, the VSM measurements also showed a residual magnetic moment at low temperature, which is likely due to the presence of undetected impurities. Although other crucial features must be deeply studied, such as the magnetoelectric behaviour, all the results confirm that *γ*-$BaFe_2O_4$ is a bismuth/lead-free room-temperature multiferroic material, characterized by a stable ferroelectricity and an antiferromagnetic ground state.

Given the above-mentioned results obtained on polycrystalline BaFeO samples, the second part of the work focused on the deposition of crystalline *γ*-$BaFe_2O_4$ thin films using the Pulsed Electron Deposition (PED) technique. This step is crucial to assess the versatility of the material: in fact, multiferroic thin films offer several advantages over their bulk counterparts, such as the more feasible integration with existing devices and, by strictly controlling the deposition process, the uniformity in term of microstructure and domains orientation. According to the recent literature, this is the first comprehensive investigation of the experimental conditions required for the growth of pure BaFeO thin

films. Analysis of the plasma plume revealed that the dynamics of BaFeO deposition is governed by two primary mechanisms: a congruent ablation process, occurring far from thermodynamic equilibrium, and an incongruent low-energy evaporation process. Both mechanisms can be accurately described by a bicosine function model. Interestingly, this distribution significantly impacts the phase purity of BaFeO, as confirmed by structural and compositional characterizations. In the central and thicker region of the substrate, where the evaporative-to-ablative ratio is minimized, the presence of a secondary $Ba_2Fe_2O_5$ phase is not detected. This suggests that the evaporative contribution is the primary factor responsible for the out-of-stoichiometry composition. The spurious phase arises from the incongruent condensation of the target surface, where a mixture of γ-$BaFe_2O_4$ and $Ba_2Fe_2O_5$ phases tends to form. The influence of the substrate type on the structural properties of BaFeO films was also evaluated. Generally, (h00)-oriented BaFeO tends to grow on amorphous and polycrystalline substrates at 1073 K. Instead, in the case of SiO_2/Si substrates, that growth temperature promotes preferential growth of (0k0) and (0kl) lattice planes. Conversely, a heteroepitaxial (h00) film was obtained by depositing on a single-crystal MgO-(111) substrate. These latter results suggest that PED is not only suitable for producing high-quality γ-$BaFe_2O_4$ polycrystalline films but also opens up the possibility of achieving epitaxial growth of single-crystal layers. This unprecedented result paves the way for the utilization of such thin films for multiferroic application, where phase purity, structural orientation, and defect-free structures profoundly enhance the magnetoelectric properties of the device. As the last part of this work, a preliminary investigation on partially substituted barium ferrites has been carried out. Overall, mixed stuffed-tridymite systems have been obtained by replacing Fe^{3+} with Ga^{3+} and Al^{3+} on the B-sites of the BaFeO structure. In particular, it appears that a certain amount of both gallium and aluminum can be successfully incorporated into the orthorhombic phase, as confirmed by the decrease of its *b* and *c* lattice parameters; nonetheless, an unexpected increase of the *a* parameter is observed for both the solid solutions. Such results need a more in-depth study to precisely determine the position and deformation of the MO_4 tetrahedra. Within this framework, a combined analysis based on SCXRD and NPD technique could be an optimal choice. Moreover, regarding the iron-gallium series, it has been observed that, as the Ga/Fe ratio is above 0.33, corresponding to the x = 1.5 composition, the hexagonal symmetry, which is peculiar of pure $BaGa_2O_4$, prevails. This latter structure, having a non-centrosymmetric $P6_3$ space group, has been studied in detail

by a SCXRD-based analysis and might display a certain variation of the magnetic properties due to the presence of iron cations. Eventually, some electric measurements carried out on the $BaFe_{1.75}Al_{0.25}O_4$ composition suggest that even this mixed stuffed-tridymite maintains a ferroelectric behaviour, as a P(E) minor loop has been obtained. Although other attempts did not produce high-purity products, all these results represent a clear indication that BaFeO lattice is a versatile scaffold for synthesizing new stuffed-tridymites with the potential of a variety of properties.

Overall, the determination of an actual multiferroic state at room temperature, coupled with the demonstrated ability to effectively produce γ-$BaFe_2O_4$ in a variety of forms, from polycrystalline bulk to epitaxial film, outlines some interesting perspectives in a manner not dissimilar to what has happened in the case of more well-known materials, such as the aforementioned bismuth ferrite. The systematic definition of basic protocols for the characterization of the physical properties and synthesis of $BiFeO_3$ has motivated its experimental use in different and increasingly complex systems, starting from coupling tests with single layers of ferromagnetic materials (as described in Chapter 2) to its integration in the latest generation spintronic devices. This has made this ferrite one of the best-known multiferroic materials, even at the industrial level. In the current case, the discovery of BaFeO as a new multiferroic system with low leakage and stable ferroelectricity/antiferromagnetism, combined with the promotion of a further deposition technique able to effectively transfer its structural features on several substrates, aligns with some long-term goals of the scientific community, both in terms of achieving robust ferroic properties at room temperature and at any dimensional scale (from micro to nano), and in terms of the integration and scale-up of alternative synthetic approaches to enable manufacturing of multiferroic-based devices [1]. Surely, the next research target is certainly the in-depth characterization of any magnetoelectric coupling within the material; in this regard, the above-described optimization of the PED deposition protocol will turn out to be essential to precisely control the growth of crystal domains and, therefore, determine their magnetoelectric behavior. The range of possible interactions of barium ferrite with other typical materials of the electronics industry, such as soft ferromagnets and piezoelectric compounds, is also completely unexplored, and, so, it will represent the first step in the design of prototype devices. Moreover, it is worth noting that an architecture based on this compound might be ideal for the designing of next

generation logic devices, such as magnetoelectric random access memories, in which the presence of antiferromagnets has already demonstrated many advantages over traditional ferromagnetic MRAMs, in terms of resistance to magnetic interferences, ferromagnetic hysteresis losses and, mainly, switching energy [2]. Additionally, it would be appropriate to reconsider the well-known properties: for example, as already specified in Chapter 2, the photoabsorbent nature of BaFeO could be combined with its stable ferroelectricity even at high temperatures to produce photovoltaic cells; in this case, the PED technique has already largely shown its compatibility both with other well-known materials in the photovoltaic sector and other deposition techniques, such magnetron sputtering and the chemical bath deposition, which are crucial to design the modern thin film solar cells [3,4]. Then, it will be necessary to test the partial chemical substitution under different experimental conditions: at present, this material has demonstrated good compatibility with atoms that are also capable of generating stuffed tridymite structures, while, on the contrary, attempts made with ions characterized by various oxidation states have always produced impurities. Conducting the reaction in an inert atmosphere or transferring the reagents to other systems, such as sol-gel matrices, could prove to be solutions worthy of further investigation. It is therefore clear that this study lays the foundations for re-evaluating and expanding the technological potential of a material, albeit already known in the past, but so far exploited for limited experiment in confined fields of academic research.

6.1 References

[1] N.A. Spaldin and R. Ramesh *"Advances in magnetoelectric multiferroics"* Nat. Mat. (2019), 18, 203-212

[2] T. Kosub, M. Kopte, R. Hühne, P. Appel, B. Shields, P. Maletinsky, R. Hübner, M. O. Liedke, J. Fassbender, O. G. Schmidt and D. Makarov *"Purely antiferromagnetic magnetoelectric random access memory"* Nat. Commun. (2017), 8, 13985

[3] S. Rampino, N. Armani, F. Bissoli, M. Bronzoni, D. Calestani, M. Calicchio, N. Delmonte, E. Gilioli, E. Gombia, R. Mosca, L. Nasi, F. Pattini, A. Zappettini and M. Mazzer *"15% efficient Cu(In,Ga)Se_2 solar cells obtained by low-temperature pulsed electron deposition"* Appl. Phys. Lett. *(*2012), 101 (13), 132107

[4] G. Spaggiari, D. Bersani, D. Calestani, E. Gilioli, E. Gombia, F. Mezzadri, M. Casappa, F. Pattini, G. Trevisi and S. Rampino *"Exploring Cu-Doping for Performance Improvement in Sb_2Se_3 Photovoltaic Solar Cells"* Int J Mol Sci. (2022), 23(24),15529